2017

A Computational Study of Silver Doped CdSe Quantum Dots

Heather Gaebler
gaeb1500@mylaurier.ca

A Computational Study of
Silver Doped CdSe Quantum Dots

Heather M. Gaebler

THESIS

Presented to the Department of Chemistry and Biochemistry

in partial fulfillment of the thesis requirements

for the degree of Master of Science

Wilfrid Laurier University

Waterloo, Ontario, Canada

Abstract

Due to quantum dot's ability to emit photons when subjected to light of sufficient energy, they have become optimal candidates for biomedical research and for optoelectronic applications. Fascination towards quantum dots arises from the fact that their properties are easily fine-tuned through a variety of different techniques. Electronic doping is a popular technique used to control the properties of quantum dots through the addition of different elements.

Via density functional theory calculations, this work investigated how the structural energies and HOMO-LUMO gaps were altered by the addition of impurity atoms. First, interstitial and substitutional doping styles were investigated at 0 K for a CdSe quantum dot that contained a single Ag^+ impurity ion, and it was concluded that the interstitial doping style was more structurally favourable than substitutional doping. In addition, different dopant locations were analyzed and it was determined that interstitially doped structures with Ag^+ ions in surface site locations were approximately 1 eV more structurally favourable than structures with dopant ions placed midway in the structure and at the core.

To maintain charge neutrality after the addition of a Ag^+ ion, a Cl^- ion was added to the surface and it was determined that the closer the two atoms were on the surface the more structurally stable the quantum dot was at 0 K. Also, the HOMO-LUMO gaps for those structures were larger by approximately 0.5 eV compared to the structures where the two atoms were placed farthest apart on the surface.

At a finite temperature value of 333 K, there were no trends visible between the HOMO-LUMO gaps, structural energies, and the distance between the 2 atoms. It was however concluded that all doped structures were more energetically favourable than their undoped counterpart at both temperature values of 0 and 333 K.

Acknowledgements

I would like to thank my co-supervisors Dr. Ian P. Hamilton and Dr. Marek S. Wartak for providing me the opportunity to complete my Master of Science degree. I am forever grateful for the constant guidance, support, and encouragement they both have shown me over the past two years. I would also like to thank Dr. Vladimir Kitaev for being an outstanding committee member and Dr. Lillian DeBruin for her help in guiding me through this entire process.

I was inspired to achieve this level of education by the birth of my two God Daughters, Bianca and Elisabeth. In addition, I would also like to acknowledge my immediate and extended family for their constant love and support.

Finally, I would like to thank Wilfrid Laurier University, Compute Canada, NSERC (Natural Sciences and Engineering Research Council), and ASPIRE (Applied Science in Photonics and Innovative Research in Engineering) for graciously funding the research I completed.

Contents

List of Figures

List of Schemes

List of Tables

List of Abbreviations

Å	– angstrom
AIMD	– ab initio molecular dynamics
BOMD	– Born-Oppenheimer molecular dynamics
DFT	– density functional theory
DZVP	– double-zeta valence polarized
eV	– electron volt
fs	– femtosecond
GPW	– Gaussian and plane waves
GTH	– Goedecker-Teter-Hutter
HOMO	– highest occupied molecular orbital
K	– Kelvin
KS	– Kohn-Sham
LSPR	– localized surface plasmon resonance
LUMO	– lowest unoccupied molecular orbital
MNPBEM	– metal nanoparticle boundary element method
nm	– nanometer
ns	– nanosecond
QD	– quantum dot
R^2	– coefficient of determination
TOP	– trioctylphosphine
TOPO	– trioctylphosphine oxide
TPP	– triphenylphospine

Chapter 1: Introduction

1.1 Semiconductors

Bulk semiconductors are universally defined as an intermediate conductivity material between metals and insulators[1], and are credited as being one of the most resourceful classes of materials known to the scientific community.[2] Aside from a few exceptions, semimetals and metals are zero energy gap materials while insulators contain an energy gap greater than 3 eV.[2] Figure 1.1 illustrates the absence of energy gaps in metals and the presence of energy gaps in semiconducting and insulating materials. The energy gap in a semiconductor can be described as the minimum amount of energy an electron requires in order to be promoted from its bound state in the valence band to a free state in the conduction band.[3,4]
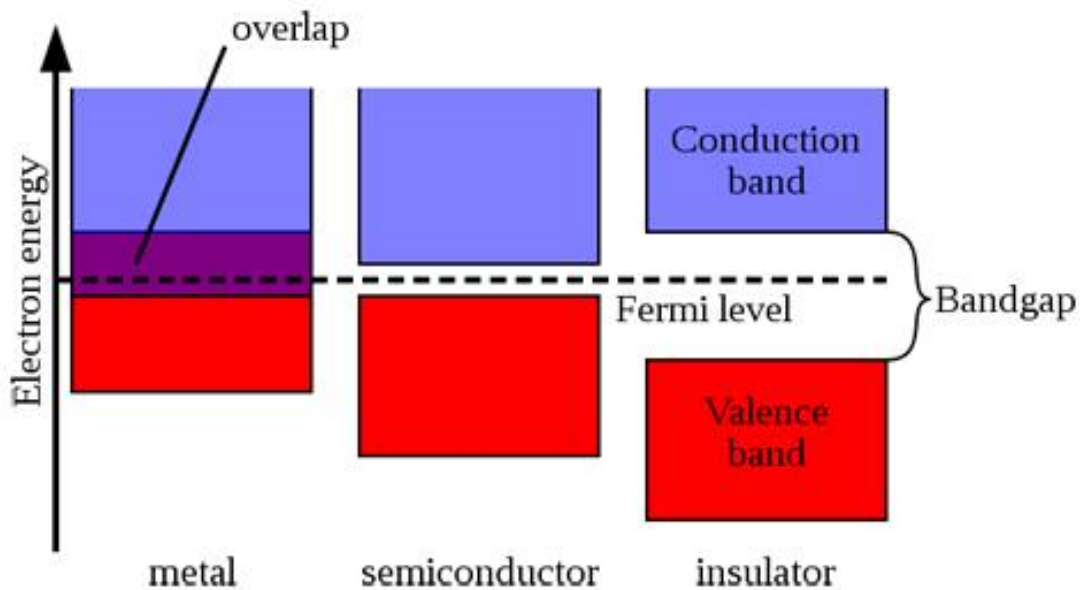
Figure 1.1: Electronic band structure diagrams of insulators, semiconductors, and metals. [5]

1.1.1 Nanoscale Semiconductors

Ever since technology was integrated into everyday life, the investigation of both semiconductors and structures that exist on the nanoscale have been at the forefront of materials research.[6-9] Nanostructures are structures that have at least one of their dimensions fall between the range of 1 and 100 nm,[10] and have gained widespread interest due to their novel characteristics and properties.[11] Based on morphology, nanostructures can be divided into 3 different classifications: 0-dimensional (if they resemble spheres), 1-dimensional (if they are elongated like a rod or wire), and 2-dimensional (if they are planar like a sheet of paper).[10] Leading with the catch-phrase "smaller means greater", nanoscale semiconducting materials have been integrated into many electronic devices ultimately producing a quicker device turn-on time, a lessened power consumption, a decrease in consumer cost, and of course as their name suggests, a decrease in device size.[10]

1.1.2 Quantum Dots

In the early 1980's, thorough experimentation lead to the remarkable discovery of semiconducting nanoscaled particles, coined as quantum dots (QD).[12] Still today, fascination arises from the QD's ability to emit photons of various wavelengths when subjected to light of sufficient energy, and that the colour of the light released under excitation is a direct consequence of the confinement of the QD's electrons.[13-18] When a photon of sufficient energy is absorbed by the QD, an electron is promoted to a higher energy level and an exciton is formed. An exciton is the bound state of the

electron and its hole which are attracted to each other by the electrostatic Coulomb force. The electron is negative and the hole is positive, but together they are electrically neutral. The excitons of a QD are confined in all three spatial dimensions; the wave functions of the electrons are restricted by the volume of the QD, and it is the recombination of the electron-hole pair that is responsible for the coloured emission.[19] After many detailed investigations it was concluded that the size of the energy gaps were inversely proportional to the size of the QD, meaning that larger QD's will emit lower energy light, and smaller QD's of the same material will emit higher energy light.[19] This phenomenon is known as the quantum confinement effect[20-22] and is outlined in Figure 1.2.
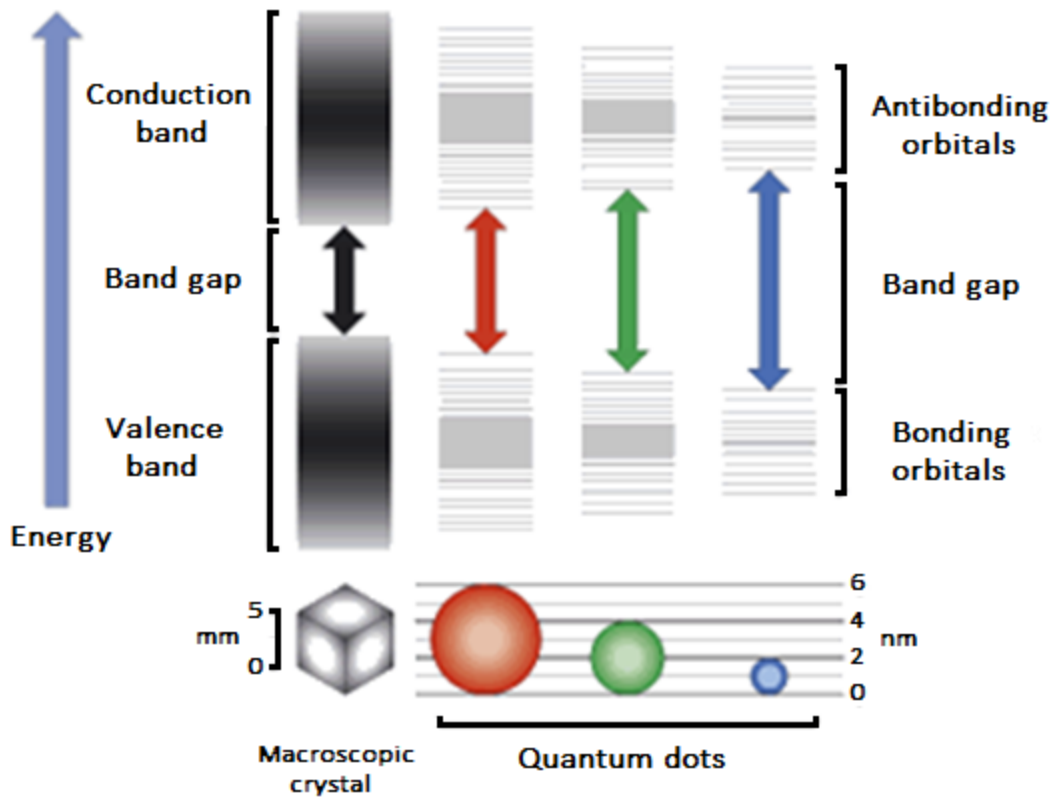
Figure 1.2: Schematic representation of the quantum confinement effect, outlining the controllable emission of light from various sized quantum dots.[20]

From an application point of view, QD's are extremely desirable since their energy gap can be fine-tuned by size alteration to achieve a selective absorption.[23] An easier method compared to composition variation, it involves monitoring the size of the nanocrystals during chemical processing[24] and can result in an energy gap that has been tailored several fold.[25] Some heavily studied inorganic QD's include ZnS, PbS, CdS, CdTe, and CdSe which are utilized in a wide range of applications from photovoltaics[14,15,26], biosensing and medicine[27], to light-emitting devices.[28,29]

In order to achieve a higher degree of stability, a technique called surface passivation is frequently employed by coating the core of the QD with larger energy gap inorganic semiconductors[30-33] and by adding a layer of stabilizing ligands to the surface.[34] Figure 1.3 demonstrates how the shell encompasses the entire core while the ligands bound to the shell protrude outwards. Without surface passivation, the QD's fluorescing abilities are known to quickly decay under powerful laser illumination[35,36] until reaching an everlasting dark state.[37]
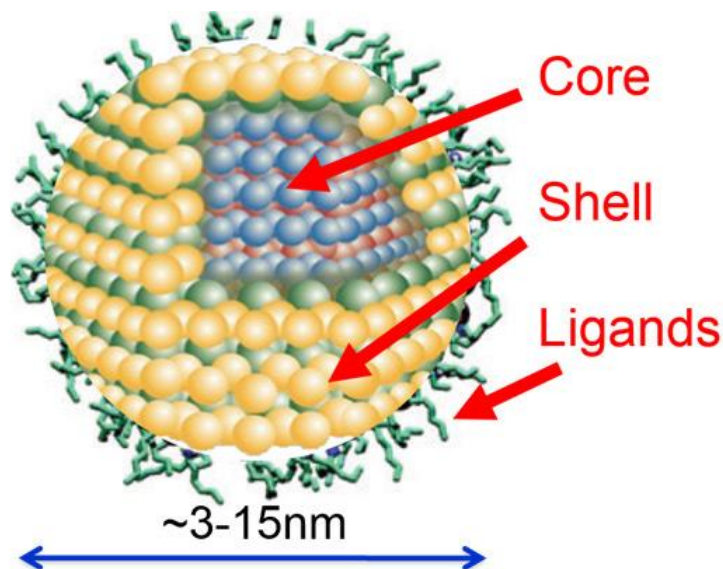
Figure 1.3: Diagram of the core/shell model with a cross-sectional view displaying each portion of the QD.[38]

1.1.3 Electronic Impurity Doping

Through the intentional addition of impurity atoms, tight control over magnetic, optical, and electronic properties of quantum dots can be achieved.[39,40] Compared to their undoped counterpart, doped QD's experience a decrease in self-quenching, reabsorption from the enlarged Stokes shift, and are much less sensitive to chemical, thermal, and photochemical disturbances.[41,42] Introduction of an impurity through a process known as electronic impurity doping will provide the QD with either extra holes or extra electrons.[43] Extra holes are created when the impurity atom contains less valence electrons than the atom it is replacing. Extra electrons are present when the impurity atom has more valence electrons, and therefore when ionized by thermal energy it will donate electrons to the QD.[44] These added holes or electrons become readily available as carriers of electrical current and therefore are beneficial for enhancing conduction.[43,44] To maintain charge neutrality after the addition of the positive holes or negative electrons, appropriately charged ligands can be added to the QD surface.

Despite the fact that the addition of carriers to QD's via methods (remote doping via binding ligands,[45-47] electrochemical doping,[46,47] and thermal treatments[48,49]) have been successful, studies involving electronic impurity doping are often restricted due to the synthetic challenge of integrating an impurity atom into a nanosized object.[44] Additional complications may arise after the introduction of only a few impurity atoms to a nanocrystal that may contain hundreds of atoms. As a result of the minute size of the nanocrystal, a process known as "self-

purification" may occur which is the expulsion of the impurity atoms to the surface which could compromise the entire structure of the nanocrystal.[51-54] In the past, the introduction of the impurity atoms at specific stages in the nanocrystal's growth has proven to be an effective approach in controlling where the impurity atoms reside within the structure.[55]

1.1.3.1 Silver Impurities

Silver (Ag) as an impurity atom in bulk II-VI semiconductors is known to participate in either p-type doping and adopt a substitutional site,[56-58] or n-type doping and inhabit an interstitial site within the semiconductor.[57,58] A II-VI semiconductor is a binary compound comprised of a metal from group 2 or 12 of the periodic table of elements and a non-metal from group 16 (previously known as group 6). Recent efforts by Banin *et al.* were successful in incorporating Ag impurities into InAs nanocrystals as shifts in the valence and conduction bands were detected via scanning tunnelling microscopy.[59] Their research primarily focused on the heavily doped limit as tens to hundreds of Ag^+ ions were incorporated into each of their InAs nanocrystals, and it was proposed that there was a direct substitution of In^{3+} with a Ag^+ ion. The decrease in valence electrons resulting from the replacement of In^{3+} with Ag^+ causes an electron deficiency in the bonding orbitals which is characteristic of p-type doping.[59] Another research project was conducted by Norris *et al.* on the effects of adding Ag^+ ions to a PbSe lattice.[60] It was initially hypothesized that since Ag^+ had only one valence electron it would act as an electron acceptor if substituted in for Pb^{2+}

in the lattice. With the substitution of Pb^{2+} for Ag^+, the deficiency of electrons would create a hole and ultimately lower the Fermi level of the system. The Fermi level can be thought of as a hypothetical energy level that is located at the midway point between the valence and conduction band in an undoped semiconductor. It is the highest point at which electron energy levels can exist at zero kelvin. If holes are added to a system the Fermi level will drop since the probability of finding a hole near the valence band is higher than the probability of finding an electron near the conduction band. The opposite trend is observed when electrons are added to the system and therefore by monitoring changes in the Fermi level with a voltmeter it can be deduced which type of doping style is occurring within the system. Unable at that time to create conditions that would allow for low doping levels, Norris *et al.* like Banin *et al.* observed the effects of adding tens of Ag^+ ions to the PbSe lattice. After careful examination of the mobility pre-exponential factor, the threshold voltage, and the activation energy for electron transport, it was successfully concluded that the Ag^+ ions were operating as electronically active impurities that were lowering the Fermi level, thus adopting the p-type doping style.[60] Norris *et al.* also conducted a similar study on CdSe QD's, however the basis of the experiment was to investigate the effects of lightly doping with Ag^+ ions.[43] It was concluded from their optical and electrical data that Ag^+ ions were in fact behaving as an electronically active impurity. However, it was surprising that the addition of just a few Ag^+ ions per nanocrystal caused the largest enhancement in fluorescence.
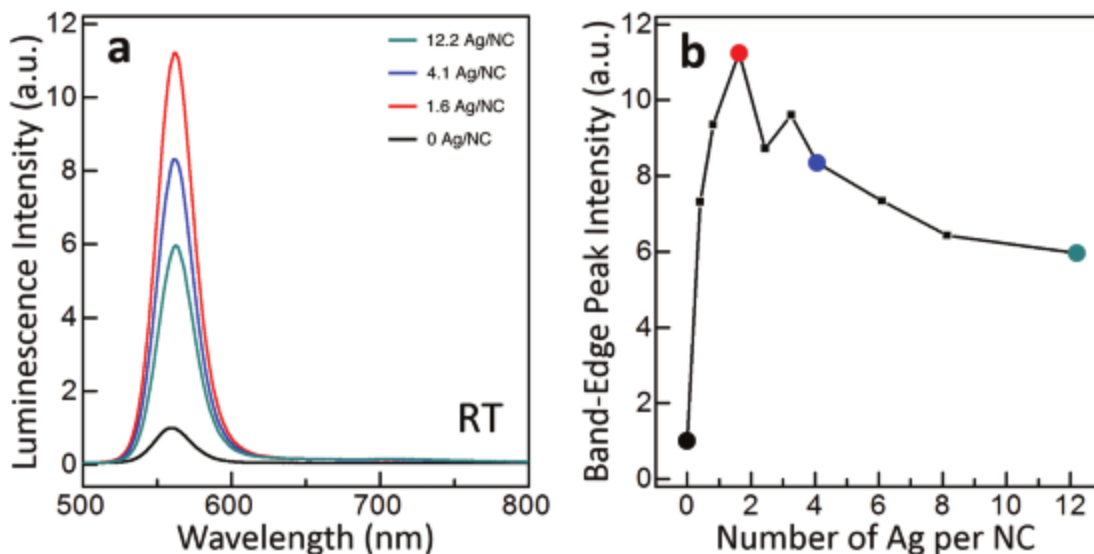
Figure 1.4: (a) Room temperature fluorescence spectra of a 3.1nm-diameter CdSe QD containing no Ag⁺ (black), 1.6 Ag⁺/QD (red), 4.1 Ag⁺/QD (blue), and 12.2 Ag⁺/QD (green). The band gap fluorescence peak intensity near 560 nm plotted as a function of the number of Ag⁺ ions per quantum dot. [43]

Figure 1.4(a) and (b) illustrates that the fluorescence intensity of a 3.1 nm-diameter CdSe QD increased upon the addition of Ag⁺ ions, with the maximum intensity occurring at approximately 2 Ag⁺/QD. As the concentration of Ag⁺ ions was increased, the fluorescence intensity decreased from this maximum. An additional 9 CdSe QD's with varying diameters were also doped and displayed the same trend of a decrease in intensity from the maximum upon increase in Ag⁺ concentration. It was also noted that there was a spike in the quantum yield from 14% to 27% after the addition of approximately 2 Ag⁺ ions; a dramatic increase that makes the doped CdSe QD's comparable to that of CdSe/ZnS core/shell nanocrystals.[61,62]

1.2 Computational Experimentation

Computational chemistry is a subdivision of chemistry that utilizes computers to determine atomic and molecular structures and properties. Computational chemists have the ability to solve many-body problems through the use of mathematical algorithms, statistics, and large databases of information and can ultimately bridge the gap between theory and experimental observations. The methods used to solve such problems can be employed for both static and dynamic situations. Popular methods used for electronic structure calculations are Density Functional Theory (DFT), and ab initio molecular dynamics (AIMD).

1.2.1 Density Functional Theory

Density functional theory is a computational quantum mechanical modelling method and is the backbone of electronic structure calculations.[63,64] Used primarily for the modelling and simulation of chemical many-body systems,[65] DFT solves the Schrödinger equation for an interacting system by mapping it exactly to a much simpler non-interacting system. The DFT foundation rests on two essential mathematical theorems formulated by Hohenberg and Kohn and a select set of equations designed by Kohn and Sham.

1.2.1.1 Hohenberg-Kohn Theorems

In 1964, Pierre C. Hohenberg and Walter Kohn introduced the two fundamental theorems widely known as the Hohenberg-Kohn theorems.[66,67] The first

theorem states that "the external potential, and hence the ground-state energy from Schrödinger's equation is a unique functional of the electron density".[68] Putting it simply, a functional is a function of another function and this theorem is stating that the ground-state wave function is mapped to the ground-state electron density in a 1:1 ratio. The second theorem provides insight on the functional itself and states that "the electron density that minimizes the energy of the overall functional is the true electron density corresponding to the full solution of the Schrödinger equation".[68]

1.2.1.2 Kohn-Sham Equations

As for the select set of equations, Walter Kohn and Lu Jeu Sham invented a set of non-interacting electrons which have the same density as those in the interacting problem. The Kohn-Sham (KS) equations are outlined below[68,69,70]:

$$\{-\frac{1}{2}\nabla^2 + v_{KS}(r)\}\ \psi_i(r) = \varepsilon_i\psi_i(r) \qquad \text{(Eqn. 1.1)}$$

In reference to the non-interacting Schrödinger equation (Eqn. 1.1), the KS potential (v_{KS}) on the left hand side of the equation can be broken down into 3 separate components: v_n, v_H, and v_{XC}. v_n defines the potential involved with the interaction between an electron and the collection of atomic nuclei. v_H is termed as the Hartree potential and can be mathematically expressed as[68,69,70]:

$$v_H(r) = \int\frac{n(r')}{|r-r'|}d^3r' \qquad \text{(Eqn. 1.2)}$$

The Hartree potential represents the Coulomb repulsion between the electron chosen in the KS equations and the total electron density from all the electrons within the

system. The final potential component is the functional derivative of the exchange-correlation energy[68,69,70]:

$$v_{XC}(r) = \int \frac{\delta Exc}{\delta n(r)} \qquad \text{(Eqn. 1.3)}$$

In summary, solving the KS equations can be thought of as a never ending cycle in the sense that in order to obtain your solution you need to define the Hartree potential, but to define the Hartree potential you need to know the electron density. To obtain the electron density you must know the single electron wave functions which must be solved using the KS equations. This cycle was broken through the creation of a set of rules for such "never-ending" calculations. Ideally created for a computer, the algorithm used to solve this cycle is known as the self-consistent field theory.

1.2.2 Ab Initio Molecular Dynamics Approach

An extension of DFT, ab initio molecular dynamics (AIMD) is a computational tool that provides insight on classical many-body problems.[71] This finite-temperature simulation method allows users to follow the trajectories of moving atoms[68] and accurately calculate equilibrium and non-equilibrium properties.[72] By applying an approximation formulated by Born and Oppenheimer, these types of calculations have been simplified which allows for completion in a timely manner.

1.2.2.1 Born-Oppenheimer Approximation

In 1927, Max Born and J. Robert Oppenheimer proposed the assumption that since the electrons of a molecule were moving so quickly compared to the nuclei that their motions could be separated and the nuclei viewed as clamped centers.[66,73] With the wavefunction separated into two components, the kinetic energy term associated with the nuclei can ultimately be neglected. Since the number of degrees of freedom of the system has now been reduced, the electronic wavefunctions and energies can be calculated. It is important to note that although the kinetic energy term associated with the nuclei has been disregarded based on them being labelled as stationary, the positions of the nuclei are an important factor in determining the electronic wavefunctions and energies.

1.2.2.2 Born-Oppenheimer Molecular Dynamics Method

Utilizing the approximation outlined above, Born-Oppenheimer molecular dynamics (BOMD) calculates the potential energy of the system "on the fly" if the potential energy of the atoms are known as a function of the atomic coordinates. This concept can be mathematically expressed by defining a quantity called the Lagrangian, L, in terms of the kinetic, K, and potential, U, energies:[68]

$$L = K - U = \frac{1}{2}\sum_{i+1}^{3N} m_i v_i^2 - U[\varphi(r_1,....,r_{3N})] \qquad \text{(Eqn. 4)}$$

where N is the number of atoms, m_i and v_i are the mass and velocity of the atom associated with the *ith* coordinate, r represents the configuration of the atoms at any moment in time, and $\varphi(r_1,....,r_{3N})$ is the full set of the Kohn-Sham one-electron wave

functions for the electronic ground state of the system. In brief, the ground state energy of the system is calculated first, followed by the slight movement of all nuclei, followed by the calculation of the new ground state energy, followed by the slight movement of all nuclei again, and so on. In BOMD, each movement of the nuclei is considered one time step, and the size of the step depends on the time it takes for the smallest vibration within the molecular system to occur. To monitor the trajectories of atoms accurately, numerous time steps must be taken to visualize a single vibration. In general, the nuclei are moved in steps that are roughly no bigger than 10 fs, meaning that in order to view a system for even a single nanosecond 100 000 steps will be required.

1.3 Limitations of DFT

DFT is often the method of choice for modelling reaction paths,[74] catalytic reaction mechanisms,[75] and properties of atoms, molecules, and solids.[76] Although a great choice for high electron count systems due to its low computational cost, DFT is still prone to extensive failures that ultimately produce qualitative errors in the predicted properties. After careful examination, several failures have been exposed as violations of conditions of the functional used within the method.[77]

Since semiconductors are a leading material in the field of nanotechnology, accurate predictions of their energy gaps are imperative. While it has been possible for DFT to provide information on energy gaps as far back at the 1980's,[78-80] the issue of underestimating the value of the energy gap still remains problematic.[81] Other

parameters that are underestimated are the barriers of chemical reactions, charge transfer excitation energies, and the energies of dissociating molecular ions.[81]

Another downfall of DFT is the description of van der Waals interactions.[82,83] A fundamental force for many molecular processes, London dispersion forces are the attractive interaction between self-induced instantaneous dipole moments of ground state electron distributions.[84,85] There are density functionals that exist which fail to accurately describe leading dispersion interactions[84] which are an important component in the qualitative and quantitative behaviours of a system.[86]

Although there are well-known issues within the DFT method, it is still an extremely desirable computational quantum mechanical modelling method for electronic structure calculations. Even though DFT underestimates important values such as the energy gap of semiconductors, the method can still be used to successfully compare and/or rank the underestimated values to draw useful conclusions in research.

1.4 Self-Consistent Field Theory

DFT utilizes a specific algorithm termed the self-consistent field theory which was designed to break the never ending cycle of solving for the ground-state electron density.

$$\rho_0(\vec{r})$$

$$v_{KS}(\vec{r})$$

$$\left[-\frac{1}{2}\nabla^2 + v_{KS}(\vec{r})\right]\psi_i = \varepsilon_i\psi_i$$

$$\rho(\vec{r}) = \sum_i^M |\psi_i(\vec{r})|^2$$

Convergence?

no

yes

END
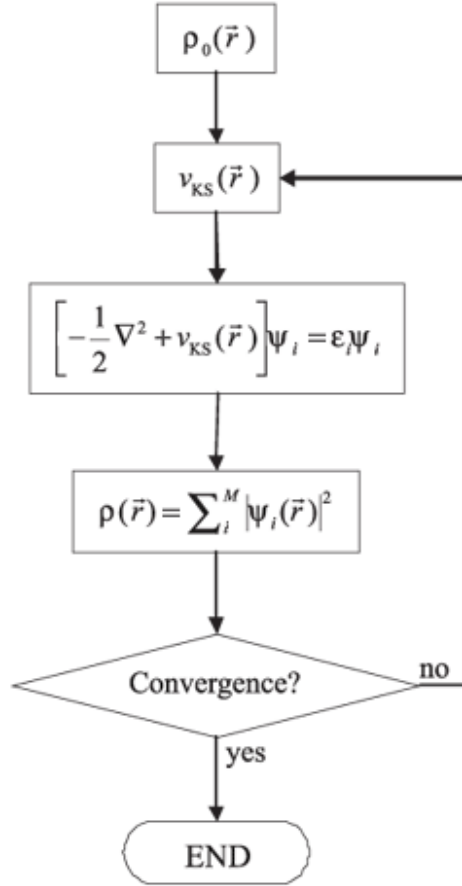
Figure 1.5: Basic algorithm for the self-consistent field theory[87]

Figure 1.5 above outlines the basic steps of the algorithm. An initial trial electron density must be defined and by using this trial electron density, the KS equations can be solved to obtain the single electron wave functions. Start by calculating the electron density defined by the KS single electron wave functions obtained from the previous step. Next, compare this electron density with the initial electron density used to solve the KS equations. These steps are repeated until the changes between the calculated electron density and the initial electron density are smaller than a specified threshold. When the two densities are considered the same, then this value represents the ground-state electron density which can be used to calculate the total energy.[68]

Chapter 2: Computational Modelling of the CdSe Crystal Lattice

CdSe QD's are noted as one of the most extensively investigated II-VI semiconducting nanoparticles.[88] They have become popular candidates used for biomedical applications such as photo-thermal cancer therapy[89-91] and biomedical imaging,[92] as well as for optoelectronic applications ranging from solar energy conversion products[93] to light emitting diodes.[94]

2.1 Research Objectives

The main objective of this chapter is to establish a computational model for a CdSe QD that accurately represents CdSe QD's that are obtainable via experimental synthesis methods. Having a model that is representative of synthetic QD's will allow for a direct comparison of the computational results obtained in this thesis to previously published experimental research studies. A secondary objective is to use the established CdSe model to investigate what the impact is of adding a single silver cation, Ag^+, to the CdSe lattice on the overall structural energy of the QD as well as the HOMO-LUMO gap. In order to investigate both doping styles, an Ag^+ ion will be placed separately within the interstitial spaces of the lattice as well as substituted into the position of a Cd atom.

2.2 Computational Method

ChemCraft is a quantum chemistry visualization software package that was used for displaying 3-dimensional images of the CdSe QD as well as all the atomic coordinates associated with the structure. This commercial software allows for the modification of molecular geometry at the hands of the user and offers a variety of customizable features.

DFT was the modelling method used for all electronic structure calculations. Specifically, the Gaussian and Plane Waves (GPW) method was employed which solves numerically the self-consistent Kohn-Sham equations and is best suited for large, dense systems like solids and liquids. The electrons around each nuclei were described using Goedecker-Teter-Hutter (GTH) pseudopotentials, the exchange-correlation functional applied was PBE, and the basis set used was DZVP-MOLOPT. DZVP stands for "double-zeta valence polarized" which signifies that there are 2 contracted Slater functions per orbital plus one set of polarization functions, and MOLOPT basis sets are optimized from molecular calculations. All simulations in this chapter were performed at 0 K. Finite temperature calculations will be presented in future chapters.

All calculations were completed through the quantum chemistry software package, CP2K. This freely available software package performs simulations of molecular systems and provided data on structural energies and HOMO-LUMO gaps for the CdSe QD. CP2K was accessed through SciNet, one of the largest computational resource centers in Canada.

2.3 Results and Discussion

2.3.1 CdSe Quantum Dot Geometry

The CdSe QD can present itself in 3 different forms: halite, sphalerite, and wurtzite. Both halite and sphalerite are classified under the cubic crystal system as each of their two atom types form a separate face-centered cubic lattice. The sphalerite form is known to be unstable and will readily convert into the wurtzite structure via the addition of heat, and the halite form is known to exist only under extreme pressure. The wurtzite crystal lattice is the most commonly observed form for CdSe QD's and falls within the hexagonal crystal system.

The CdSe QD structure chosen for this research project is in wurtzite form and consists of 59 cadmium atoms (red) and 50 selenium atoms (blue), as shown in Scheme 2.1. It has a diameter of approximately 1.8 nm, the Cd-Se bond lengths vary between 2.5 Å and 2.8 Å, and the overall charge is +18.
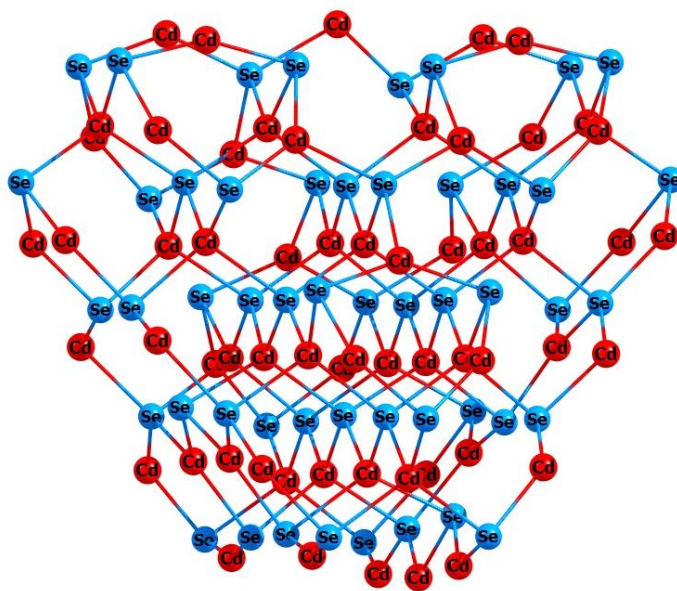
Scheme 2.1: CdSe crystal lattice in wurtzite form consisting of 109 atoms; 59 cadmium (red) and 50 selenium (blue).

2.3.2 Surface Passivation

QD's are known for their minute size and for having an enormous surface-to-volume ratio. They are often capped with surface agents known as ligands which are well known for their crucial part in QD synthesis as they aid in controlling nucleation and growth rate, shape, and size.[95-100] Aside from their role in the synthesis process, surface ligands have also been known to increase luminescence properties as well as the electrical conductivity of CdSe QD's.[101-103] Common surface ligands known to enhance properties of CdSe QD's are: alkylamine, trioctylphosphine (TOP), trioctylphosphine oxide (TOPO), and triphenylphospine (TPP).[101,104]
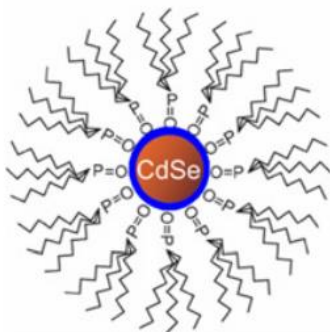
Figure 2.1: A CdSe core encompassed in a ZnS shell capped with trioctylphosphine oxide (TOPO) ligands.[105]

As stated in the previous section, the charge of the bare QD was reported at +18, a result of the fact that there are 9 more cadmium atoms present than selenium atoms. Aside from their property enhancing abilities, ligands were added to the surface of the CdSe QD in order to gain charge neutrality. The decision of which ligand to add was largely influenced by computational cost since the addition of electrons to the system will increase the run time. To put this into perspective, doubling the amount of electrons in the system will increase the run time by a factor

of 8. As shown in Figure 2.1, TOPO is a well-known ligand however is extremely large and complex; adding numerous ligands of this size would make the structure too computationally expensive. In attempts to keep things realistic but on a smaller scale, the acetate ion ($C_2H_3O_2^-$) was chosen and 18 ligands were bound to the surface via cadmium atoms as shown in Scheme 2.2.
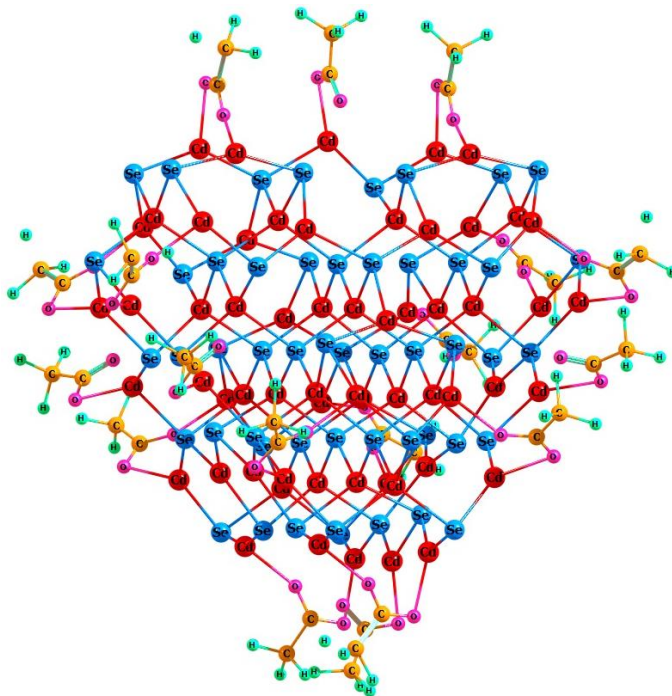
Scheme 2.2 $Cd_{59}Se_{50}$ QD capped with 18 acetate ligands.

This new structure now has an overall charge of 0, consists of 235 atoms, and has an approximate diameter of 2.4 nm.

The first calculations performed were to obtain the structural energy values of the $Cd_{59}Se_{50}^{+18}$ and $Cd_{59}Se_{50}Ac_{18}$ QD's in order to gage the effects of adding ligands to the surface. It was expected that the $Cd_{59}Se_{50}Ac_{18}$ QD would have a lower structural energy value as ligands are known to increase the overall stability. Table 2.1 in Appendix A contains the structural energy values for the bare and capped QD's. The

value corresponding to the bare QD is the summation of the energy value for the $Cd_{59}Se_{50}^{+18}$ structure and the energy value for 18 acetate ions. The energy value for the capped QD was determined to be roughly 300 eV more negative than the bare QD which coincides with previous expectations that it is favourable for the QD to be capped with ligands.

2.3.3 Interstitial Doping

The cavities that make up the $Cd_{59}Se_{50}Ac_{18}$ QD are hexagonal in shape with a width of just under 5 Å. Since the atomic diameter of Ag^+ is 2.58 Å, it is physically possible for Ag^+ ions to make their way into the spaces of the lattice. To begin analysis on interstitial doping, Ag^+ was placed separately in 3 different locations in the $Cd_{59}Se_{50}Ac_{18}$ structure: on the surface, midway into the lattice, and at the core (see Appendix A, Schemes 2.3-2.5). The addition of the Ag^+ ion caused a charge imbalance, therefore a chlorine atom was added to the surface of the $Cd_{59}Se_{50}Ac_{18}$ QD. Chlorine was chosen since it is often used as a ligand in QD synthesis and AgCl is both experimentally and computationally inexpensive. The balanced chemical reaction is as follows:

$$Cd_{59}Se_{50}Ac_{18} + AgCl \rightarrow Cd_{59}AgSe_{50}Ac_{18}Cl \qquad \text{(Eqn. 2.1)}$$
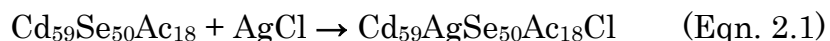
Based on published results by Norris *et al.* it was expected that the three doped structures be more stable than the undoped counterpart regardless of where the Ag^+ ion was located within the lattice. It was also anticipated that the structure with Ag^+ on the surface be more energetically favourable than the other two locations based on

a process known as "self-purification", where the impurity atoms are expelled to the surface.

As shown in Figure 2.2 below, all three doped structures are in fact more energetically favourable than the undoped counterpart by more than 1 eV (see Appendix A, Table 2.2). The energy value corresponding to the undoped structure is the summation of the energy value for the $Cd_{59}Se_{50}Ac_{18}$ structure and the energy value for AgCl. Also as expected, the structure with the Ag^+ surface site location is approximately 1 eV more negative than the other two doped structures.
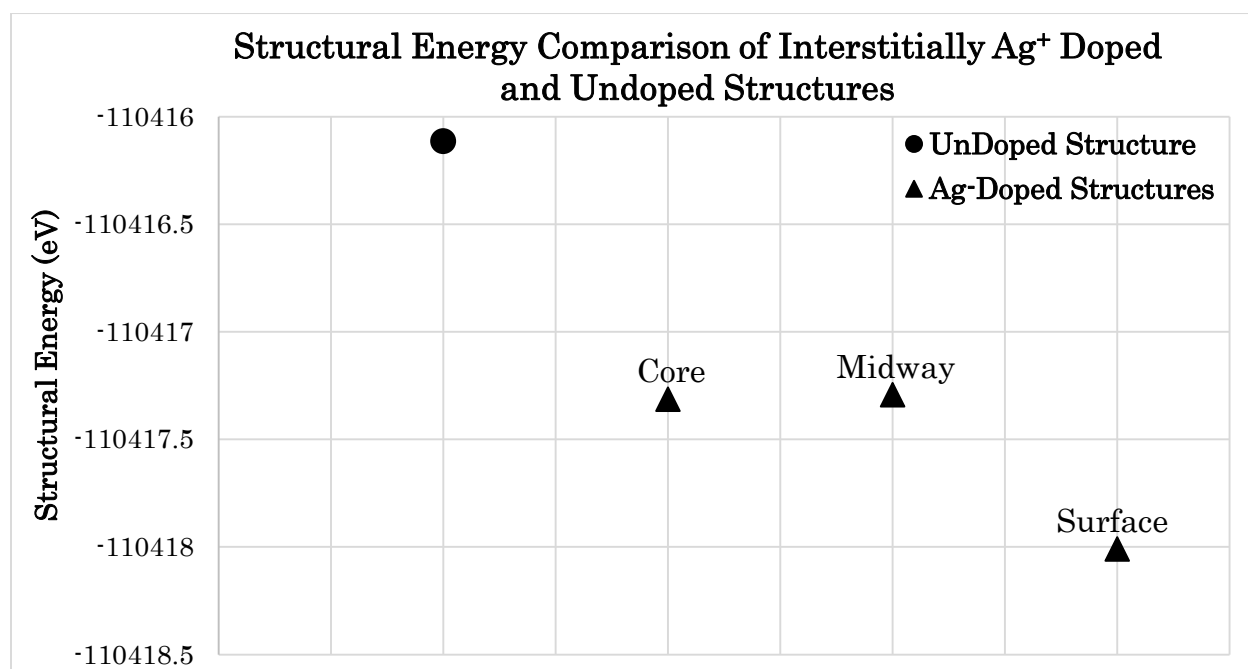
Figure 2.2: Structural energy values (eV) at 0 K for $Cd_{59}Se_{50}Ac_{18}$ QD (●) and three $Cd_{59}AgSe_{50}Ac_{18}Cl$ QD's (▲), where the Ag^+ ion was placed on the surface, midway into the lattice, and at the core.

Before analysis of the HOMO-LUMO gaps was completed, it was expected that there would be a noticeable shift in the gap values when comparing the three doped structures to the undoped QD as it is known that doping alters luminescence

properties.[43] It was also predicted that since the doped QD with the Ag$^+$ surface site had the most negative structural energy value, its HOMO-LUMO gap would be slightly larger in size compared to the other two doped structures.[106] The same rationalization was applied to the doped QD with the Ag$^+$ ion located midway in the lattice; having the most positive structural energy value of the doped structures should result in the smallest HOMO-LUMO gap. Figure 2.3 contains the HOMO-LUMO gap data which coincides with former expectations that a slight shift in values be observed. Comparing the undoped structure to the three doped structures, there is a decrease in gap value by 0.2-0.6 eV upon doping. Comparing only doped structures, it was also noted that the doped QD with the Ag$^+$ surface site does in fact have a slightly larger HOMO-LUMO gap, and the doped QD with the Ag$^+$ midway site has the smallest (see Appendix A, Table 2.3).
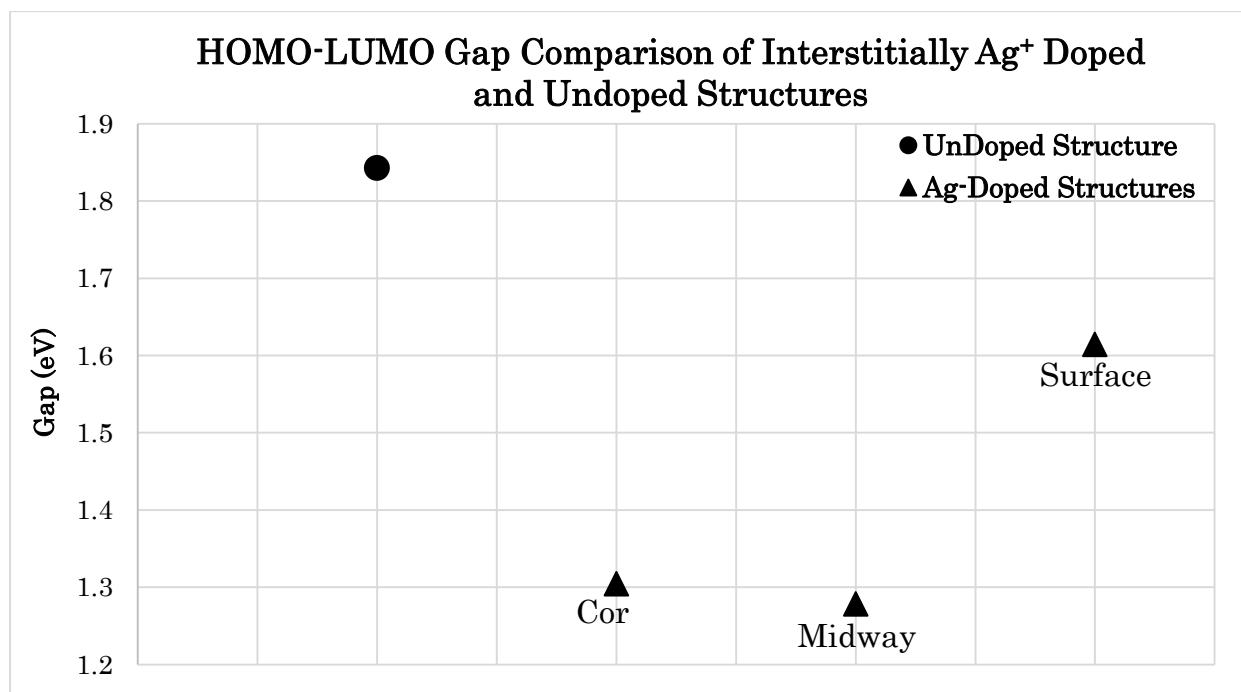
Figure 2.3: HOMO-LUMO gap values (eV) at 0 K for Cd$_{59}$Se$_{50}$Ac$_{18}$ QD (●) and three Cd$_{59}$AgSe$_{50}$Ac$_{18}$Cl QD's (▲), where the Ag$^+$ ion was placed on the surface, midway into the lattice, and at the core.

2.3.4 Substitutional Doping

Previous experimental studies were successful in incorporating Ag atoms into semiconducting nanocrystalline lattices via substitution of core atoms for Ag ones.[59,60] For this computational study, six CdSe doped structures were created: two with the Ag^+ ion substituted at the core, one with the Ag^+ ion substituted midway in the lattice, and three with the Ag^+ ion substituted at the surface (see Appendix A, Schemes 2.6-2.8). The substitution of Cd^{2+} for Ag^+ created a charge imbalance, so in order to maintain charge neutrality a single acetate ligand was removed from the surface. The balanced chemical reaction is as follows:

$$Cd_{59}Se_{50}Ac_{18} + AgCl \rightarrow Cd_{58}AgSe_{50}Ac_{17} + Cd^{2+} + Ac^- + Cl^- \qquad \text{(Eqn. 2.2)}$$

Recent publications have noted that heavily doping inorganic semiconducting nanocrystals with Ag^+ ions causes a decrease in the Fermi level of the system which is characteristic of substitutional doping. Since this computational study is focusing on doping with only a single Ag^+ ion, it was expected that the six substitutionally doped $Cd_{58}AgSe_{50}Ac_{17}$ QD's have structural energy values less negative than their undoped counterpart. Figure 2.4 contains the structural energy trend for substitutional doping and supports the claims made in the literature that lightly doping via a substitutional process is not favourable as all six lightly doped structures are less energetically favourable than their undoped counterpart (see Appendix A, Table 2.4). The energy value corresponding to the undoped structure is the summation of the energy value for the $Cd_{59}Se_{50}Ac_{18}$ structure and the energy value for AgCl. The energy values corresponding to the six doped structures are the

summation of the energy values for $Cd_{58}AgSe_{50}Ac_{17}$, Cd^{2+}, Ac^-, and Cl^-. When comparing the six doped structures, two out of the three structures with the Ag^+ substitution site on the surface were the most energetically favourable and it should be noted that this same trend was observed for the interstitial doping case.
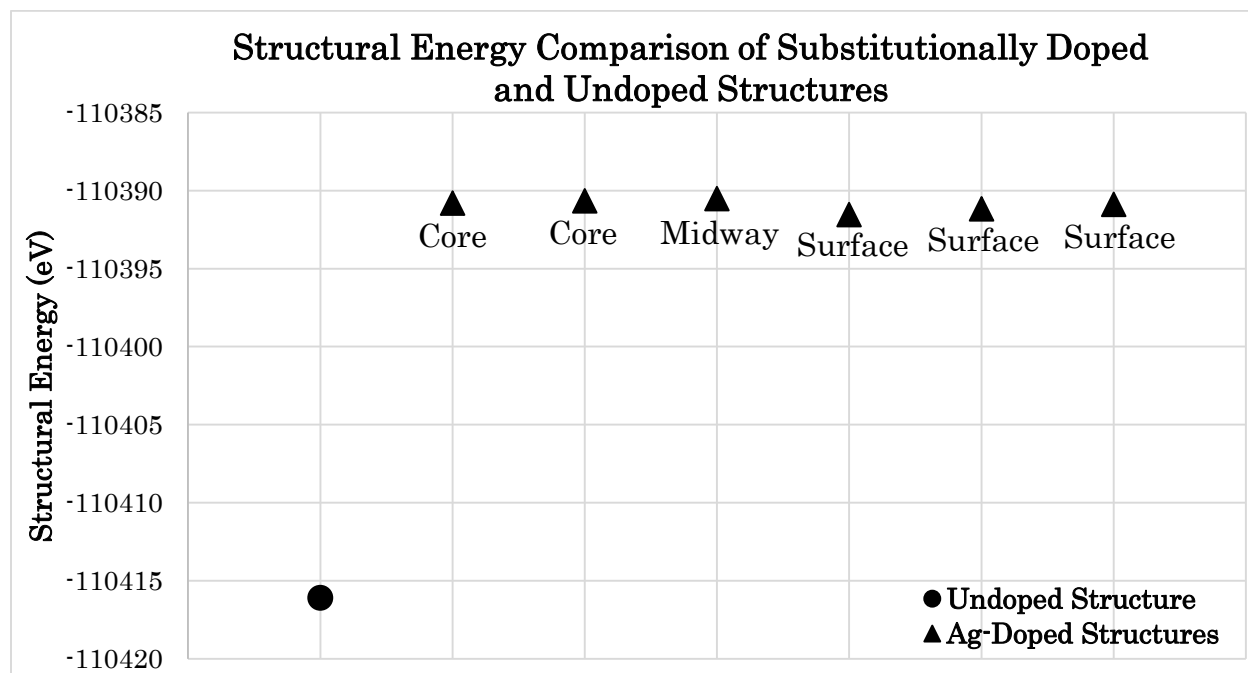
Figure 2.4: Structural energy values (eV) at 0 K for $Cd_{59}Se_{50}Ac_{18}$ QD (●) and six $Cd_{58}AgSe_{50}Ac_{17}$ QD's (▲), where the Ag^+ ion was substituted in on the surface, midway into the lattice, and at the core.

As stated in section 2.3.3, a shift in HOMO-LUMO gap values is to be expected for structures that have undergone impurity doping. Figure 2.5 contains the HOMO-LUMO gap data and like the interstitial doping case presented previously, there is a shift in values upon doping. When comparing the six doped structures to the undoped structure, there is a decrease in gap value by 0.004-0.7 eV (see Appendix A, Table 2.5). Out of the six doped structures, the surface site structure with the most negative structural energy value has the highest HOMO-LUMO gap value, and the midway

surface site structure with the least negative structural energy value has to smallest

gap value. This same trend was observed in the interstitial doping case.
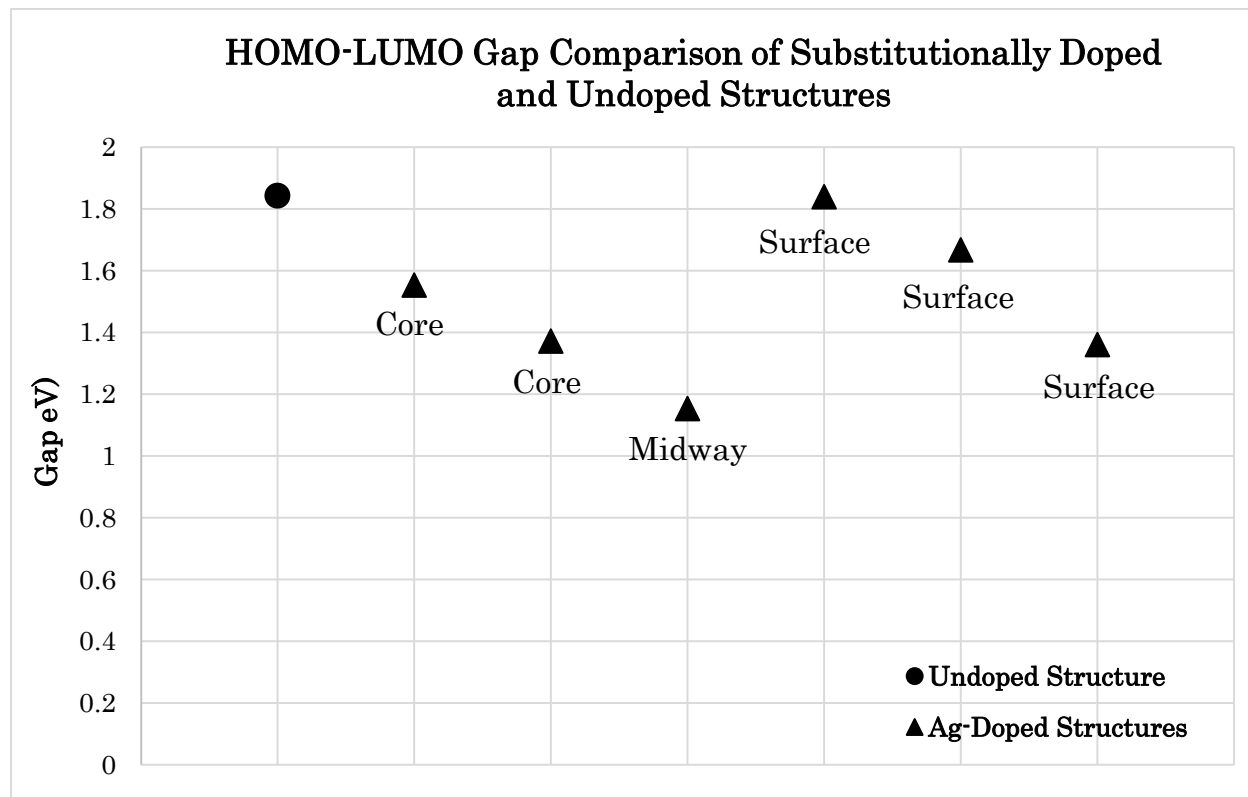
Figure 2.5: HOMO-LUMO gap values (eV) at 0 K for Cd$_{59}$Se$_{50}$Ac$_{18}$ QD (●) and six Cd$_{58}$AgSe$_{50}$Ac$_{17}$ QD's (▲), where the Ag$^+$ ion was placed on the surface, midway into the lattice, and at the core.

2.4 Conclusions

In conclusion, the main objectives of this chapter were successfully met as a computational model for a realistic CdSe QD was constructed and interstitial and substitutional impurity doping was investigated. The size of the QD is on the lower end compared to the CdSe QD's synthesized by Norris *et al.*, however, the bond lengths between cadmium and selenium for the computational QD are around 2.6 Å which is in agreement with literature claims for experimentally synthesized CdSe QD's in wurtzite form.[107] The QD consists of 59 cadmium atoms and 50 selenium

atoms with 18 acetate ligands protruding from the surface. With a diameter of 2.4 nm and an overall neutral charge, this fabricated QD is considered a stable structure. Using the structural energy values presented in this chapter for both doping cases, formation energies were calculated based on Eqn. 2.1 and Eqn. 2.2 (see Appendix A, Table 2.6 and Figure 2.6). All the formation energies for the six substitutional cases are positive and therefore unfavourable, and all the formation energies for the three interstitial cases are negative and therefore favourable. Moving forward, only interstitially doped $Cd_{59}Se_{50}Ac_{18}$ QD's will be investigated with an Ag^+ ion located solely in surface sites.

Chapter 3: Influence of Ag-Cl Distance on the Doped CdSe Quantum Dot

3.1 Research Objectives

The main objective of this chapter is to investigate if the distance between the Ag^+ and Cl^- ions influences structural energy and the HOMO-LUMO gap of the $Cd_{59}Se_{50}Ac_{18}$ QD. As concluded in the previous chapter, only surface sites will be utilized when constructing the doped $Cd_{59}Se_{50}Ac_{18}$ QD's and locations will be chosen at random. Although the surface of the undoped QD is already covered with 18 acetate ligands, there is still ample space to add the two ions and create an overall picture which includes a variety of Ag-Cl distances.

3.2 Computational Method

ChemCraft was used for displaying 3-dimensional images of the CdSe QD as well as all the atomic coordinates associated with the structure. By knowing the atomic coordinates, ChemCraft is also able to produce the exact distances in units of angstroms between any atoms chosen by the user.

All electronic structure calculations were performed at 0 K and were completed through the quantum chemistry software package, CP2K. The modelling method used was DFT, specifically the Gaussian and Plane Waves (GPW) method. The electrons around each nuclei were described using Goedecker-Teter-Hutter (GTH) pseudopotentials, the exchange-correlation functional applied was PBE, and the basis set used was DZVP-MOLOPT.

3.3 Results and Discussion

3.3.1 Distance Effects on Structural Energy

In an attempt to gain a thorough understanding of how the distance between the Ag^+ and Cl^- ions effects structural energy, twenty different $Cd_{59}AgSe_{50}Ac_{18}Cl$ structures were created with varying Ag-Cl distances (see Appendix B, Schemes 3.1-3.20). The smallest distance achieved was 4.89 Å as Ag^+ and Cl^- were bound to the surface via neighbouring Cd-Se atoms. Since the diameter of the bare CdSe QD is approximately 18 Å, the largest distance obtainable was 18.77 Å as Ag^+ and Cl^- were bound to the surface on opposite ends of the structure.

Figure 3.1 contains the formation energy data calculated by using the interstitial doping chemical reaction equation:

$$Cd_{59}Se_{50}Ac_{18} + AgCl \rightarrow Cd_{59}AgSe_{50}Ac_{18}Cl \qquad \text{(Eqn. 3.1)}$$
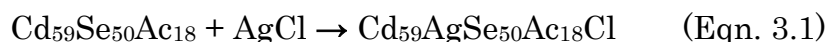
All twenty structures have negative formation energy values which was expected based on the data outlined in Chapter 2. The general trend amongst the data is that as the distance between Ag^+ and Cl^- increases, the formation energy becomes less negative (see Appendix B, Table 3.1). A linear line of best fit was added to Figure 3.1 and the reported coefficient of determination (R^2) value is 0.4558. A factor impacting the R^2 value is the wide spread of formation energies for structures with similar Ag-Cl distances. For example, four doped structures were created with Ag-Cl distances between 8.81-8.97 Å. After optimization, one of the structures has a formation energy that is roughly 1.05 eV more positive than the other three. Also, two structures with

similar Ag-Cl distances of 11.72 Å and 12.43 Å have a formation energy difference of almost 0.7 eV.
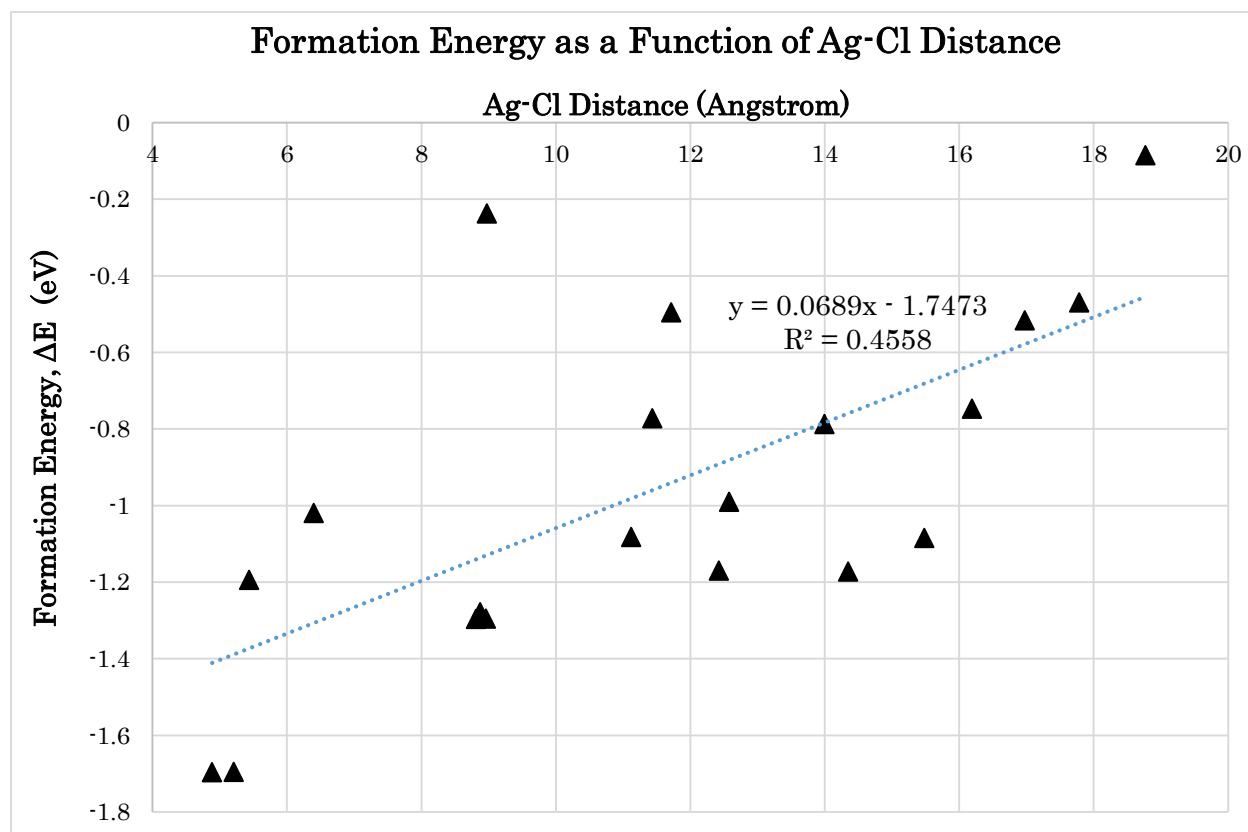
Figure 3.1: Formation energy, ΔE, values (eV) at 0 K for twenty interstitially doped $Cd_{59}AgSe_{50}Ac_{18}Cl$ QD's with varying Ag-Cl distances (Å).

3.3.2 Distance Effects on the HOMO-LUMO Gap

Before completing an in-depth analysis of the twenty HOMO-LUMO gaps, it was expected as before that the structures with the most negative formation energy have the largest gaps and those with the least negative formation energy have the smallest. Figure 3.2 displays the relationship between the Ag-Cl distances and the HOMO-LUMO gaps which coincides with our expectations; the structures with the smallest Ag-Cl distance have the largest gaps and the ones with the largest distances

have the smallest gaps (see Appendix B, Table 3.1). A linear line of best fit was added

to Figure 3.2 and the reported coefficient of determination (R^2) value is 0.6025. As

mentioned in the previous section, the R^2 value is a reflection of the broad range of

results for structures with similar Ag-Cl distances. The two structures with the Ag-

Cl distances of 11.72 Å and 12.43 Å with the formation energy difference of almost

0.7 eV have gap values of 1.1 eV and 1.6 eV, respectively.
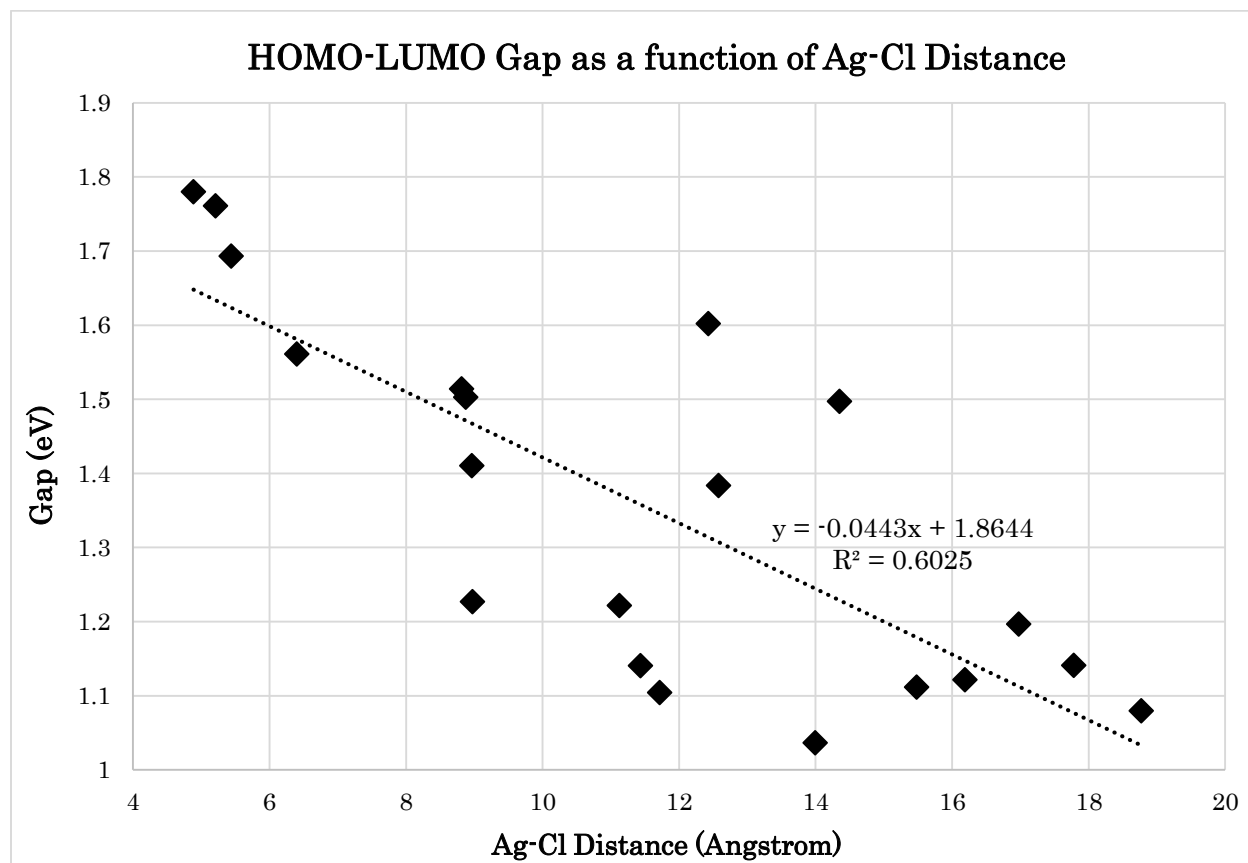
Figure 3.2: HOMO-LUMO gap values (eV) at 0 K for twenty interstitially doped Cd$_{59}$AgSe$_{50}$Ac$_{18}$Cl QD's with varying Ag-Cl distances (Å).

3.4 Conclusions

In conclusion, the objective of this chapter was successfully met as it was proven that the Ag-Cl distance does play a role in altering the properties of the $Cd_{59}AgSe_{50}Ac_{18}Cl$ QD at 0 K. It was determined that structures with smaller Ag-Cl distances are more energetically favourable than the ones with larger distances, and that Ag-Cl distance and HOMO-LUMO gap value have an inversely proportional relationship. It is not yet fully understood why or how the distance between Ag^+ and Cl^- is effecting the QD's properties. For all twenty structures analyzed, the base $Cd_{59}AgSe_{50}Ac_{18}$ QD is exactly the same. The only changing factor is the locations of the Ag^+ and Cl^- ions, therefore it is quite clear that further theoretical work is needed in order to understand this specific aspect of impurity doping in CdSe QD's.

Chapter 4: Temperature Impact on the Doped CdSe Quantum Dot

4.1 Research Objectives

The main objective of this chapter is to incorporate a temperature factor into the CdSe QD system and to investigate how the structural energy and HOMO-LUMO gap is impacted. All previous portions of this thesis were conducted at 0 K, or absolute zero, where it is understood that entropy is zero as all molecular motion has been halted. Taking a step towards practical experimental conditions, numerous structures from Chapter 2 will be chosen to have their temperatures raised to 333 K; a value chosen based on the Ag$^+$ doping procedure outlined by Norris *et al.* (2012).

4.2 Computational Method

Since temperature was applied to the systems, the modelling method specifically utilized in this chapter was Born-Oppenheimer molecular dynamics (BOMD). All electronic structure calculations were performed at 333 K through the quantum chemistry software package, CP2K. The electrons around each nuclei were described using Goedecker-Teter-Hutter (GTH) pseudopotentials, the exchange-correlation functional applied was PBE, and the basis set used was DZVP-MOLOPT. The time step applied to each system was 0.5 fs per step and each structure was run for 9585 fs to ensure enough data points could be collected for a detailed analysis of the HOMO-LUMO gaps and structural energy values.

The visualization software packed used was ChemCraft which displayed 3-dimensional images of the CdSe QD's as well as the distances between any selected

atoms. Through ChemCraft, the CdSe structure can be viewed and investigated at each time step.

4.3 Results and Discussion

Ten out of the twenty structures presented in Chapter 2 were chosen to have their temperatures raised to 333 K. Four structures were chosen for having the smallest Ag-Cl distances at 0 K (see Appendix C, Schemes 4.1-4.4), two were chosen for having the largest Ag-Cl distances at 0 K (see Appendix C, Schemes 4.5-4.6), and four were chosen because of their wide spread in results at 0 K for similar Ag-Cl distances (see Appendix C, Schemes 4.7-4.10).

At first, the temperature was initially set for 333 K. However, upon inspection of the structures in CP2K it was discovered that the temperature was too high and atoms were ejecting out of the crystal lattice. To overcome this issue, the structures were run in a "temperature work-up" approach starting with 50 K and with a temperature increase of 50 K until 333 K was reached. This method proved successful as all atoms stayed intact until the final step of 9585 fs was achieved.

4.3.1 Temperature Impact on Ag-Cl Distance

After optimization at 333 K, it was noted that some of the Ag-Cl distances for the ten chosen structures had changed. Since the calculations performed at 333 K are of "never-ending" type, the Ag-Cl distances at 9000 fs were chosen to be compared to the distances at 0 K. After roughly 1000 fs the data leveled out (see Appendix C,

Figure 4.5) and stayed level with no dramatic increase or decrease well beyond the 9000 fs mark. The 9000 fs mark was chosen because the structures had been running at 333 K for close to 8000 fs with no dramatic change in the structural energy values. Table 4.1 contains the Ag-Cl distances for the ten doped structures at 0 K as well at 333 K, at the 9000 fs mark. Some major changes observed were an increase from 5.21 Å to 10.68 Å and a decrease from 18.77 Å to 13.20 Å. All other changes were noted as minor as they differed by 1 Å or less.

Structure	Ag-Cl Distance (Å) at 0 K	Ag-Cl Distance (Å) at 333 K, at 9000 fs
1	4.89	4.94
2	5.21	10.68
3	5.44	5.31
4	6.40	7.09
5	17.78	16.76
6	18.77	13.20
7	8.88	8.21
8	8.97	8.52
9	11.43	11.43
10	11.72	11.97

Table 4.1: Ag-Cl distances (Å) for ten interstitially doped CdSe QD's at 0 K and 333 K.

4.3.2 Temperature Impact on Structural Energy

With the new factor of temperature added to the ten structures, it was expected that there be some variation in the structural energy results when compared to the results presented previously at 0 K. Figure 3.1 from Chapter 3 demonstrated that as the Ag-Cl distance decreased, the formation energy became more negative. Figure 4.1 contains the structural energy values at 333 K for ten doped structures as well as the

undoped QD over a time period of 1900 fs. As expected, all ten doped structural energy values are more negative than the undoped structure, however, the trend outlined in Figure 3.1 regarding Ag-Cl distance and structural energy is not evident. The QD with the largest Ag-Cl distance of 16.76 Å at 9000 fs is one of the most stable structures within the data set, and the QD with an Ag-Cl distance of only 8.52 Å at 9000 fs is the least stable.

Figure 4.1: Structural energy values (eV) at 333 K for the undoped $Cd_{59}Se_{50}Ac_{18}$ QD and ten interstitially doped $Cd_{59}AgSe_{50}Ac_{18}Cl$ QD's with varying Ag-Cl distances (Å).

In order to visualize the presence and absence of trends more clearly, separate figures were created containing data for selected structures. Figure 4.2 contains the formation energy data at 333 K for the structures with the two smallest Ag-Cl distances and the two largest Ag-Cl distances. The linear trend observed in Chapter 3 at 0 K is no longer present at 333 K. Although the formation energy for the smallest Ag-Cl distance is the most negative, the second smallest distance is the most positive in this data set. Also, the formation energy for the structure with the Ag-Cl distance at 16.76 Å is more negative than the smaller distance of 13.20 Å.
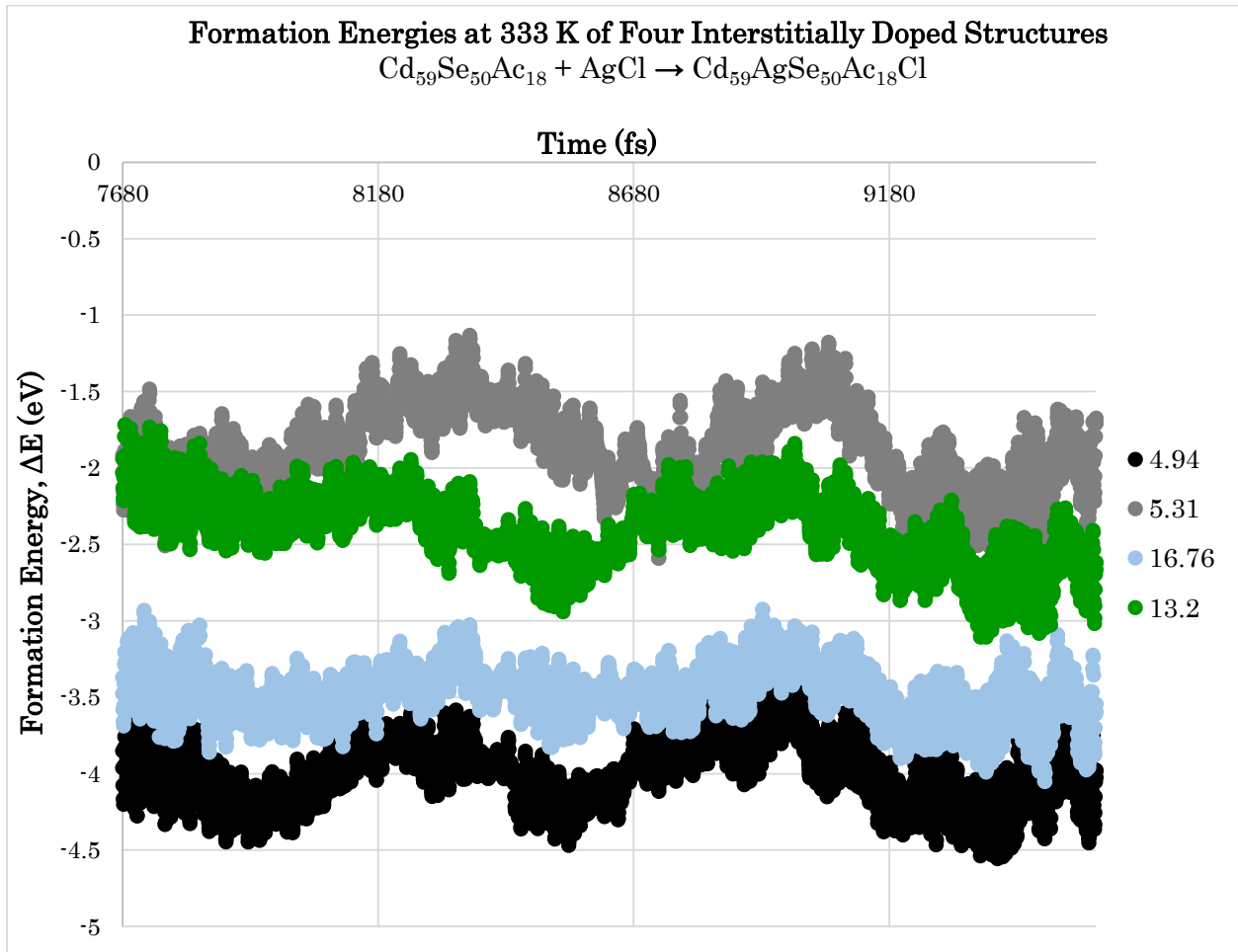
Figure 4.2: Formation energy, ΔE, values (eV) at 333 K for four interstitially doped Cd₅₉AgSe₅₀Ac₁₈Cl QD's with Ag-Cl distances of 4.94 Å, 5.31 Å, 16.76 Å, and 13.20 Å.

Figure 4.3 contains the formation energy values at 333 K for four structures with Ag-Cl distances of 8.21 Å, 8.52 Å, 11.43 Å, and 11.97 Å. These four structures also do not demonstrate the linear trend observed at 0 K since both structures with larger Ag-Cl distances are more energetically favourable. However, if comparing the structures with an approximate Ag-Cl distance of 8 Å together and the two with an approximate distance of 11 Å together, the structures with the smaller Ag-Cl distance are more energetically favourable.

Formation Energies for Four Interstitially Doped Structures
$$Cd_{59}Se_{50}Ac_{18} + AgCl \rightarrow Cd_{59}AgSe_{50}Ac_{18}Cl$$
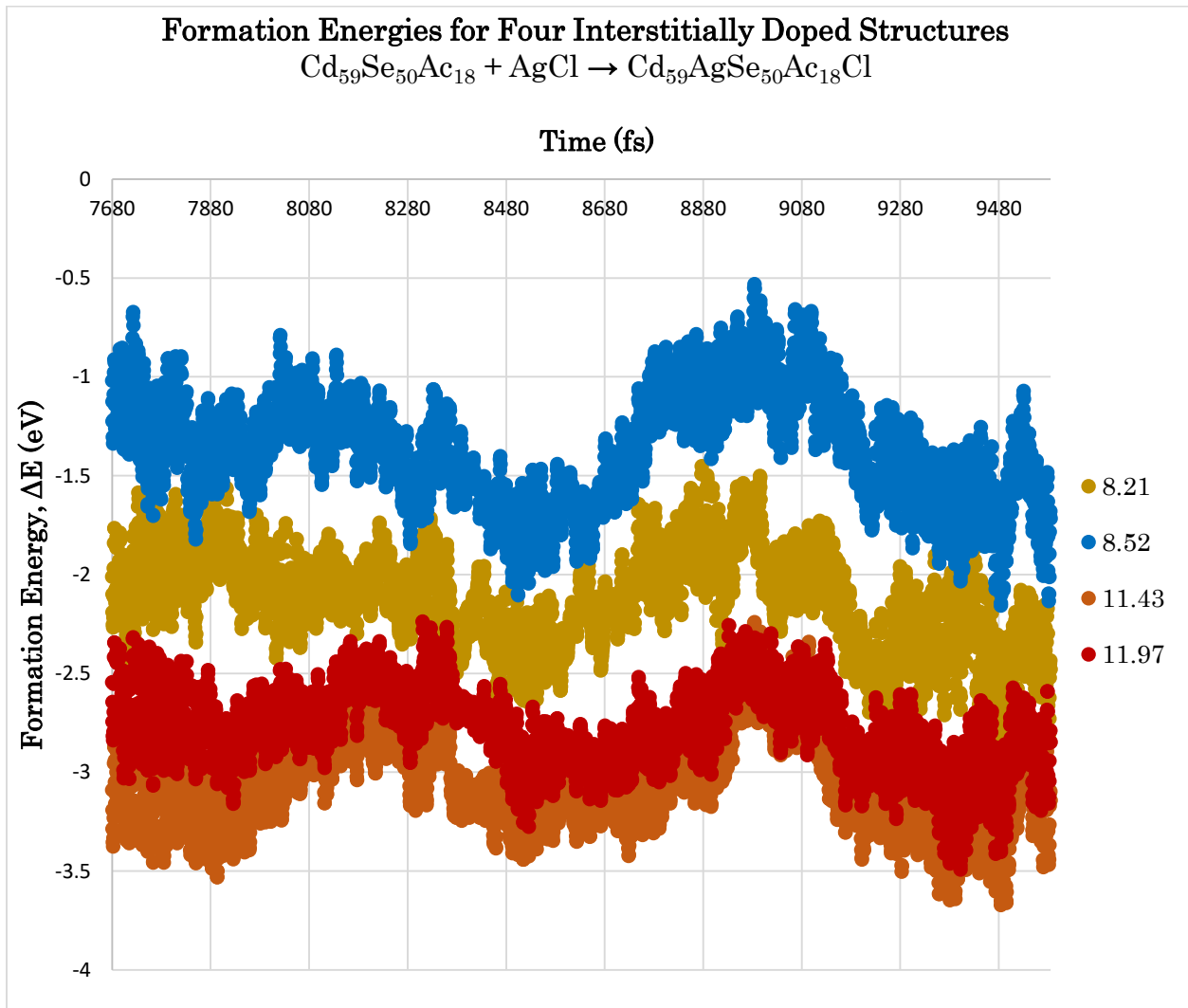
Figure 4.3: Formation energy, ΔE, values (eV) at 333 K for four interstitially doped $Cd_{59}AgSe_{50}Ac_{18}Cl$ QD's with Ag-Cl distances of 8.21 Å, 8.52 Å, 11.43 Å, and 11.97 Å.

4.3.3 Temperature Impact on the HOMO-LUMO Gap

After incorporation of the temperature factor it was still expected, as it was for the 0 K case, that there be a shift in the HOMO-LUMO gap upon doping. Since the structural energies at 333 K did not follow a linear fashion as they did at 0 K, it was predicted that these HOMO-LUMO gaps would not follow a linear trend as well. It was however expected that the structures with the lowest energies have the largest HOMO-LUMO gaps and the ones with the highest energies have the smallest gaps. Figure 4.4 contains the HOMO-LUMO gap data for the ten doped structures as well as the undoped structure over the same time period of 1900 fs. There is no trend observed as the structures with Ag-Cl distances of 4.94 Å and 8.21 Å have the largest HOMO-LUMO gaps, and the structures with Ag-Cl distances of 8.52 Å, 11.43 Å, and 11.97 Å have the smallest gaps. The inversely proportional trend of structural energy and HOMO-LUMO gap is observed but only for some structures. The structure with the lowest energy (Ag-Cl distance of 4.94 Å) does in fact have one of the largest gaps, however the other structure with the largest gap (Ag-Cl distance of 8.21 Å) cannot even be considered in the top five out of ten most energetically favourable structures. The structure with the highest energy (Ag-Cl distance of 8.52 Å) has at times the smallest HOMO-LUMO gap, however the other two structures with the smallest gaps (Ag-Cl distances of 11.43 Å and 11.97 Å) are considered in the top five out ten most energetically favourable structures.

HOMO-LUMO Gaps at 333 K of Ten Interstitially Doped CdSe QD's as a function of Time
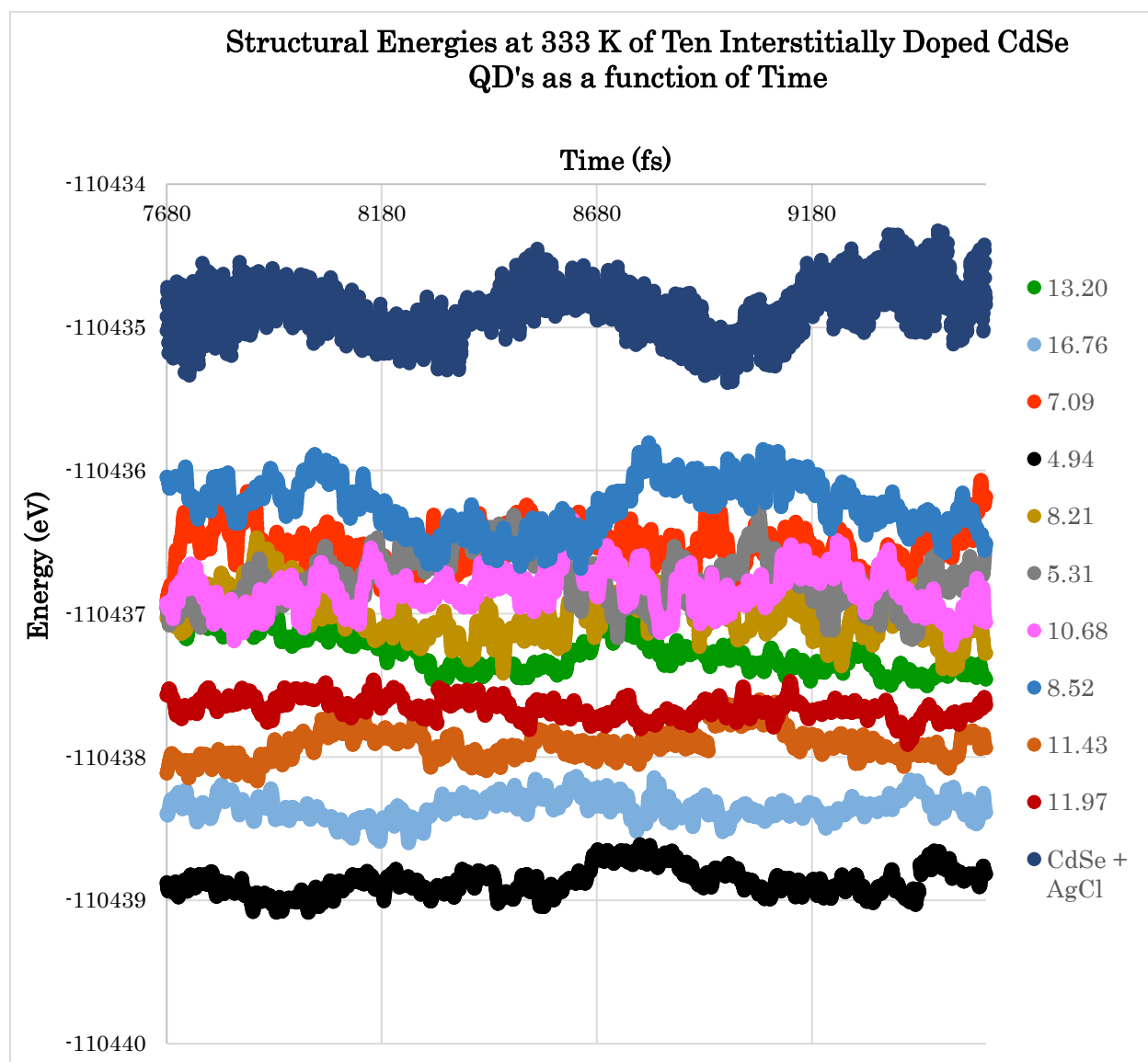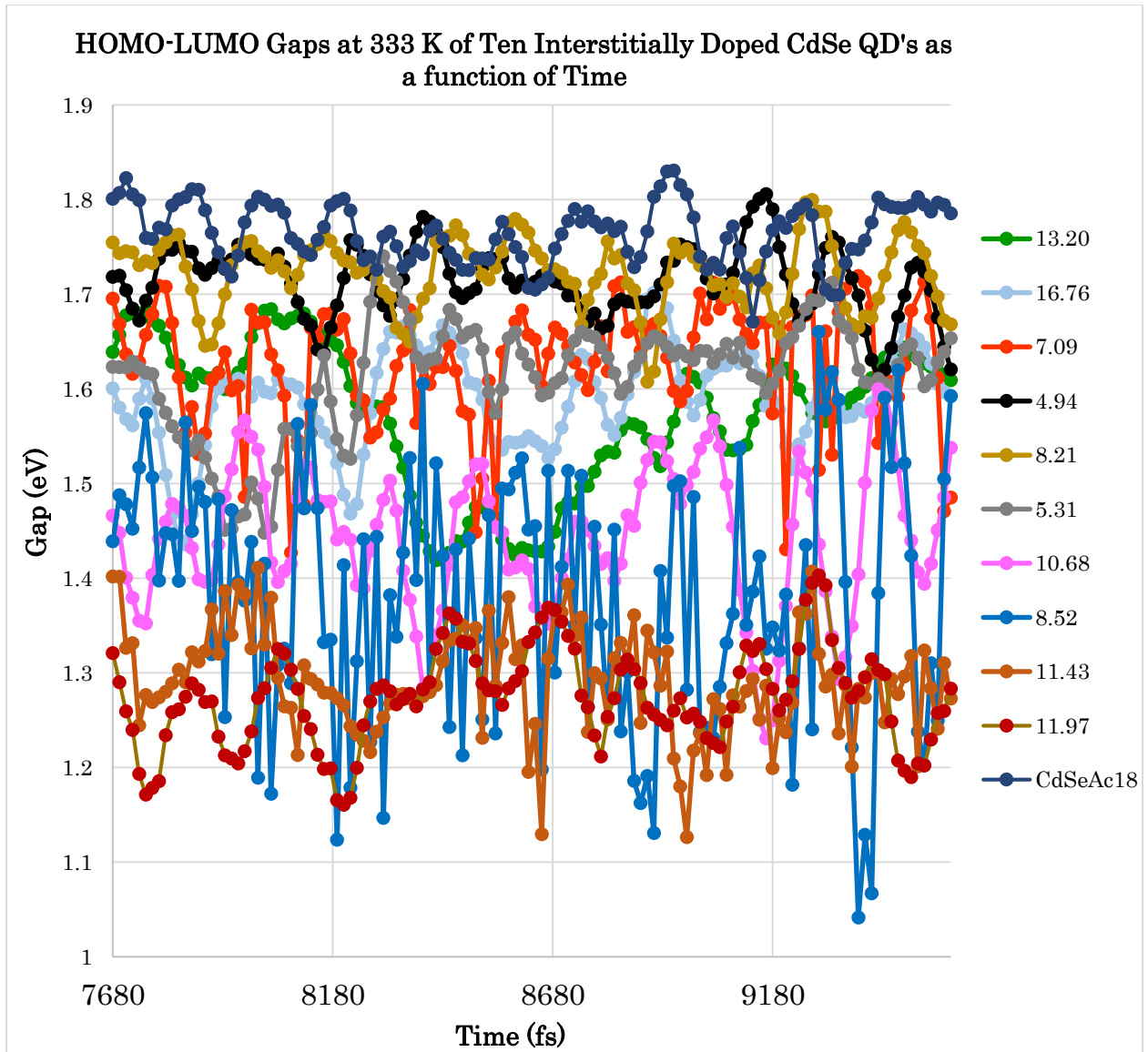
Figure 4.4: HOMO-LUMO gap values (eV) at 333 K for the undoped $Cd_{59}Se_{50}Ac_{18}$ QD and ten interstitially doped $Cd_{59}AgSe_{50}Ac_{18}Cl$ QD's with varying Ag-Cl distances (Å).

4.4 Conclusions

In conclusion, the objective of this chapter was successfully met as it was determined that temperature does play a role in altering the structural energy and HOMO-LUMO gap of ten interstitially doped $Cd_{59}AgSe_{50}Ac_{18}Cl$ QD's. However, unlike the data presented for the 0 K case, there were no definitive trends in both the

structural energy and HOMO-LUMO gap values for the ten structures run at 333 K. Nevertheless, all ten doped structures were more energetically favourable than the undoped counterpart, and there was an observed shift in the HOMO-LUMO gap values upon doping at 333 K. Based on these results alone, it cannot be said with confidence that the properties of the $Cd_{59}Se_{50}Ac_{18}$ QD can be fine-tuned at 333 K by controlling the location of the added AgCl atoms.

Chapter 5: Significance and Future Work

5.1 Summary

The objectives of this thesis project were to gain an understanding of which doping style the CdSe QD undergoes when lightly doped and to investigate how the properties of the CdSe QD are affected by the addition of a single Ag^+ impurity ion.

DFT calculations were carried out for both cases of interstitial and substitutional doping and the formation energies of all the structures were determined. Since the formation energies for the interstitial cases were negative and the substitutional ones positive, it was concluded that CdSe QD's must be undergoing interstitial doping when only a few Ag^+ ions are introduced. Three separate dopant sites were investigated and the most probable location for the Ag^+ ion was determined to be on the surface of the CdSe lattice.

The Ag^+ ion was introduced into the QD system via the addition of AgCl. Upon dissociation, the chlorine atom adopts a formal negative charge and, like the Ag^+ ion, will bind to the surface of the QD. DFT calculations were performed at 0 K on twenty CdSe QD's with varying Ag-Cl distances. It was determined that structures with smaller Ag-Cl distances were more energetically favourable than the ones with larger distances, and that Ag-Cl distance and HOMO-LUMO gap value had an inversely proportional relationship.

The final portion of this thesis involved adding a temperature factor to ten of the twenty structures outlined in the previous section. AIMD calculations were

performed at 333 K and no definitive trends in both the structural energy and HOMO-LUMO gap values for the ten structures was observed.

Regardless of whether the structures were run at 0 K or 333 K, all the doped structures were more energetically favourable than the undoped counterpart. A shift in the HOMO-LUMO gap was also observed for all the reported Ag-Cl distances although it seemed unlikely to be able to control the gap at 333 K. These results coincide with the literature as it is known that doping increases the structural stability and is a successful method for altering the properties of CdSe QD's.

5.2 Significance of Research

Quantum dots are a remarkable nano-sized material as they have the ability to emit photons of various wavelengths when subjected to light of sufficient energy. The colour of light a QD will release is directly related to the size of its HOMO-LUMO gap which today can be fine-tuned at the hands of scientists. Electronic impurity doping is a method used to control and enhance the most desirable properties of a QD by either providing extra electrons or extra holes. Previously published work has successfully investigated the heavily doped limit however the investigation of lightly doping appears somewhat difficult. Norris *et al.* stated that lightly doping a CdSe QD with Ag^+ ions resulted in a dramatic enhancement in properties, however, due to the low concentration of Ag^+, it was impossible to determine the location of the dopants. The objective of this thesis project is to help solve the missing pieces associated with lightly doping CdSe QD's. Gaining an understanding of where the dopant atoms

reside and what factors influence the production of light will be key features in the construction of highly efficient quantum dots.

5.3 Future Work

Although there was a prominent trend in data for the structures at 0 K, there were no trends observed at 333 K for both the structural energies and HOMO-LUMO gaps. It would be interesting to see if any trends were evident at temperature values of 100 K, 273 K, and 300 K. Collectively with data for 5 different temperatures, it may be possible to determine at which temperature the trends begin to disappear.

For simplicity reasons, only one Ag^+ ion was added to the $Cd_{59}Se_{50}Ac_{18}$ lattice in this thesis project. It would be beneficial to run additional simulations at 0 K and above with QD's that have been doped with more than one silver ion. Norris *et al.* reported that approximately 2 silver ions per QD caused the greatest enhancement in fluorescence compared to 0, 4, and 12 silver ions per QD. It would also be helpful to be able to create fluorescence-like spectra from the computational results in order to perform a side by side comparison to experimental data.

Chapter 6: Additional Side Projects

6.1 An Introduction to Localized Surface Plasmon Resonance

When a metallic nanoparticle is subjected to an electromagnetic field of incoming radiation a dipole is formed amongst its movable elementary charges.[108] A restoring force within the nanoparticle attempts to counterbalance the dipole resulting in the oscillation of conduction electrons located at the interface between the metallic nanoparticle and its embedding medium.[108,109] The term localized surface plasmon resonance (LSPR) signifies the elementary excitations occurring on the surface of the metal nanoparticle. The resonance behaviour will determine the optical properties[110] which can be influenced by parameters such as the surrounding dielectric medium,[111] and the shape, size, and material of the nanoparticle.[108] Figure 6.1 illustrates the formation of a dipole and shows the electron cloud for a sphere and a rod oscillating up and down as a result of the alternating electric field.
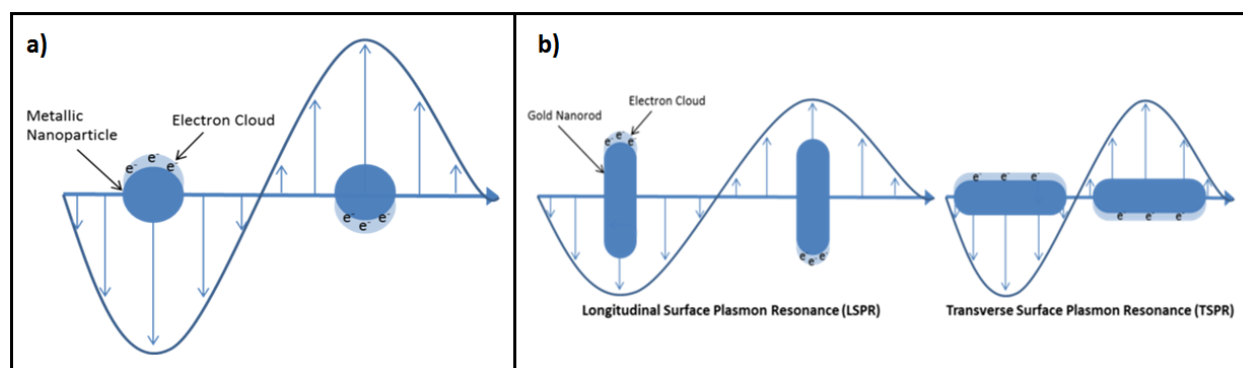

Figure 6.1: Schematic representation of (a) oscillating electron cloud for a sphere, and (b) longitudinal and transverse oscillation of electrons for a nanorod.[112]

As shown in Figure 6.1(a), a sphere is perfectly symmetrical around its center so a nanosphere will have only one unique plasmon resonance wavelength. As outlined in

Figure 6.1(b), since a nanorod is not symmetric around its center it will have two plasmon resonance wavelengths, one for the longitudinal oscillation of electrons and one for the transverse oscillation of electrons.

6.1.1 Gold Plasmonics

A popular material in the emerging field of plasmonics is gold (Au) due to its exceptional catalytic abilities and unique optical properties. The plasmonic resonance for Au is conveniently located within the visible spectrum at a wavelength around 530 nm and can be tuned into the near-infrared portion of the spectrum by altering the nanoparticle shape and size,[113,114] as shown in Figure 6.2.
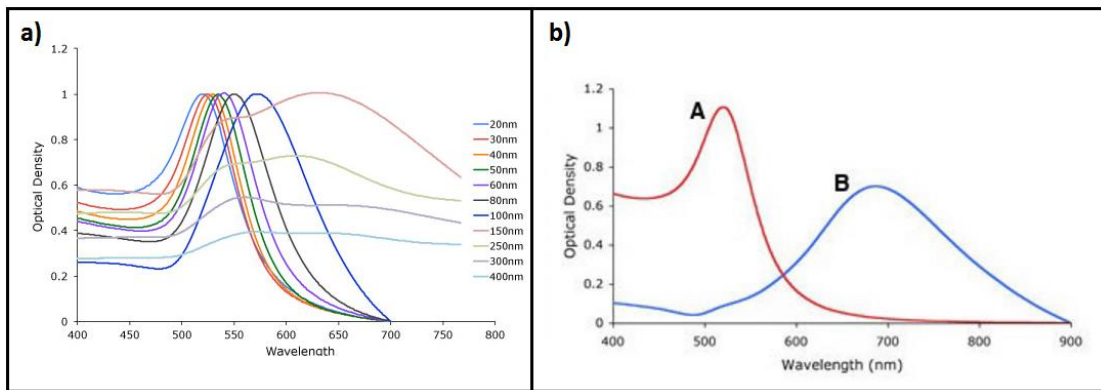

Figure 6.2: Gold plasmonic resonance red-shifting as a result of changing the nanoparticle (a) size, ranging from 20 nm to 400 nm, and (b) shape, where the red line represents a spherical nanoparticle and the blue line represents an urchin-shaped nanoparticle.[114]

6.2 Research Objectives

The main objective of this project is to model plasmonic resonance spectra for metal shapes embedded in water. The specialized Matlab modelling toolbox allows users to see how the alteration of different parameters effects the resonance spectra. The systems to be studied are single Au nanospheres and multiple Au nanospheres

placed in a row. The parameters to be investigated are the diameter of the sphere and the spacing between spheres.

6.3 Computational Method

A Matlab toolbox titled "Metal Nanoparticle Boundary Element Method" (MNPBEM) was, as its name suggests, created for the simulation of the electromagnetic properties of metal nanoparticles utilizing the boundary element method.[110,115] The purpose of the toolbox is to solve Maxwell's equations for objects with homogeneous and isotropic dielectric functions that are embedded in a dielectric medium.[116] The toolbox allows for the user to input parameters such as particle size, dielectric functions, the number of vertices for surface discretization, and the photon energies. Depending on the purpose of the simulations, users can obtain a variety of output data from extinction and scattering cross sectional plots, to computational images of the charges on the particle's surface. Figure 6.3 contained two Au spheres with a generated mesh on their surfaces where the number of vertices was inputted by the user.
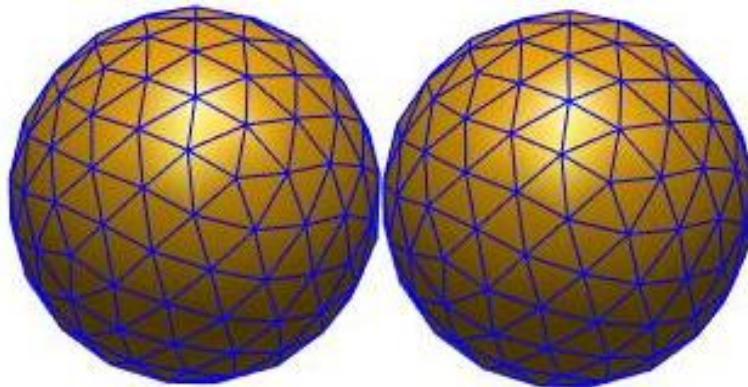
Figure 6.3: Image of two gold spheres created by the MNPBEM toolbox

6.4 Results and Discussion

6.4.1 LSPR for a Single Gold Sphere

Beginning with a straightforward simulation of a single nanosphere, the dielectric functions for gold and water were input into the MNPBEM code. To investigate the effect that size has on the plasmonic resonance, a total of twelve simulations were run as the diameter of the sphere was increased from 5 nm to 115 nm, in 10 nm increments (see Appendix D, Figures 6.8-6.19 and Table 6.1). Figure 6.4 contains all of the resonance wavelengths plotted against the gold nanoparticle diameter, in units of nanometers. As stated previously, Figure 6.4 illustrates that the plasmonic resonance for a Au nanosphere begins around 530 nm and will begin to redshift as the size is altered. An exponential line of best fit was added with an R^2 value of 0.9786, which indicates that the data fits an exponential trend quite well.
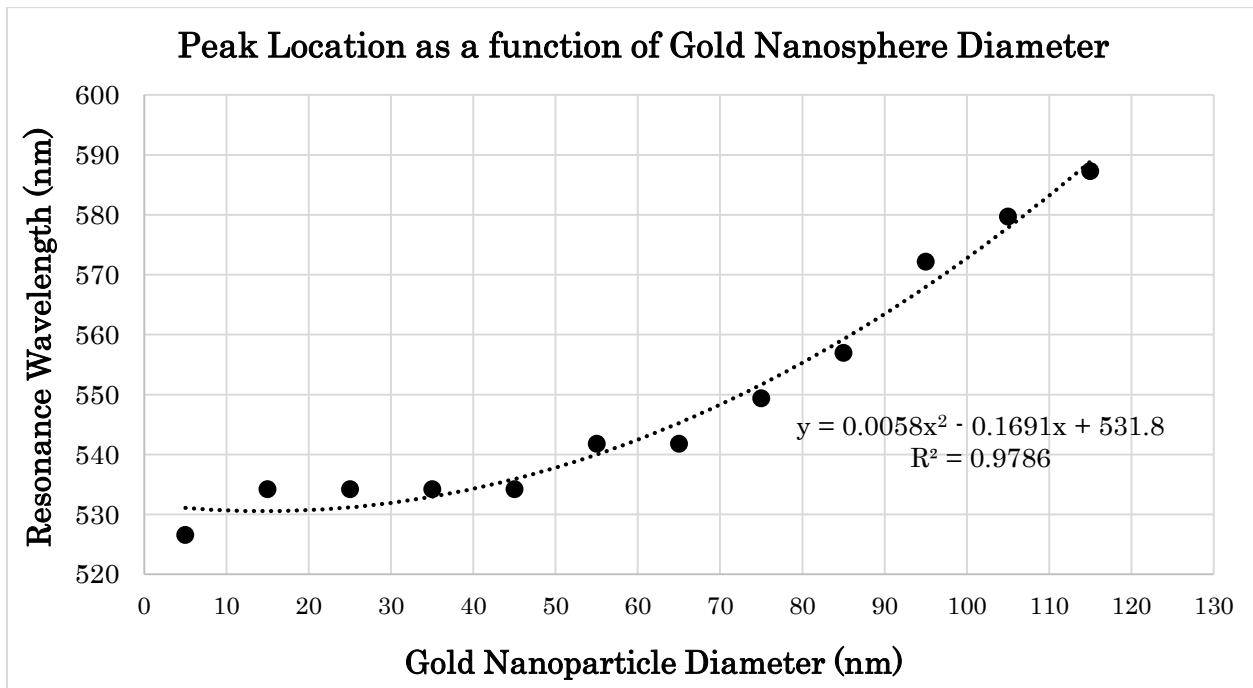

Figure 6.4: LSPR data obtained from the MNPBEM toolbox for a gold nanosphere with a diameter ranging from 5 nm to 115 nm, in 10 nm increments.

6.4.2 Modelling of Two Side By Side Gold Spheres

Two Au nanospheres with diameters of 65 nm were embedded in water to investigate the impact that sphere spacing has on the LSPR. Starting with a spacing distance of 0.01 nm, the spheres were eventually pulled apart to a distance of 150 nm. It was proposed that when another sphere is introduced into the embedding medium the original sphere should be able to "feel" the newly added sphere and the interaction be evident in the plasmonic resonance data. Figure 6.5 displays spectra for two different spacing distances of 0.01 nm and 0.1nm. Unlike the single sphere case, two resonance peaks are present at the very small distances. Since the two spheres are so close together they can be viewed as a single elongated structure and the two peaks are likely a result of the transverse and longitudinal oscillation of electrons. As outlined in Figure 6.1, transverse oscillations occur along the diameter of the nanoparticle and longitudinal oscillations occur along the length. The transverse resonance peak is located at a lower wavelength/higher energy because the positive and negative regions created during oscillation are much closer together and take more energy to separate.
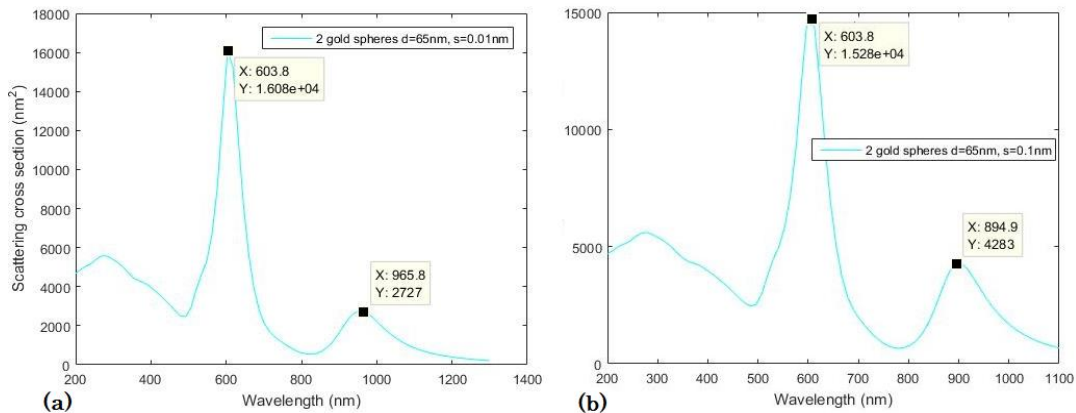
Figure 6.5: Transverse and longitudinal peaks for two gold spheres embedded in water with spacing distances of (a) 0.01 nm, and (b) 0.1 nm.

Since the diameters of the two spheres remain at 65 nm, the transverse peak is unaffected. Figure 6.6 contains the longitudinal resonance peak locations for 25 different spacing distances for the two Au spheres. For reference, the resonance wavelength of 541.8 nm for a single Au sphere with a diameter of 65 nm was added into Figure 6.6 as well. At very close spacing, the two spheres are acting like a rod and displaying two separate peaks. As you pull the two spheres apart, the two peaks merge into one as eventually it gets to a point where the two spheres do not feel the effects of one another anymore. This is the point where the two lines in Figure 6.6 meet. This data suggests that for a spacing distance of 70 nm and greater, the spheres are two independent structures and the spectra displays only a single resonance wavelength at approximately 541.8 nm (see Appendix D, Figures 6.20-6.42).
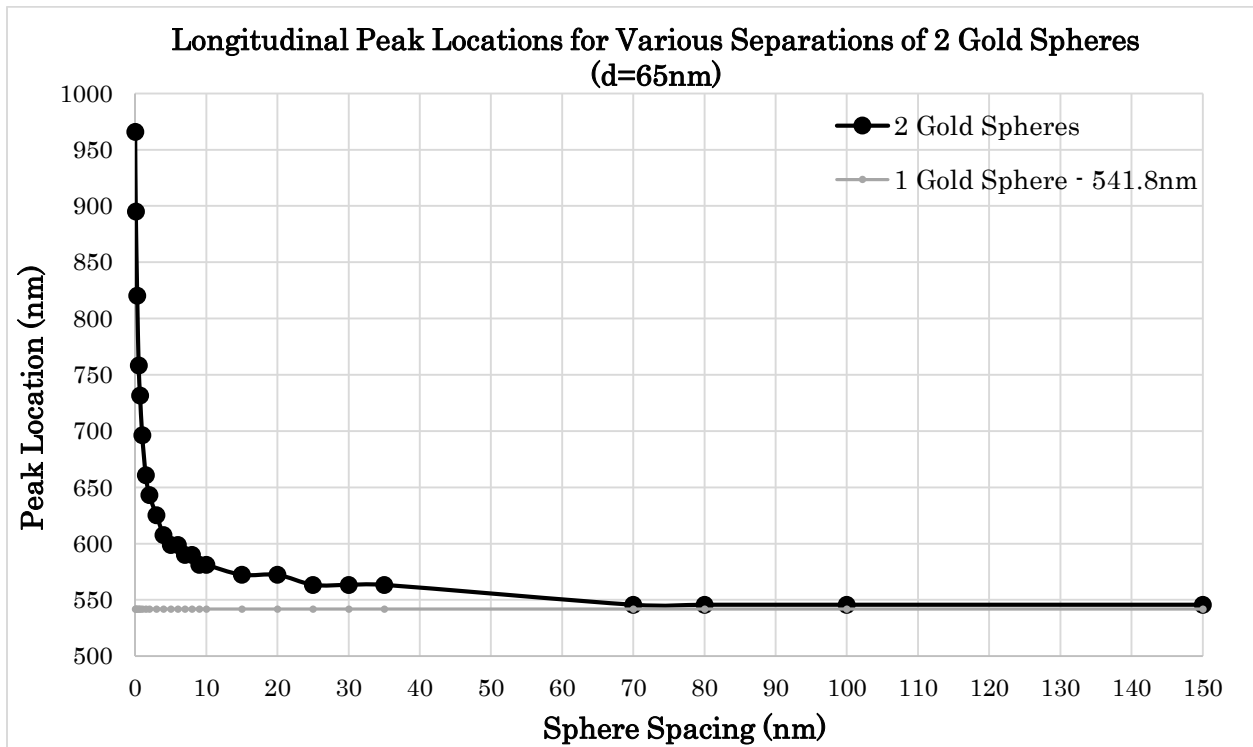
Figure 6.6: Longitudinal peak locations for two spheres as a function of the distance between them (●), and the peak location for a single sphere with a diameter of 65 nm (grey line).

6.4.3 Modelling of Three Gold Spheres in a Row

Three Au spheres were placed side by side in water at equal distances apart to investigate the LSPR for a rod-like structure. Separated by 0.1 nm, the diameters of the three Au spheres were increased from 35nm to 75 nm, in 5 nm increments (see Appendix D, Figures 6.43-6.51). It was expected that there be two resonance peaks present in the spectra for the longitudinal and transverse oscillations, and that the longitudinal wavelength red-shift more rapidly than the transverse one. Since each sphere was increased by 5nm, the entire length of the elongated structure was increased by 15 nm, while the width increased by only 5 nm. It was also expected that the longitudinal peak be present at a larger wavelength than the transverse one. Figure 6.7 contains the peak locations for both the transverse and longitudinal oscillations. Linear lines of best fit were added for each resonance peak and based on the slopes it can be said with certainty that the longitudinal resonance peak is in fact red-shifting at a larger wavelength more rapidly than the transverse one.
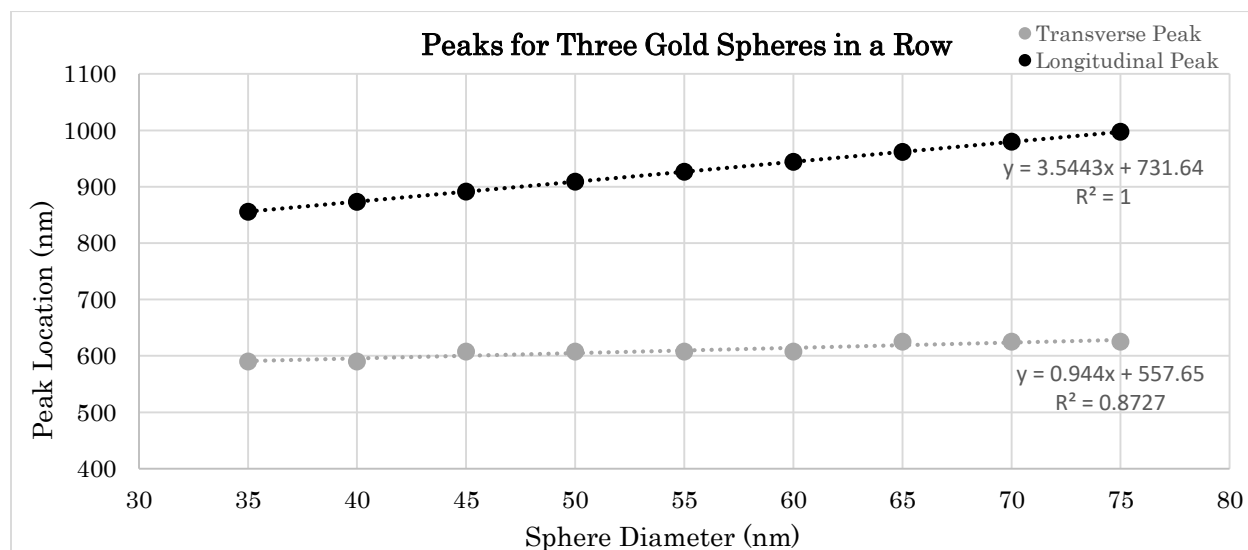
Figure 6.7: Transverse (grey) and longitudinal (black) peak location for three gold spheres in a row, with spacing distances of 0.1 nm.

6.5 Conclusions

In conclusion, this side project on plasmonics is considered a success as the MNPBEM toolbox was used to accurately simulate LSPR for single Au spheres and multiple Au spheres in a row. For the single Au sphere, the results coincided with previously published data[114] since for the smallest diameter the plasmonic resonance was around 530 nm. Furthermore, as the diameter was increased, the wavelength for the resonance red-shifted because the positive and negative regions created during oscillation were becoming farther apart. For the cases of the two spheres and three spheres placed side by side, it was noted there were two resonance peaks present in the spectra. This was due to the fact that the spheres were aligned creating a rod-like figure. As mentioned in Figure 6.1, rods display one resonance peak for the longitudinal oscillation of electrons and one for the transverse oscillation of electrons. Future work for this project could involve the simulation of different sized rods made from various metals. As the shapes to be studied become more complex, the coding involved does so as well and therefore some time may have to be spent learning the language used within the MNPBEM toolbox.

Supplementary information for Chapter 2: Fundamental Structure of CdSe Crystal Lattice

| $Cd_{59}Se_{50}^{+18} + 18C_2H_3O_2^- \rightarrow Cd_{59}Se_{50}Ac_{18}$	
Structure	**Energy (eV)**
$Cd_{59}Se_{50}^{+18}$	-86 518
$C_2H_3O_2^-$ or (Ac^-)	-1 232
$Cd_{59}Se_{50}Ac_{18}$	-109 002

Table 2.1: Structural energy values (eV) at 0 K for the bare $Cd_{59}Se_{50}^{+18}$ QD, an acetate ion, and the capped $Cd_{59}Se_{50}Ac_{18}$ QD.
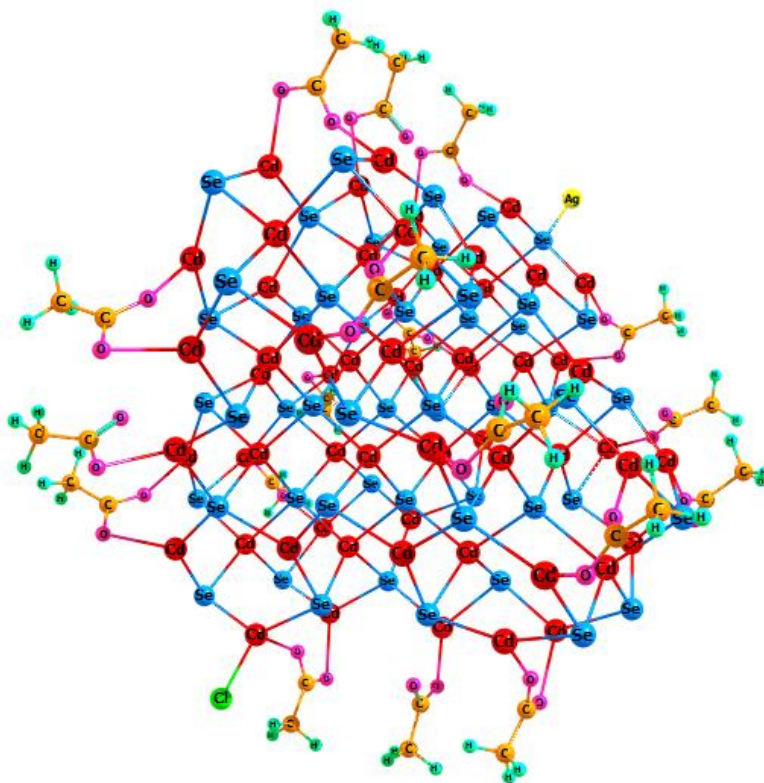
Scheme 2.3: Minimum energy structure of $Cd_{59}AgSe_{50}Ac_{18}Cl$ at 0 K, Ag^+ in surface location.
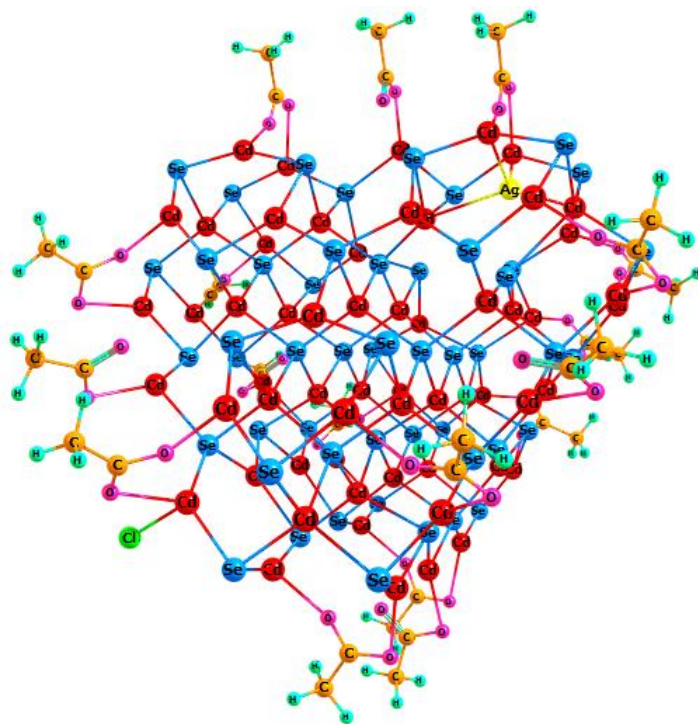
Scheme 2.4: Minimum energy structure of $Cd_{59}AgSe_{50}Ac_{18}Cl$ at 0 K, Ag^+ in midway lattice location.
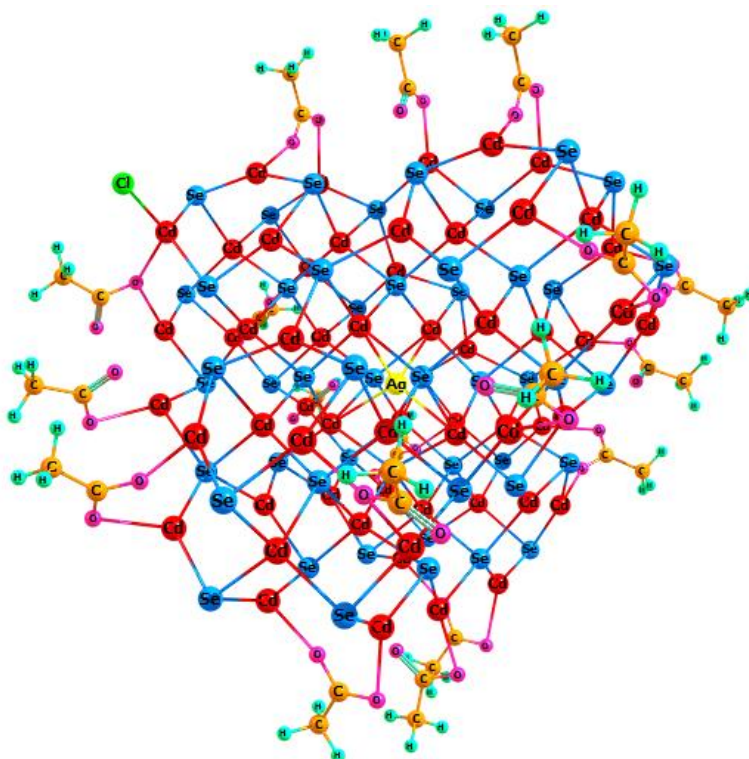
Scheme 2.5: Minimum energy structure of $Cd_{59}AgSe_{50}Ac_{18}Cl$ at 0 K, Ag^+ in core lattice location.

Cd$_{59}$Se$_{50}$Ac$_{18}$ + AgCl → Cd$_{59}$AgSe$_{50}$Ac$_{18}$Cl	
Structure	Energy (eV)
Cd$_{59}$Se$_{50}$Ac$_{18}$	-109 002
AgCl	-1 414
Cd$_{59}$AgSe$_{50}$Ac$_{18}$Cl (surface site)	-110 418
Cd$_{59}$AgSe$_{50}$Ac$_{18}$Cl (midway site)	-110 417
Cd$_{59}$AgSe$_{50}$Ac$_{18}$Cl (core site)	-110 417

Table 2.2: Structural energy values (eV) at 0 K for interstitial doping of Cd$_{59}$Se$_{50}$Ac$_{18}$ QD with Ag$^+$ through the addition of AgCl.

Cd$_{59}$Se$_{50}$Ac$_{18}$ + AgCl → Cd$_{59}$AgSe$_{50}$Ac$_{18}$Cl	
Structure	Gap (eV)
Cd$_{59}$Se$_{50}$Ac$_{18}$	1.84
Cd$_{59}$AgSe$_{50}$Ac$_{18}$Cl (surface site)	1.61
Cd$_{59}$AgSe$_{50}$Ac$_{18}$Cl (midway site)	1.28
Cd$_{59}$AgSe$_{50}$Ac$_{18}$Cl (core site)	1.30

Table 2.3: HOMO-LUMO gap values (eV) at 0 K for undoped Cd$_{59}$Se$_{50}$Ac$_{18}$ QD and three interstitially doped Cd$_{59}$AgSe$_{50}$Ac$_{18}$Cl QD's.
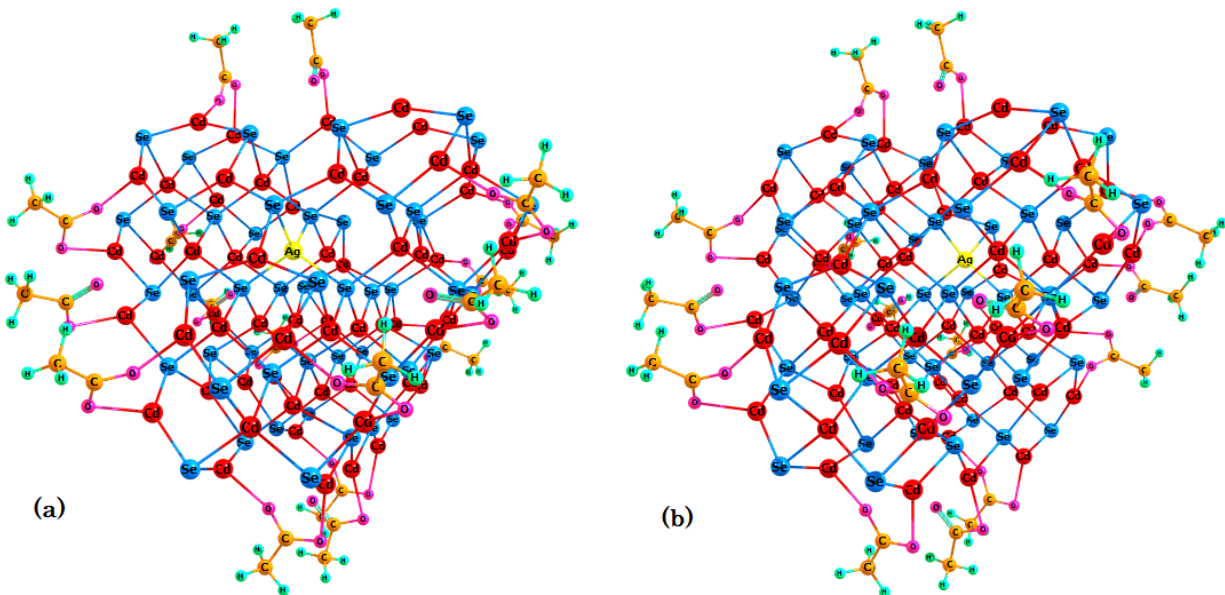
Scheme 2.6: Two minimum energy Cd$_{58}$AgSe$_{50}$Ac$_{17}$ structures at 0 K, where Ag$^+$ was substituted in at two different locations at the core of the lattice.
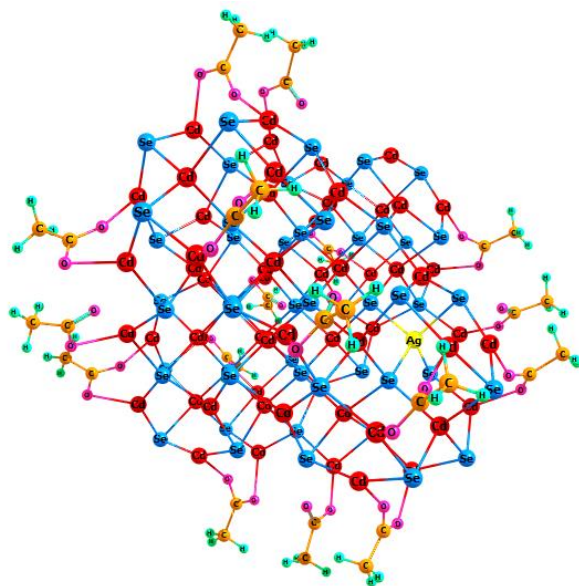
Scheme 2.7: Minimum energy $Cd_{58}AgSe_{50}Ac_{17}$ structure at 0 K, where Ag^+ was substituted in at a midway location in the lattice.
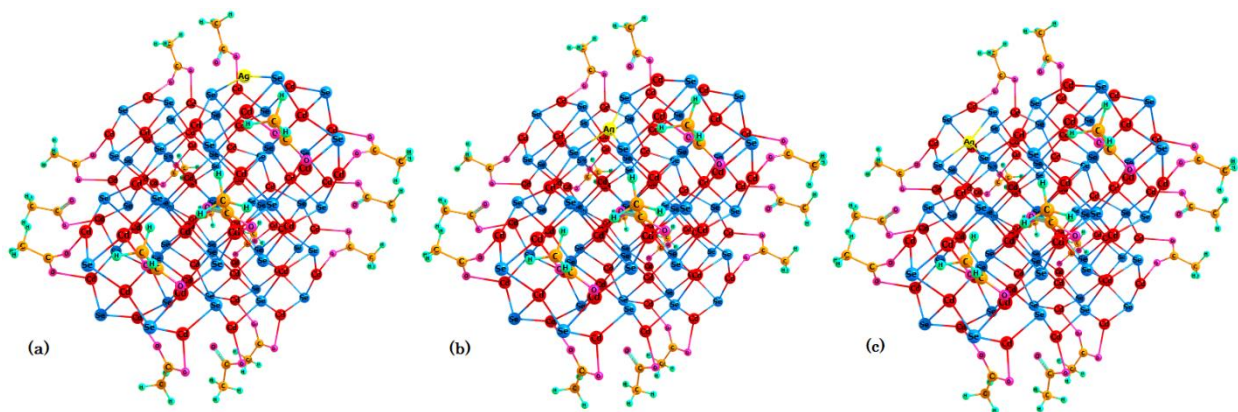
Scheme 2.8: Three minimum energy $Cd_{58}AgSe_{50}Ac_{17}$ structures at 0 K, where Ag^+ was substituted in at three different locations at the surface.

$Cd_{59}Se_{50}Ac_{18} + AgCl \rightarrow Cd_{58}AgSe_{50}Ac_{17} + Cd^{2+} + Ac^- + Cl^-$	
Structure	Energy (eV)
$Cd_{59}Se_{50}Ac_{18}$	-109 002
AgCl	-1 414
(a) $Cd_{58}AgSe_{50}Ac_{17}$ (core site)	-110 391
(b) $Cd_{58}AgSe_{50}Ac_{17}$ (core site)	-110 391
$Cd_{58}AgSe_{50}Ac_{17}$ (midway site)	-110 391
(a) $Cd_{58}AgSe_{50}Ac_{17}$ (surface site)	-110 392
(b) $Cd_{58}AgSe_{50}Ac_{17}$ (surface site)	-110 391
(c) $Cd_{58}AgSe_{50}Ac_{17}$ (surface site)	-110 391
Cd^{2+}	-1 227
Ac^-	-1 232
Cl^-	-409

Table 2.4: Structural energy values (eV) at 0 K for substitutional doping of $Cd_{59}Se_{50}Ac_{18}$ QD with Ag^+ through the addition of AgCl.

$Cd_{59}Se_{50}Ac_{18} + AgCl \rightarrow Cd_{58}AgSe_{50}Ac_{17} + Cd^{2+} + Ac^- + Cl^-$	
Structure	Gap (eV)
$Cd_{59}Se_{50}Ac_{18}$	1.84
(a) $Cd_{58}AgSe_{50}Ac_{17}$ (core site)	1.55
(b) $Cd_{58}AgSe_{50}Ac_{17}$ (core site)	1.37
$Cd_{58}AgSe_{50}Ac_{17}$ (midway site)	1.15
(a) $Cd_{58}AgSe_{50}Ac_{17}$ (surface site)	1.84
(b) $Cd_{58}AgSe_{50}Ac_{17}$ (surface site)	1.67
(c) $Cd_{58}AgSe_{50}Ac_{17}$ (surface site)	1.36

Table 2.5: HOMO-LUMO gap values (eV) at 0 K for undoped $Cd_{59}Se_{50}Ac_{18}$ QD and six substitutionally doped $Cd_{58}AgSe_{50}Ac_{17}$ QD's.

$Cd_{59}Se_{50}Ac_{18}$ + AgCl → $Cd_{59}AgSe_{50}Ac_{18}Cl$	
Product	Formation Energy, ΔE (eV)
$Cd_{59}AgSe_{50}Ac_{18}Cl$ (surface site)	-1.89
$Cd_{59}AgSe_{50}Ac_{18}Cl$ (midway site)	-1.18
$Cd_{59}AgSe_{50}Ac_{18}Cl$ (core site)	-1.20
$Cd_{59}Se_{50}Ac_{18}$ + AgCl → $Cd_{58}AgSe_{50}Ac_{17}$ + Cd^{2+} + Ac^- + Cl^-	
Product	Formation Energy, ΔE (eV)
(a) $Cd_{58}AgSe_{50}Ac_{17}$ (core site)	+25.30
(b) $Cd_{58}AgSe_{50}Ac_{17}$ (core site)	+25.46
$Cd_{58}AgSe_{50}Ac_{17}$ (midway site)	+25.59
(a) $Cd_{58}AgSe_{50}Ac_{17}$ (surface site)	+24.58
(b) $Cd_{58}AgSe_{50}Ac_{17}$ (surface site)	+24.95
(c) $Cd_{58}AgSe_{50}Ac_{17}$ (surface site)	+25.23

Table 2.6: Formation energy values (eV) at 0 K for three interstitially doped $Cd_{59}AgSe_{50}Ac_{18}Cl$ QD's and six substitutionally doped $Cd_{58}AgSe_{50}Ac_{17}$ QD's.
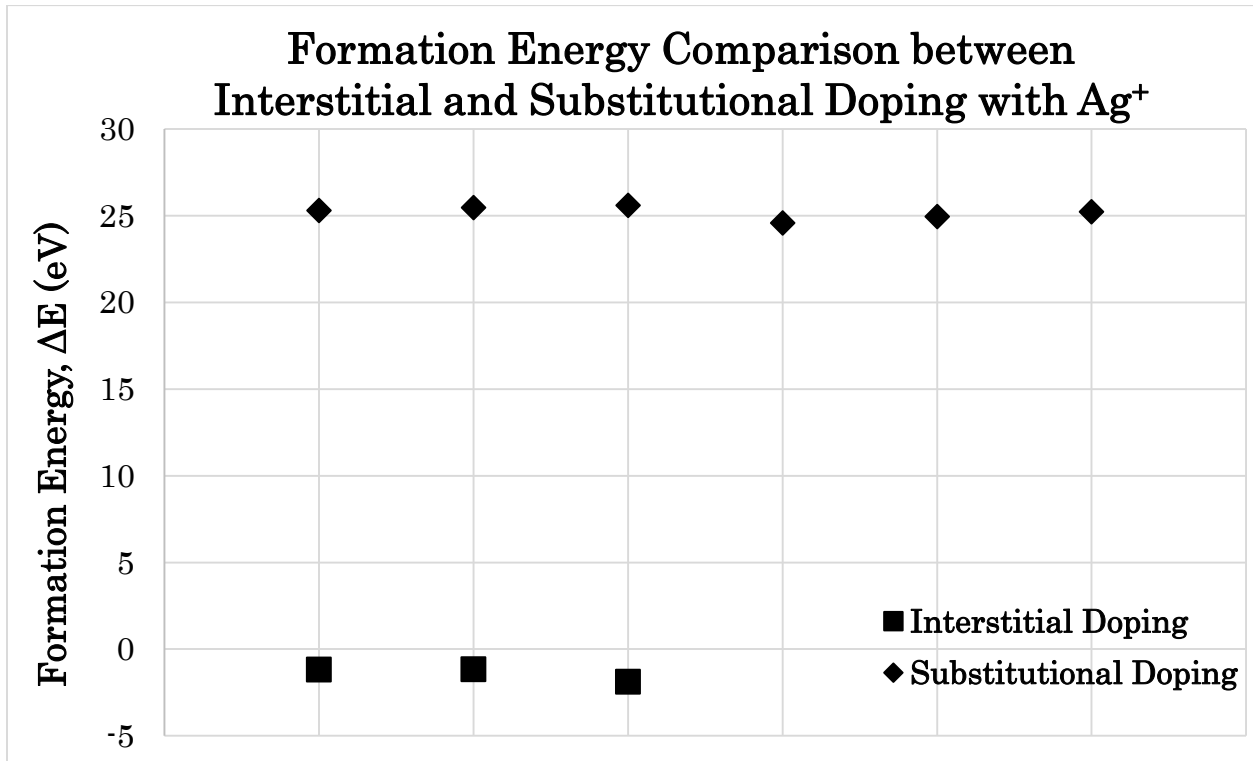
Figure 2.6: Formation energy, ΔE, values (eV) for three interstitial doping cases (■) and six substitutional doping cases (◆).

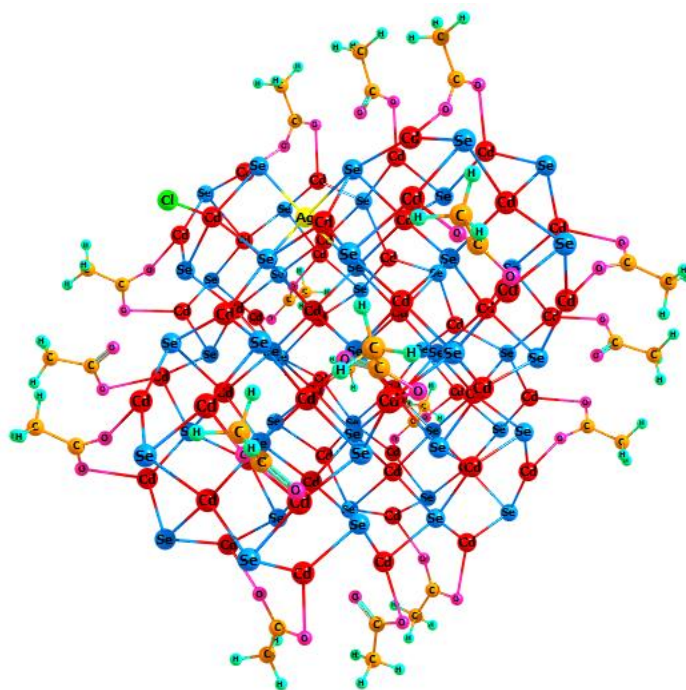*Supplementary information for Chapter 3: Influence of Ag-Cl Distance on the Doped CdSe Quantum Dot*
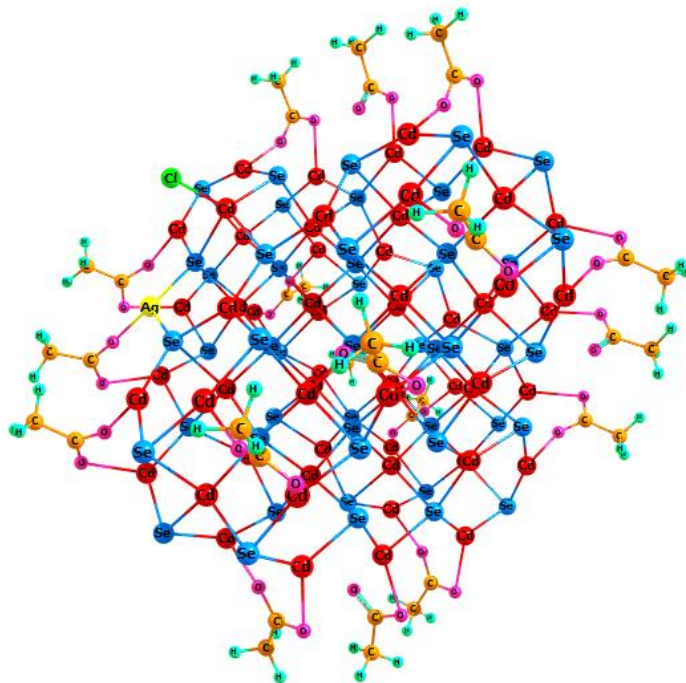
Scheme 3.1: Minimum energy $Cd_{59}AgSe_{50}Ac_{18}Cl$ structure at 0 K, Ag-Cl distance of 4.89 Å.
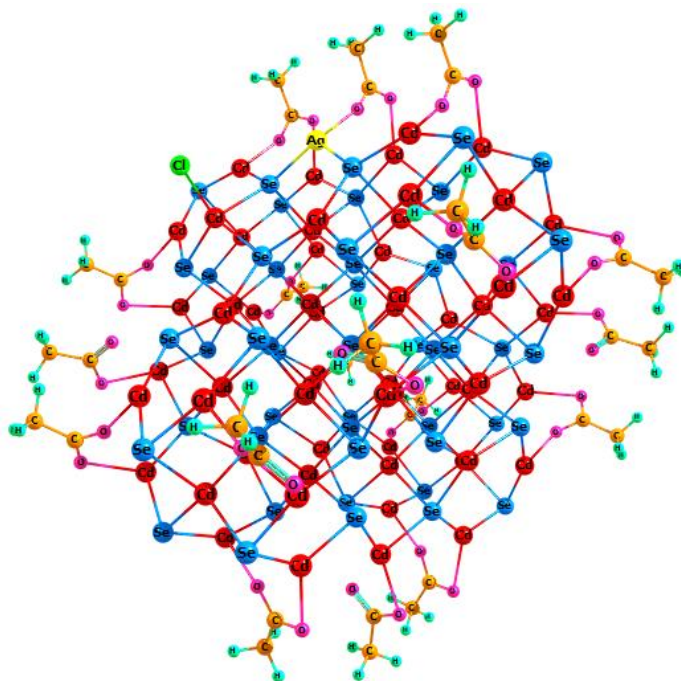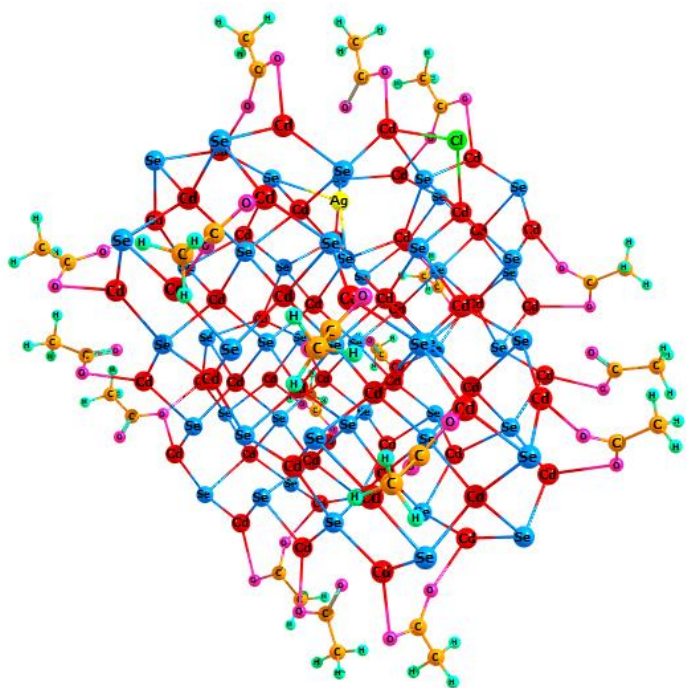

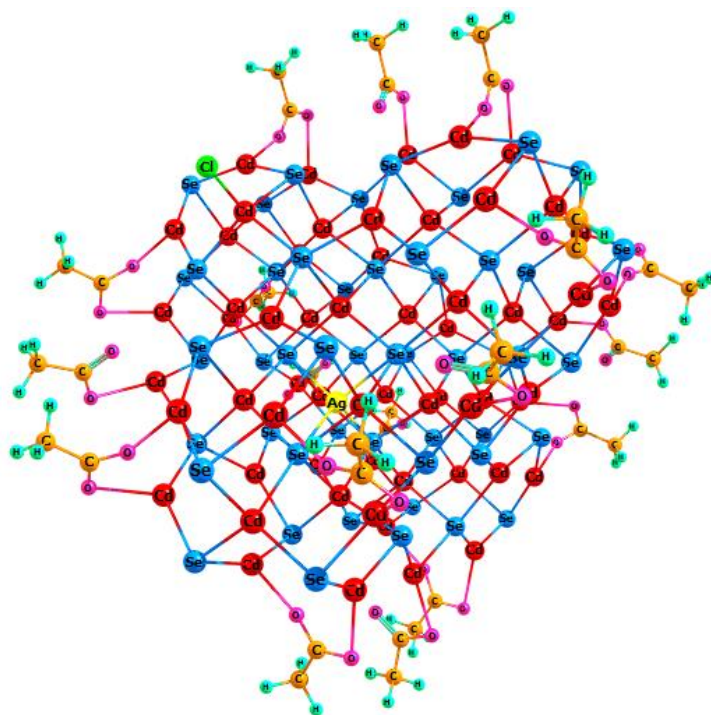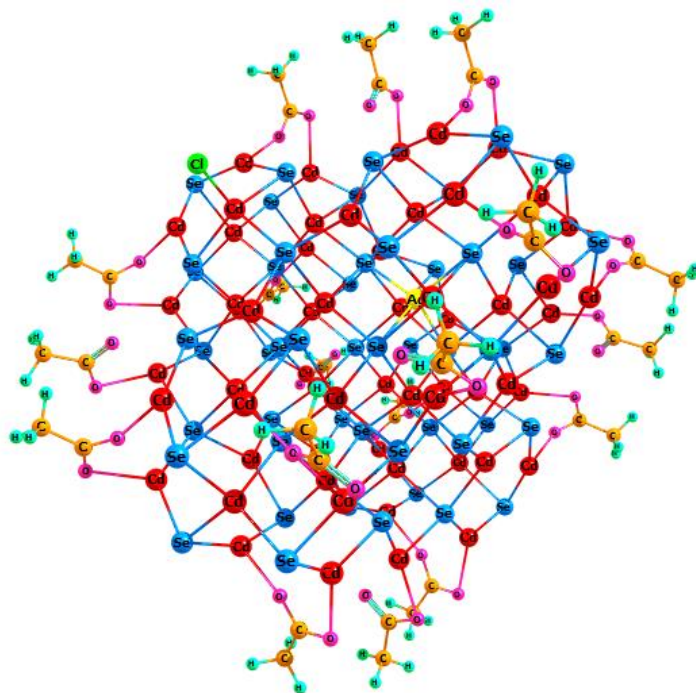Scheme 3.2: Minimum energy $Cd_{59}AgSe_{50}Ac_{18}Cl$ structure at 0 K, Ag-Cl distance of 5.21 Å.

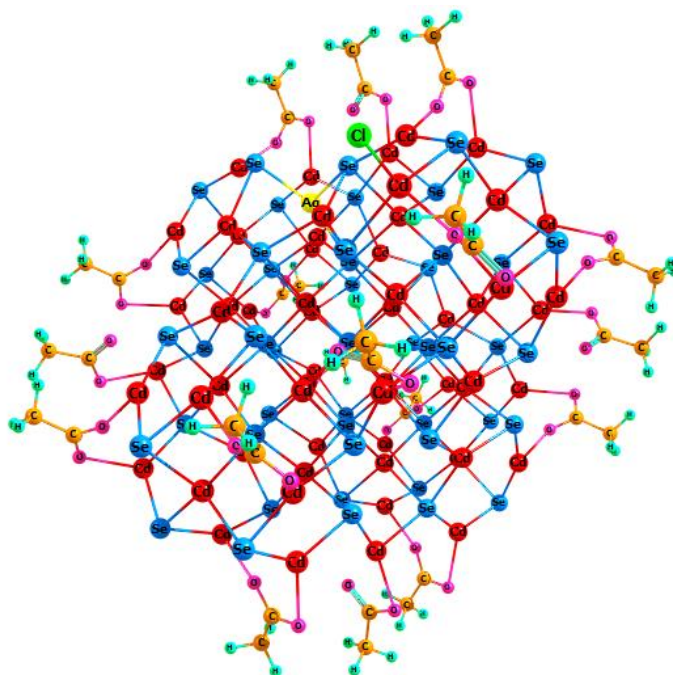Scheme 3.3: Minimum energy $Cd_{59}AgSe_{50}Ac_{18}Cl$ structure at 0 K, Ag-Cl distance of 5.44 Å.

Scheme 3.4: Minimum energy $Cd_{59}AgSe_{50}Ac_{18}Cl$ structure at 0 K, Ag-Cl distance of 6.40 Å.

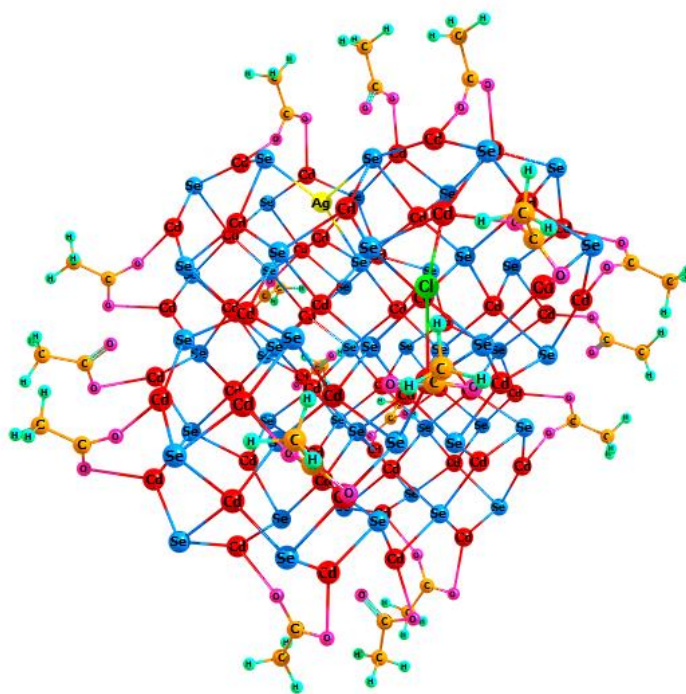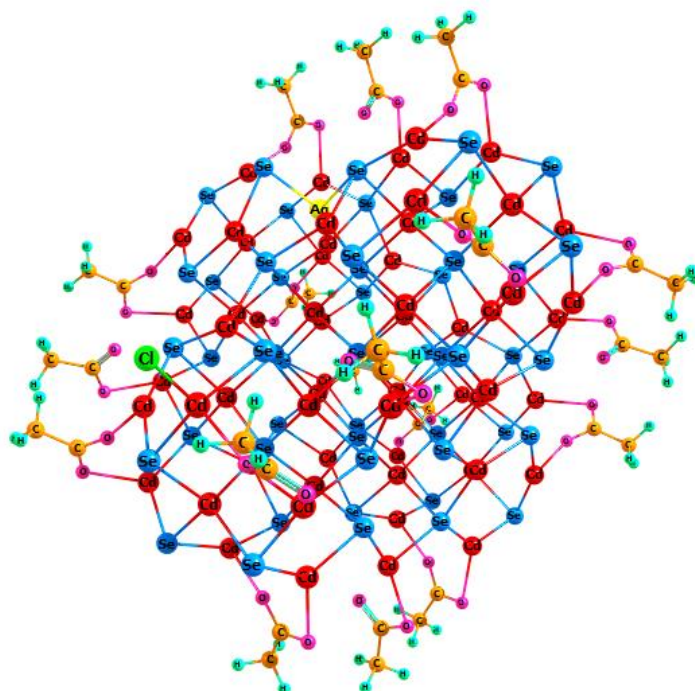Scheme 3.5: Minimum energy $Cd_{59}AgSe_{50}Ac_{18}Cl$ structure at 0 K, Ag-Cl distance of 8.81 Å.

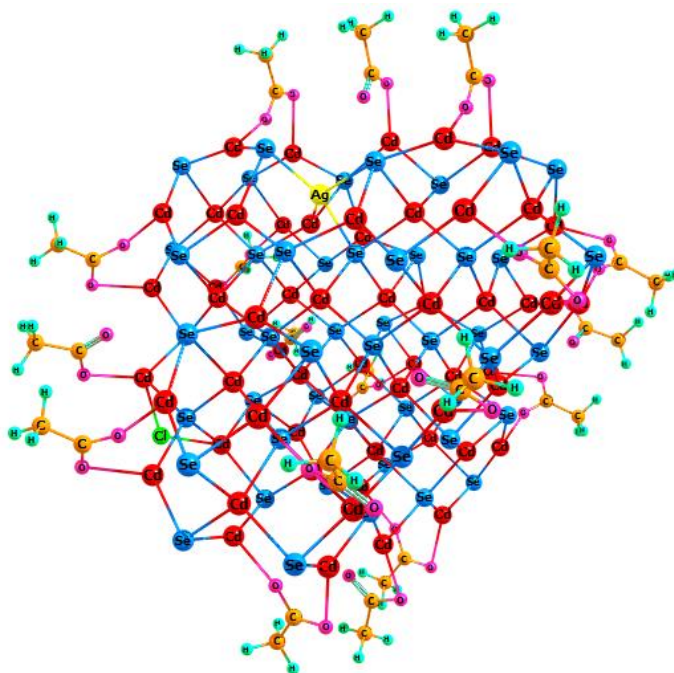Scheme 3.6: Minimum energy $Cd_{59}AgSe_{50}Ac_{18}Cl$ structure at 0 K, Ag-Cl distance of 8.88 Å.

Scheme 3.7: Minimum energy $Cd_{59}AgSe_{50}Ac_{18}Cl$ structure at 0 K, Ag-Cl distance of 8.96 Å.

Scheme 3.8: Minimum energy $Cd_{59}AgSe_{50}Ac_{18}Cl$ structure at 0 K, Ag-Cl distance of 8.97 Å.
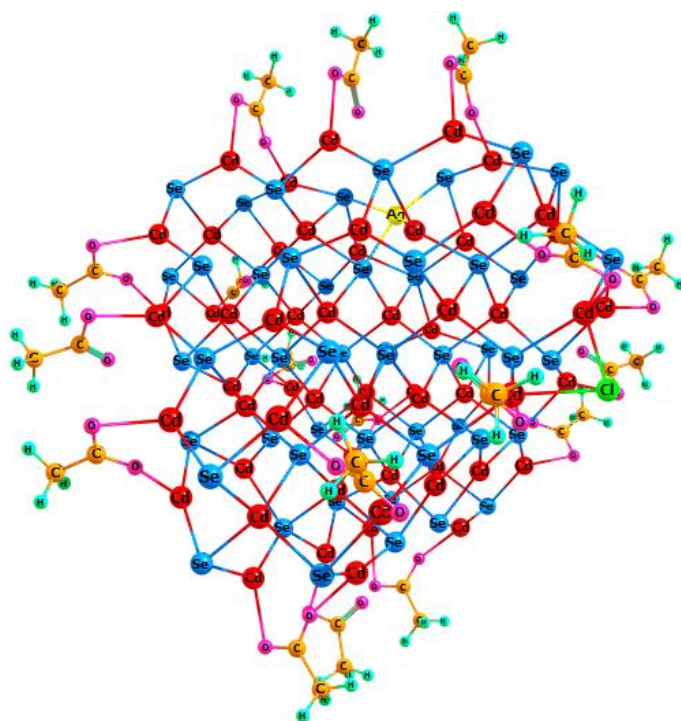
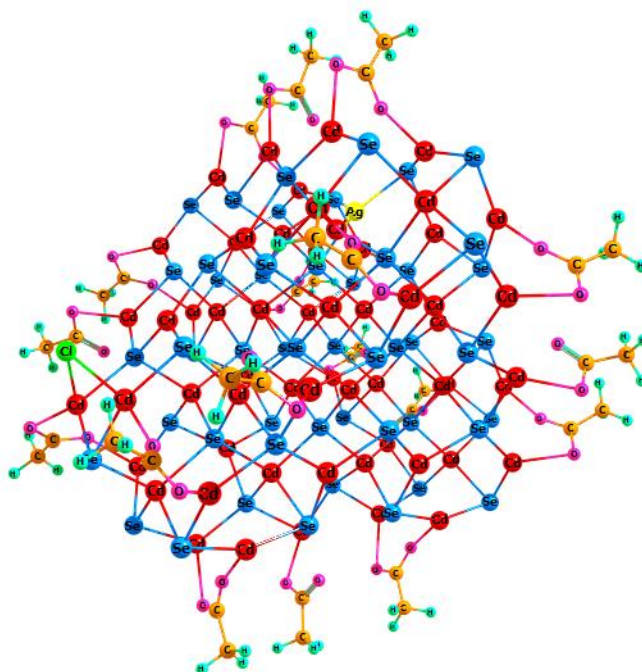Scheme 3.9: Minimum energy $Cd_{59}AgSe_{50}Ac_{18}Cl$ structure at 0 K, Ag-Cl distance of 11.12 Å.

Scheme 3.10: Minimum energy $Cd_{59}AgSe_{50}Ac_{18}Cl$ structure at 0 K, Ag-Cl distance of 11.43 Å.
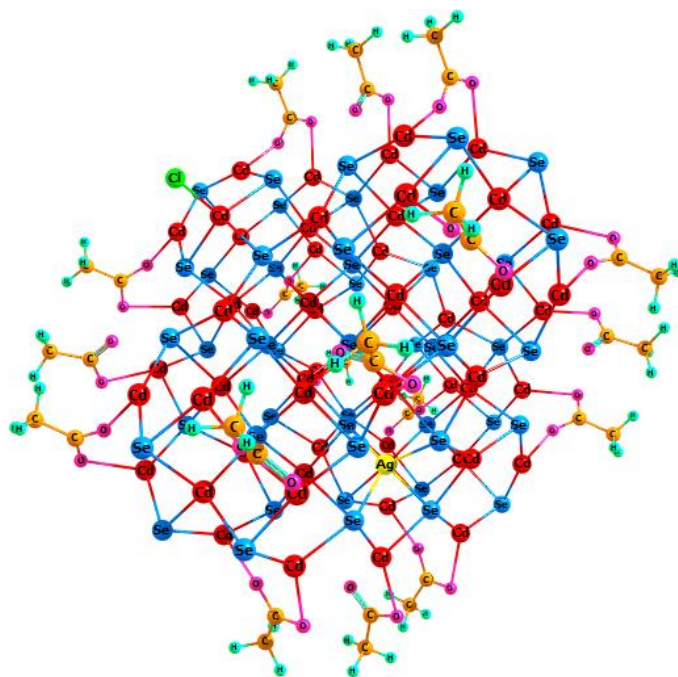
Scheme 3.11: Minimum energy $Cd_{59}AgSe_{50}Ac_{18}Cl$ structure at 0 K, Ag-Cl distance of 11.72 Å.

Scheme 3.12: Minimum energy $Cd_{59}AgSe_{50}Ac_{18}Cl$ structure at 0 K, Ag-Cl distance of 12.43 Å.

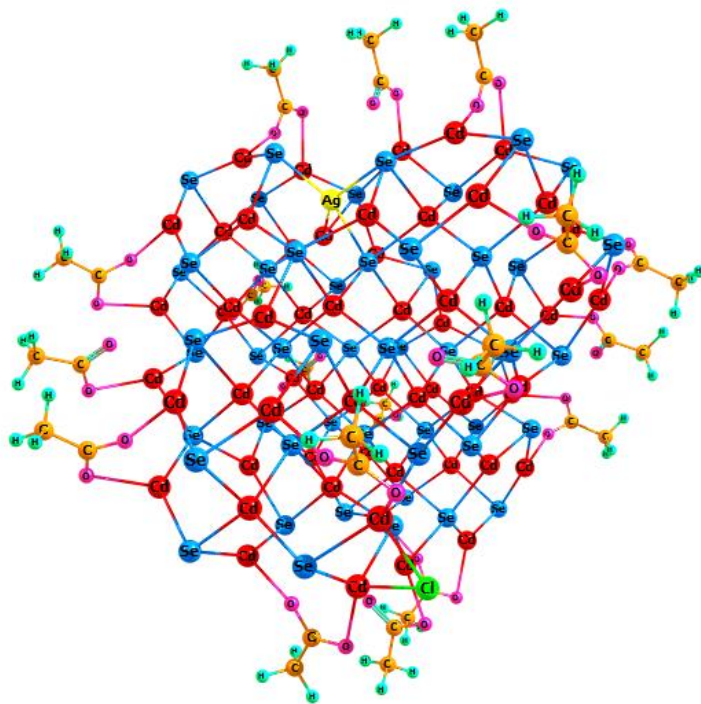Scheme 3.13: Minimum energy $Cd_{59}AgSe_{50}Ac_{18}Cl$ structure at 0 K, Ag-Cl distance of 12.58 Å.

Scheme 3.14: Minimum energy $Cd_{59}AgSe_{50}Ac_{18}Cl$ structure at 0 K, Ag-Cl distance of 13.99 Å.

Scheme 3.15: Minimum energy $Cd_{59}AgSe_{50}Ac_{18}Cl$ structure at 0 K, Ag-Cl distance of 14.35 Å.

Scheme 3.16: Minimum energy $Cd_{59}AgSe_{50}Ac_{18}Cl$ structure at 0 K, Ag-Cl distance of 15.48 Å.
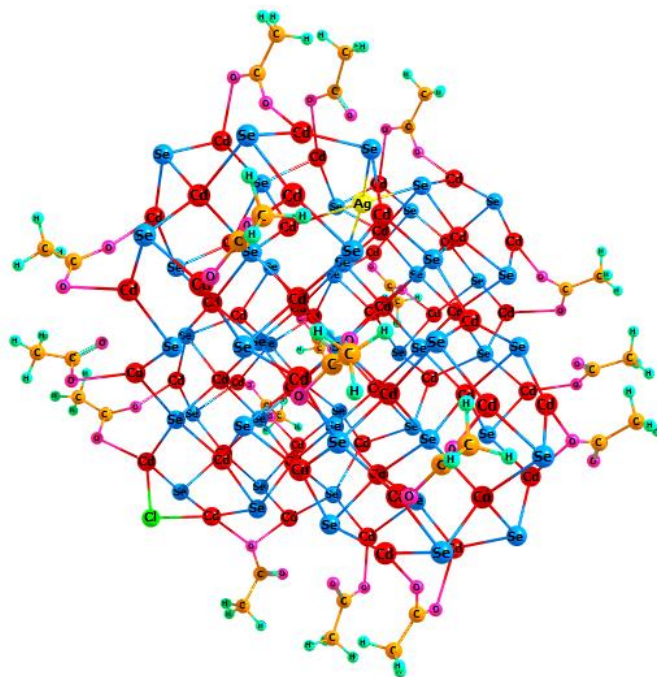
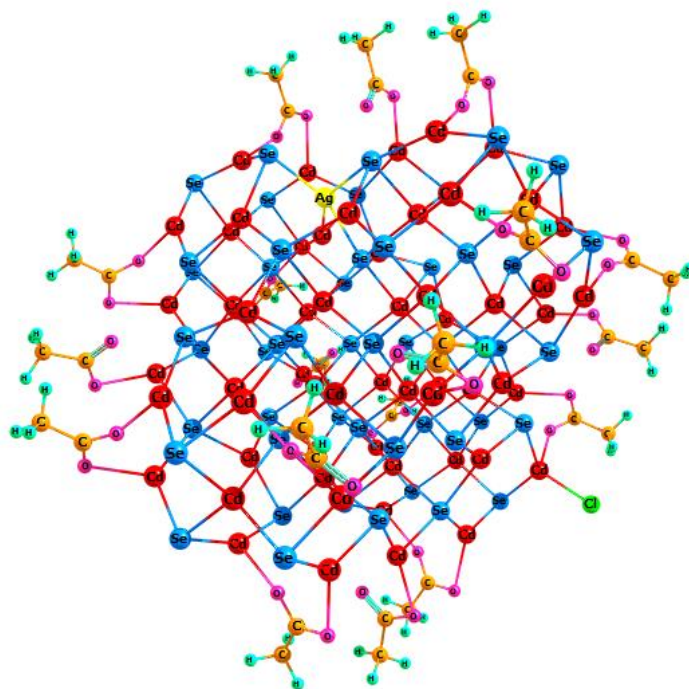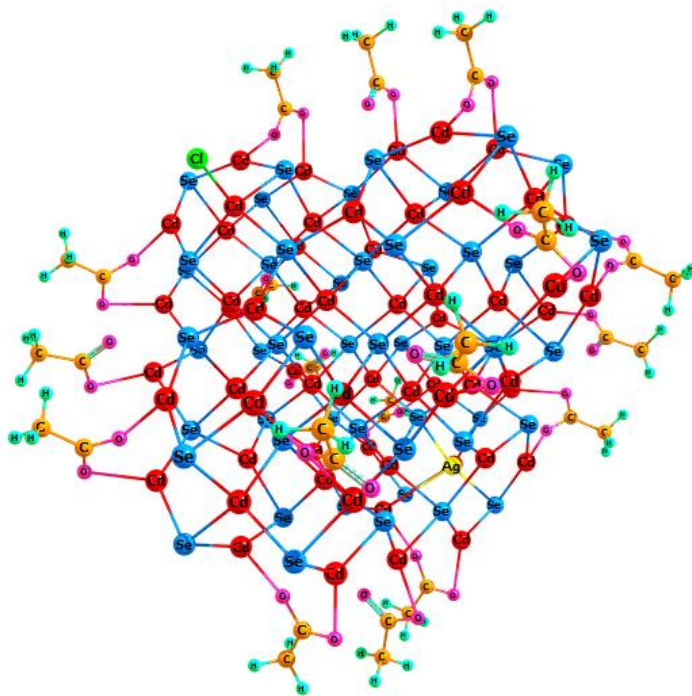Scheme 3.17: Minimum energy $Cd_{59}AgSe_{50}Ac_{18}Cl$ structure at 0 K, Ag-Cl distance of 16.19 Å.

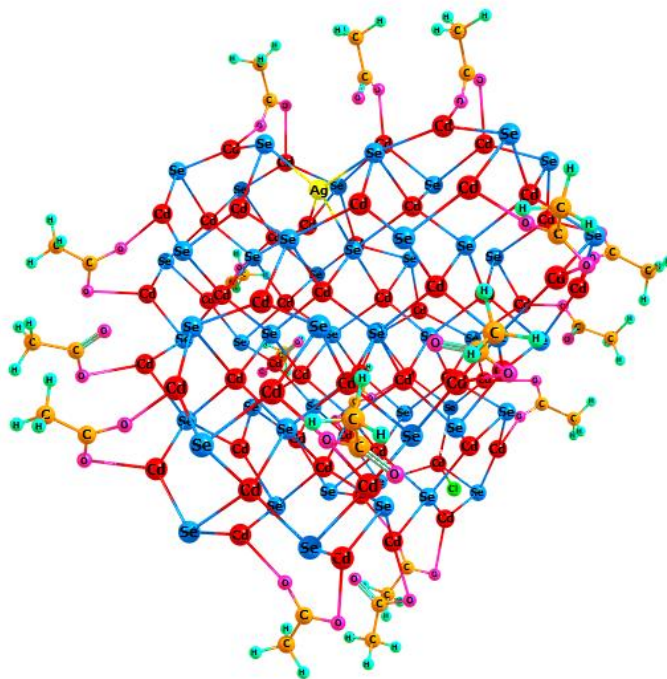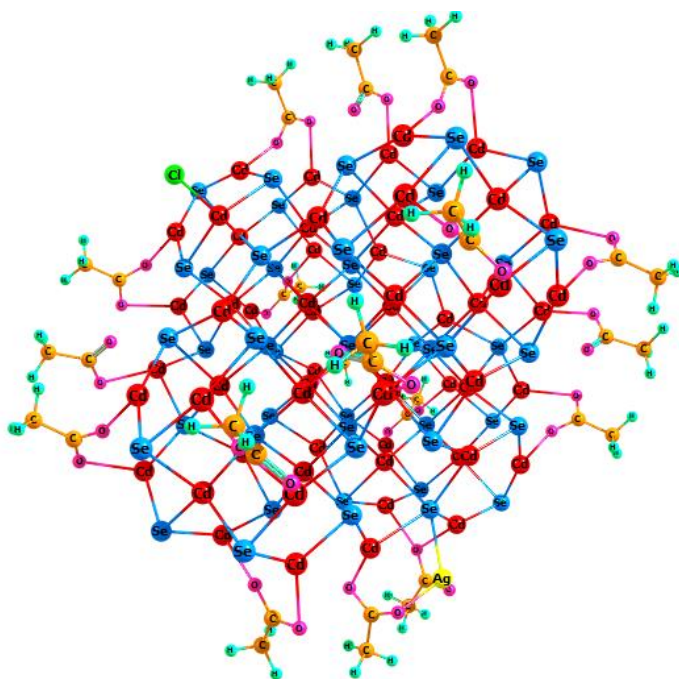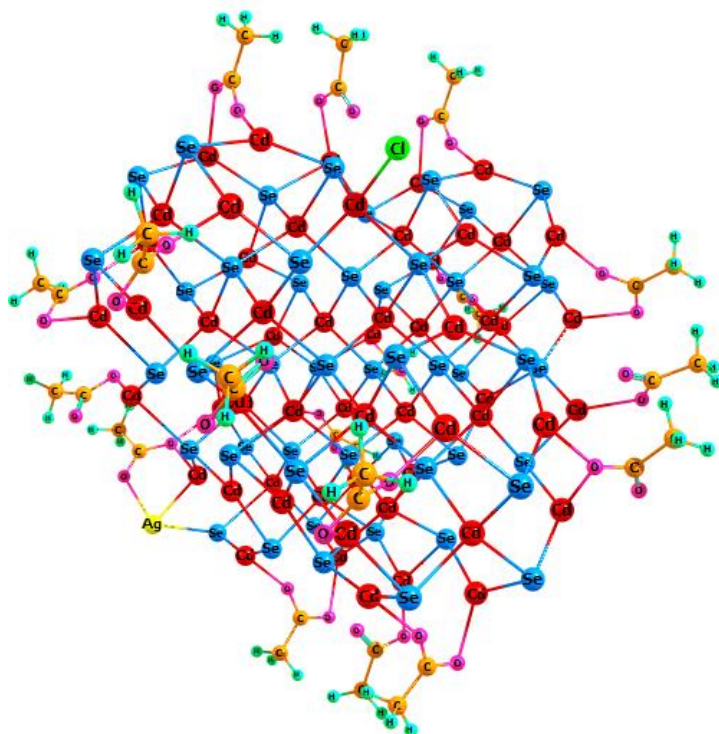
Scheme 3.18: Minimum energy $Cd_{59}AgSe_{50}Ac_{18}Cl$ structure at 0 K, Ag-Cl distance of 16.98 Å.

Scheme 3.19: Minimum energy $Cd_{59}AgSe_{50}Ac_{18}Cl$ structure at 0 K, Ag-Cl distance of 17.78 Å.

Scheme 3.20: Minimum energy $Cd_{59}AgSe_{50}Ac_{18}Cl$ structure at 0 K, Ag-Cl distance of 18.77 Å.

Structure	Ag-Cl Distance (Å)	Formation Energy (eV)	HOMO-LUMO Gap (eV)
1	4.89	-1.70	1.78
2	5.21	-1.69	1.76
3	5.44	-1.19	1.69
4	6.40	-1.02	1.56
5	8.81	-1.30	1.51
6	8.88	-1.28	1.50
7	8.96	-1.29	1.41
8	8.97	-0.24	1.23
9	11.12	-1.08	1.22
10	11.43	-0.77	1.14
11	11.72	-0.50	1.10
12	12.43	-1.17	1.60
13	12.58	-0.99	1.38
14	13.99	-0.79	1.04
15	14.35	-1.17	1.50
16	15.48	-1.09	1.11
17	16.19	-0.75	1.12
18	16.98	-0.52	1.20
19	17.78	-0.47	1.14
20	18.77	-0.09	1.08

Table 3.1 Ag-Cl distances (Å), formation energy (eV) values, and HOMO-LUMO gap (eV) values for twenty interstitially doped $Cd_{59}AgSe_{50}Ac_{18}Cl$ QD's.

Appendix C

Supplementary information for Chapter 4: Temperature Impacts on the Doped CdSe Quantum Dot
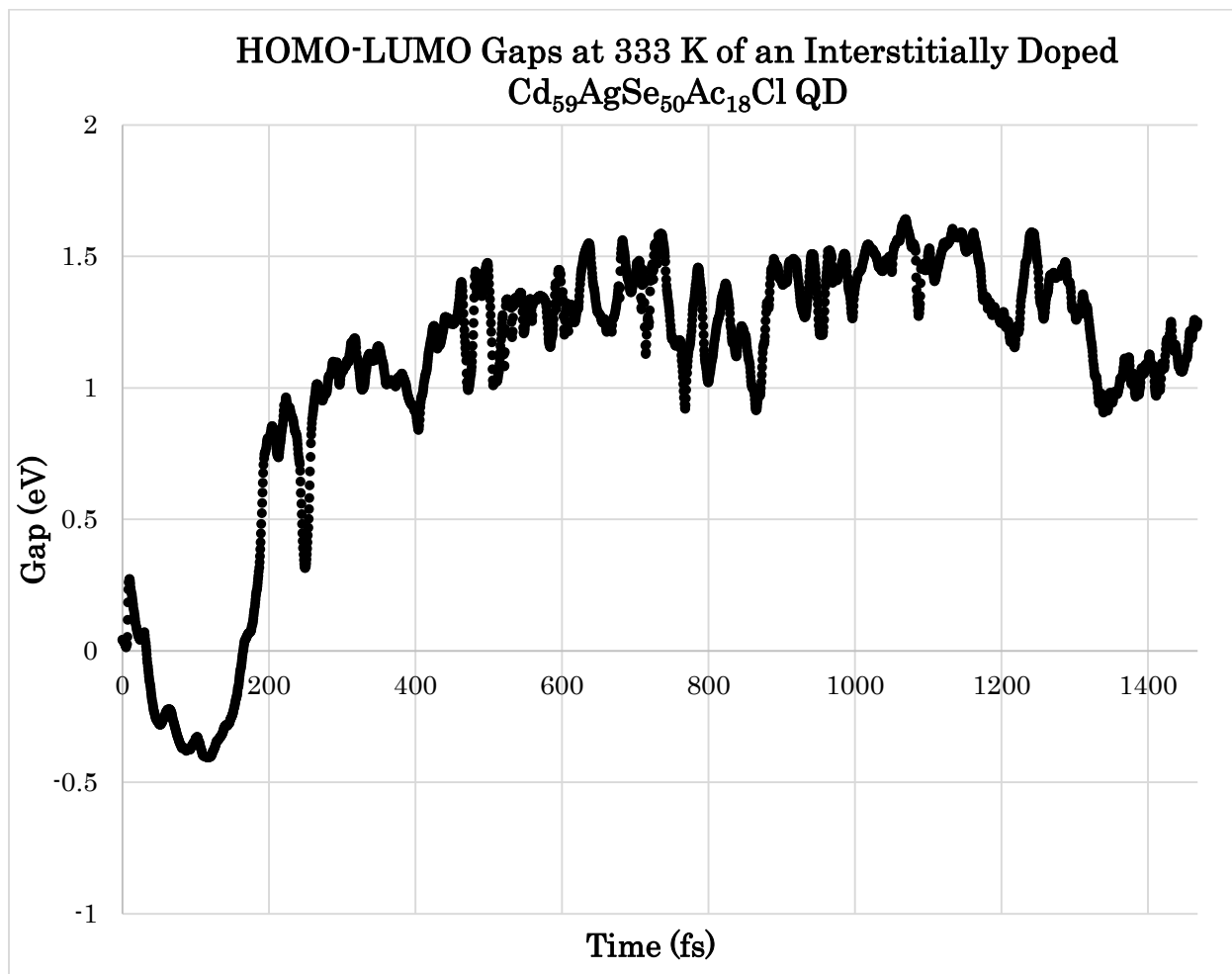

Figure 4.5: HOMO-LUMO gap values (eV) as a function of time (fs) at 333 K for an interstitially doped $Cd_{59}AgSe_{50}Ac_{18}Cl$ QD.
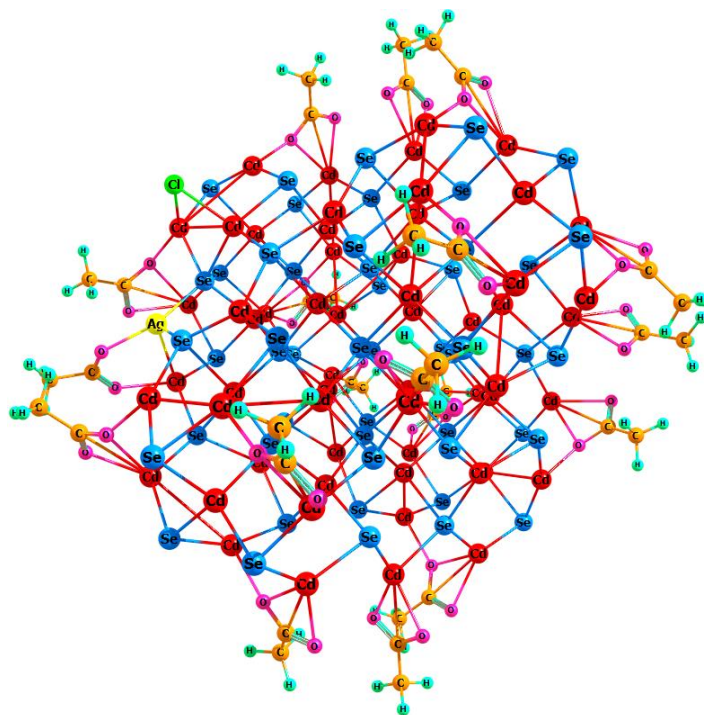
Scheme 4.1: Structure 1 - $Cd_{59}AgSe_{50}Ac_{18}Cl$ structure at 333 K, Ag-Cl distance of 4.94 Å at 333 K and 9000 fs.
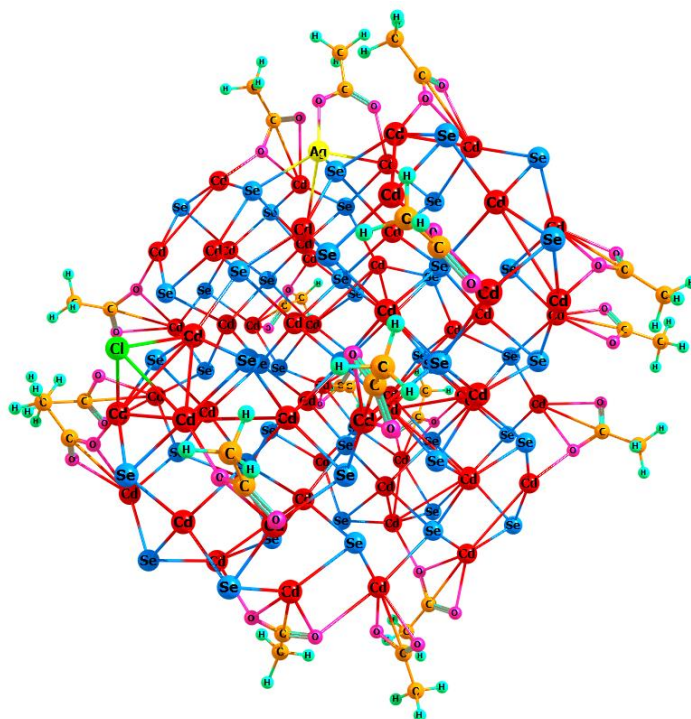
Scheme 4.2: Structure 2 - $Cd_{59}AgSe_{50}Ac_{18}Cl$ structure at 333 K, Ag-Cl distance of 10.68 Å at 333 K and 9000 fs.
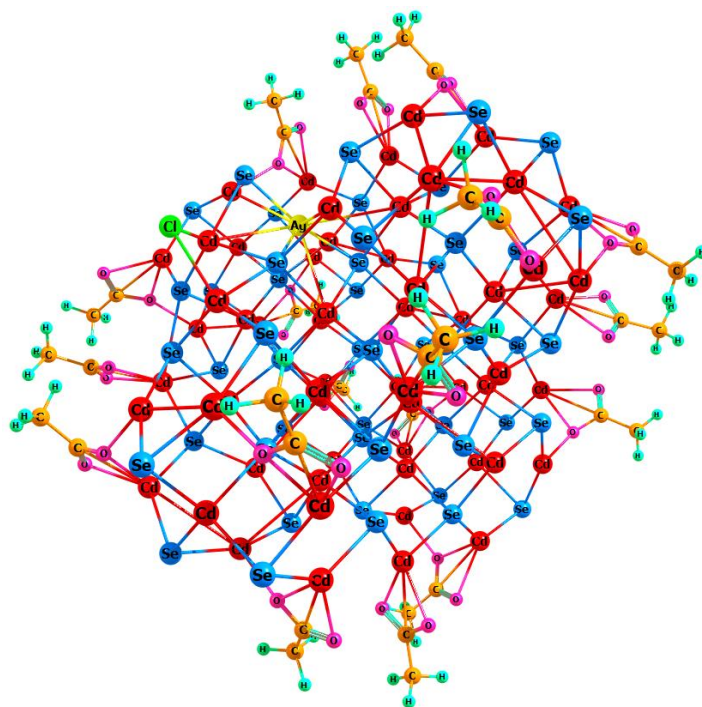
Scheme 4.3: Structure 3 - $Cd_{59}AgSe_{50}Ac_{18}Cl$ structure at 333 K, Ag-Cl distance of 5.31 Å at 333 K and 9000 fs.
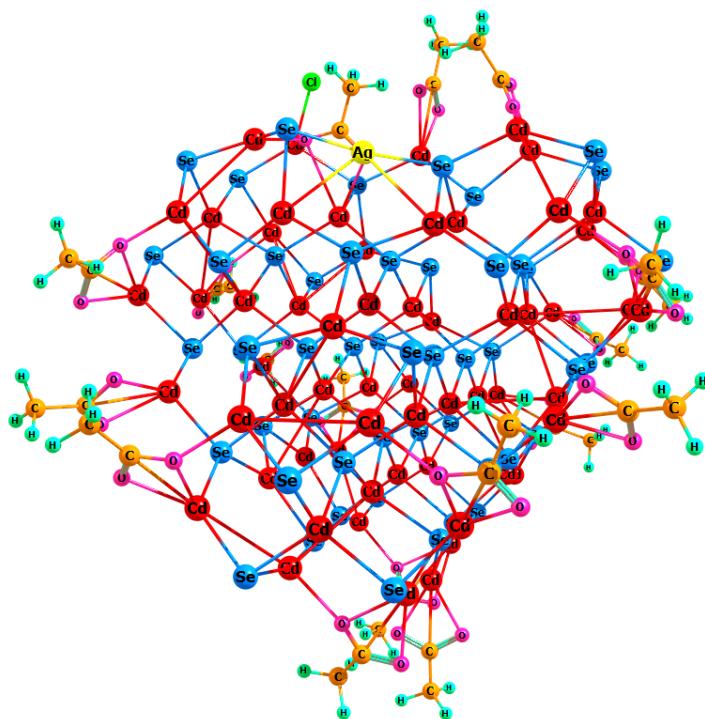
Scheme 4.4: Structure 4 - $Cd_{59}AgSe_{50}Ac_{18}Cl$ structure at 333 K, Ag-Cl distance of 7.09 Å at 333 K and 9000 fs.
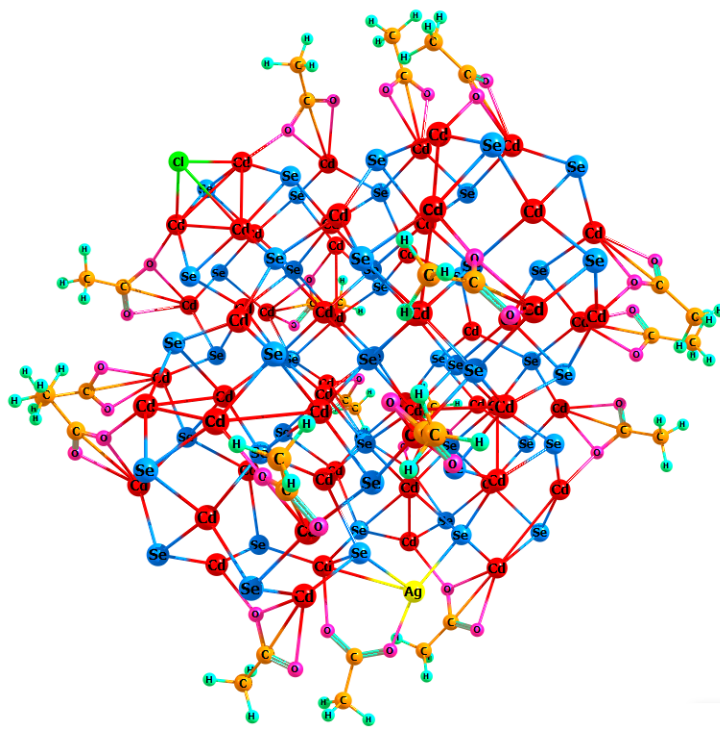
Scheme 4.5: Structure 5 - Cd$_{59}$AgSe$_{50}$Ac$_{18}$Cl structure at 333 K, Ag-Cl distance of 16.76 Å at 333 K and 9000 fs.
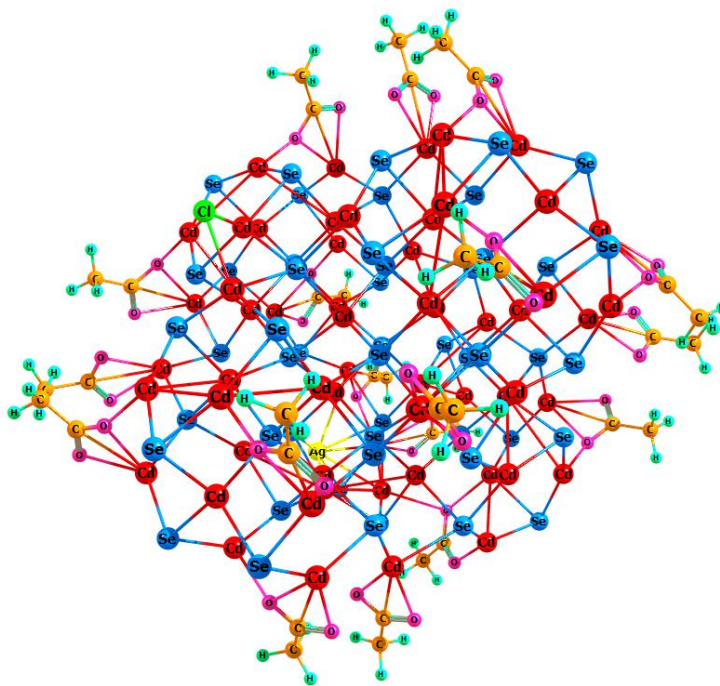
Scheme 4.6: Structure 6 - Cd$_{59}$AgSe$_{50}$Ac$_{18}$Cl structure at 333 K, Ag-Cl distance of 13.20 Å at 333 K and 9000 fs.
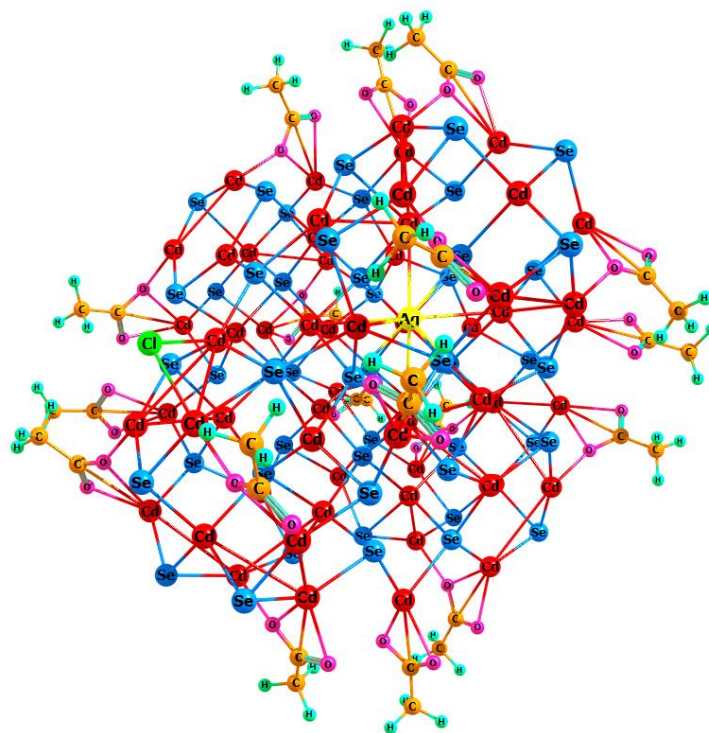
Scheme 4.7: Structure 7 - $Cd_{59}AgSe_{50}Ac_{18}Cl$ structure at 333 K, Ag-Cl distance of 8.21 Å at 333 K and 9000 fs.
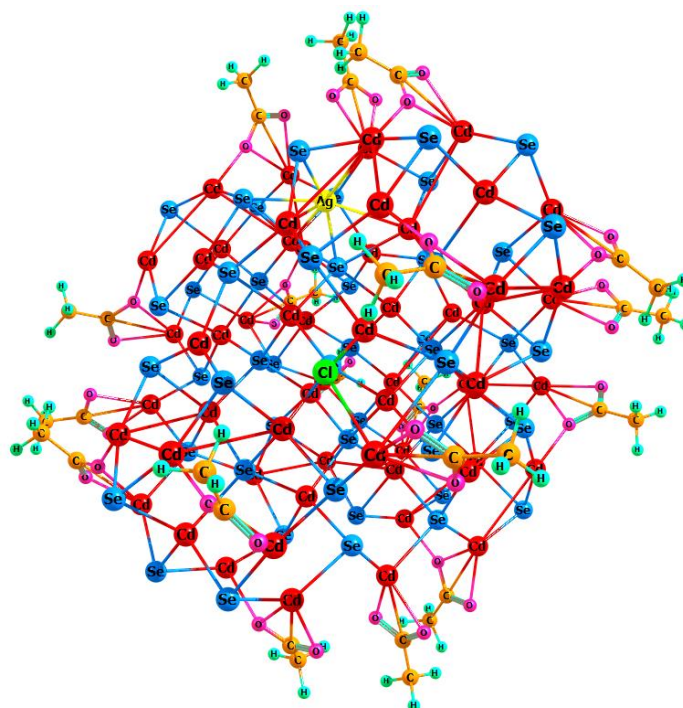
Scheme 4.8: Structure 8 - $Cd_{59}AgSe_{50}Ac_{18}Cl$ structure at 333 K, Ag-Cl distance of 8.52 Å at 333 K and 9000 fs.
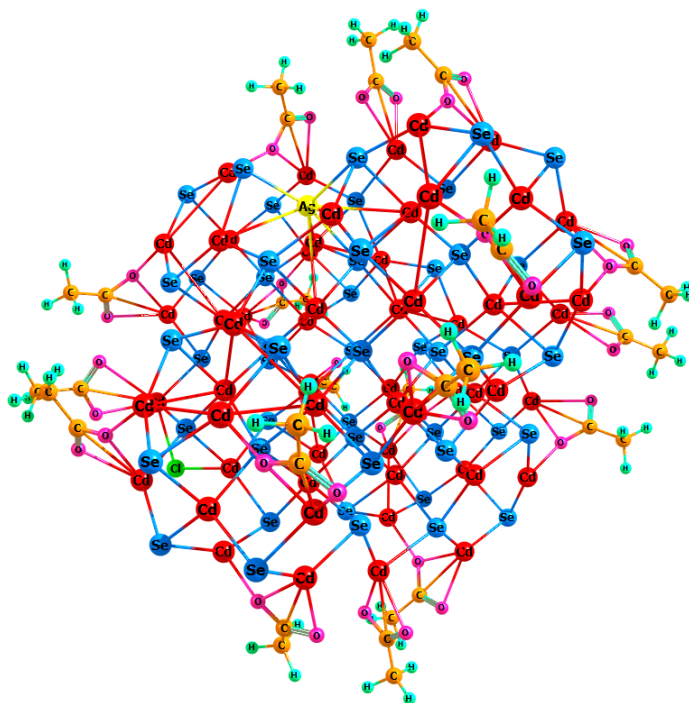
Scheme 4.9: Structure 9 - Cd$_{59}$AgSe$_{50}$Ac$_{18}$Cl structure at 333 K, Ag-Cl distance of 11.43 Å at 333 K and 9000 fs.
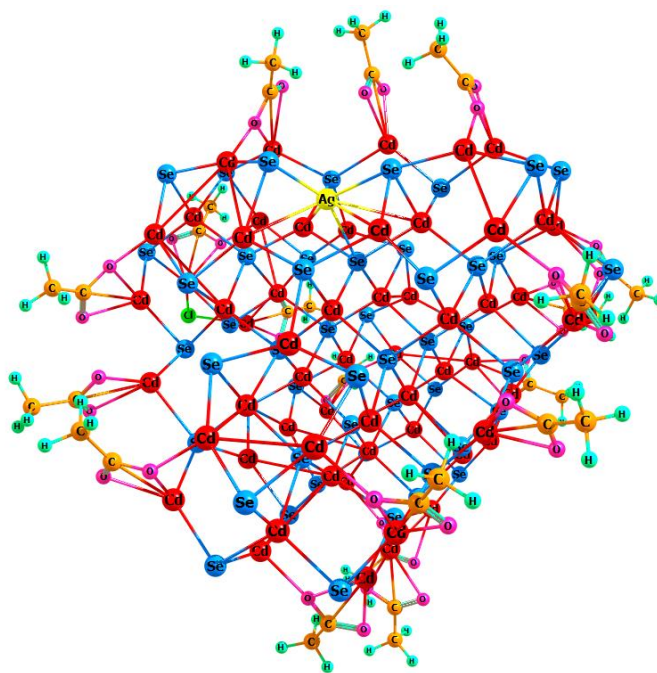
Scheme 4.10: Structure 10 - Cd$_{59}$AgSe$_{50}$Ac$_{18}$Cl structure at 333 K, Ag-Cl distance of 11.97 Å at 333 K and 9000 fs.

Appendix D

Supplementary information for Chapter 6: Additional Side Projects
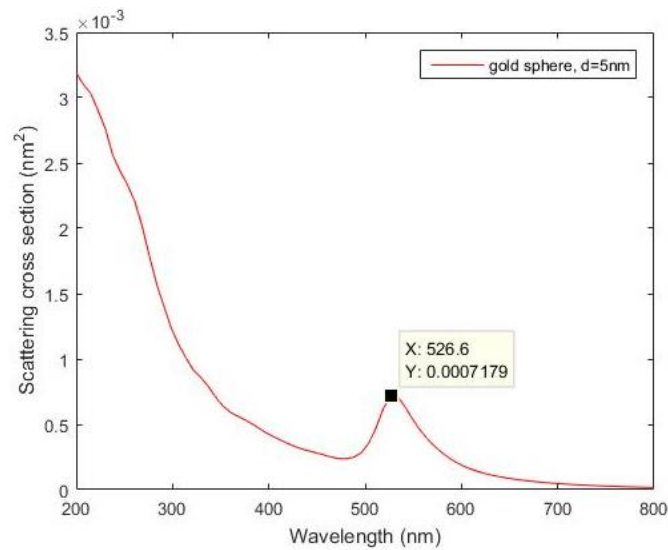
Figure 6.8: Scattering cross section plot for gold sphere, d=5 nm
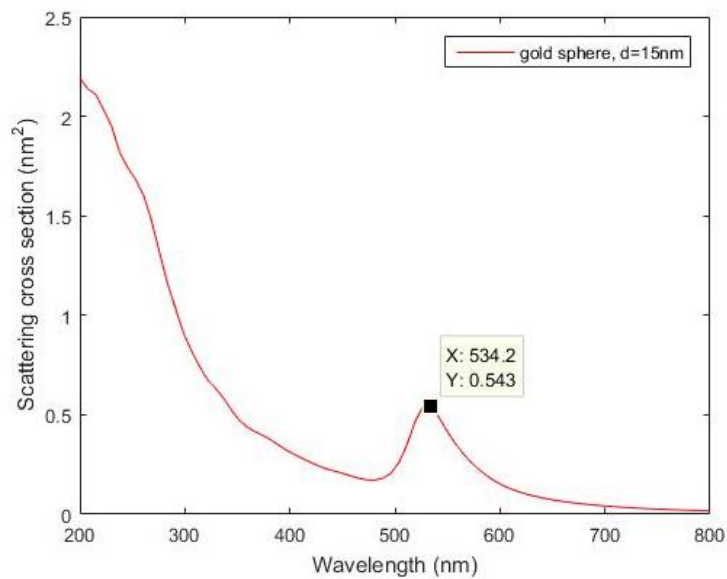
Figure 6.9: Scattering cross section plot for gold sphere, d=15 nm
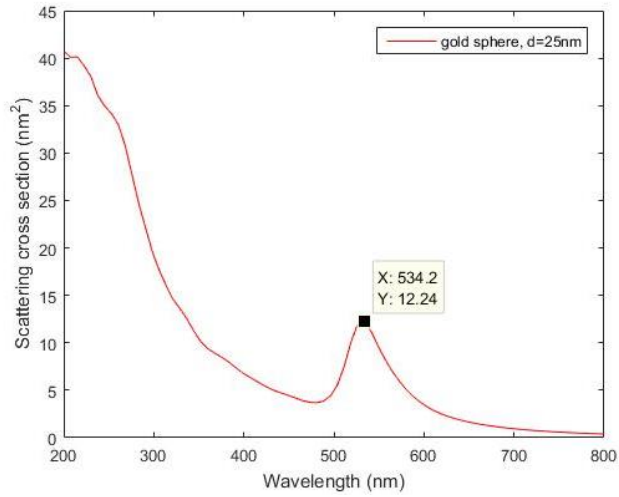
Figure 6.10: Scattering cross section plot for gold sphere, d=25 nm
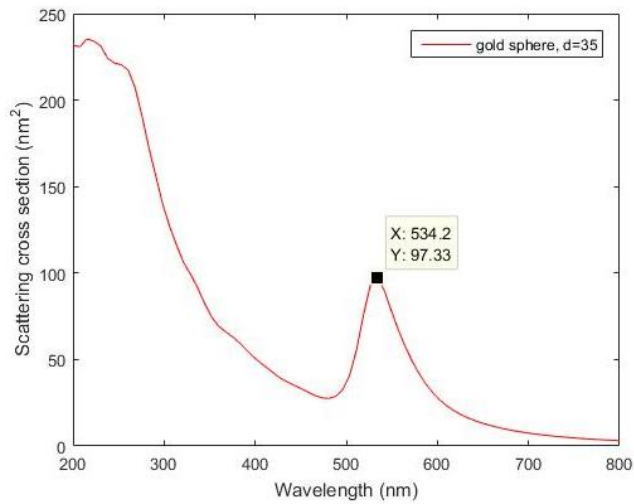
Figure 6.11: Scattering cross section plot for gold sphere, d=35 nm
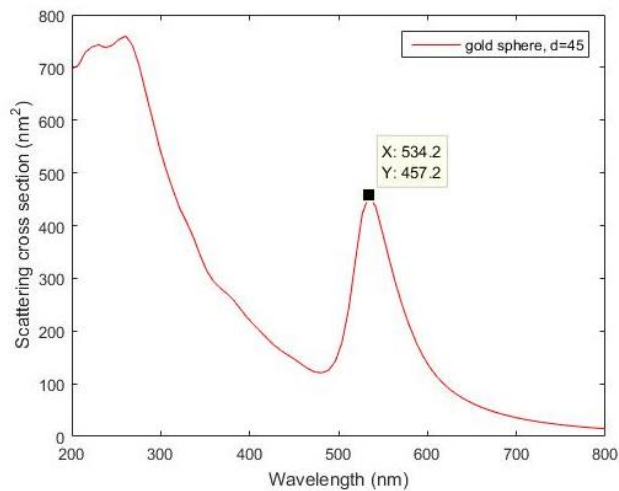
Figure 6.12: Scattering cross section plot for gold sphere, d=45 nm
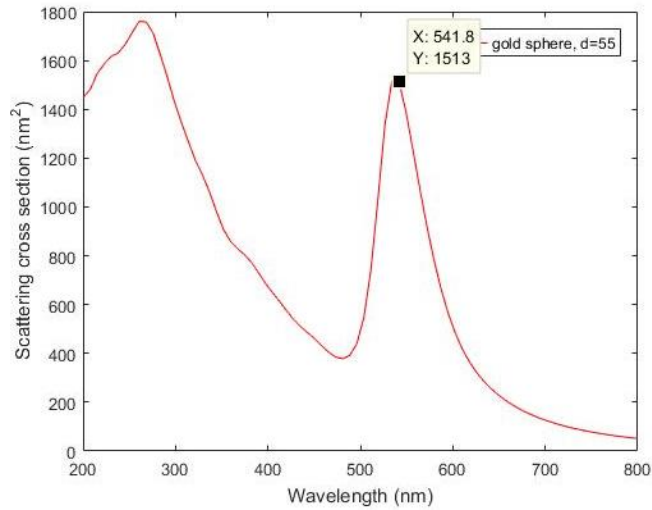
Figure 6.13: Scattering cross section plot for gold sphere, d=55 nm

Figure 6.14: Scattering cross section plot for gold sphere, d=65 nm

Figure 6.15: Scattering cross section plot for gold sphere, d=75 nm

Figure 6.16: Scattering cross section plot for gold sphere, d=85 nm

Figure 6.17: Scattering cross section plot for gold sphere, d=95 nm

Figure 6.18: Scattering cross section plot for gold sphere, d=105 nm

Figure 6.19: Scattering cross section plot for gold sphere, d=115 nm

Au Nanosphere Diameter (nm)	Peak Location (nm)
5	526.6
15	534.2
25	534.2
35	534.2
45	534.2
55	541.8
65	541.8
75	549.4
85	557.0
95	572.2
105	579.7
115	587.3

Table 6.1: Peak Location Values (nm) as a function of Gold Nanosphere Diameter.

Figure 6.20: Scattering cross section plot for two gold spheres, spacing = 0.3 nm

Figure 6.21: Scattering cross section plot for two gold spheres, spacing = 0.5 nm

Figure 6.22: Scattering cross section plot for two gold spheres, spacing = 0.7 nm

Figure 6.23: Scattering cross section plot for two gold spheres, spacing = 1 nm

Figure 6.24: Scattering cross section plot for two gold spheres, spacing = 1.5 nm

Figure 6.25: Scattering cross section plot for two gold spheres, spacing = 2 nm

Figure 6.26: Scattering cross section plot for two gold spheres, spacing = 3 nm

Figure 6.27: Scattering cross section plot for two gold spheres, spacing = 4 nm

Figure 6.28: Scattering cross section plot for two gold spheres, spacing = 5 nm

Figure 6.29: Scattering cross section plot for two gold spheres, spacing = 6 nm
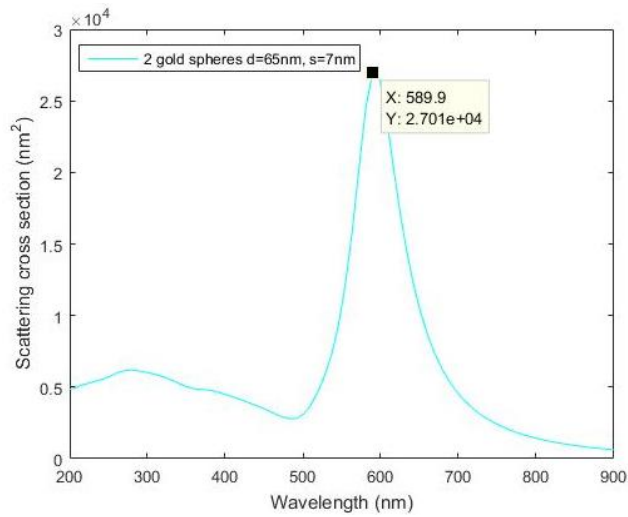
Figure 6.30: Scattering cross section plot for two gold spheres, spacing = 7 nm
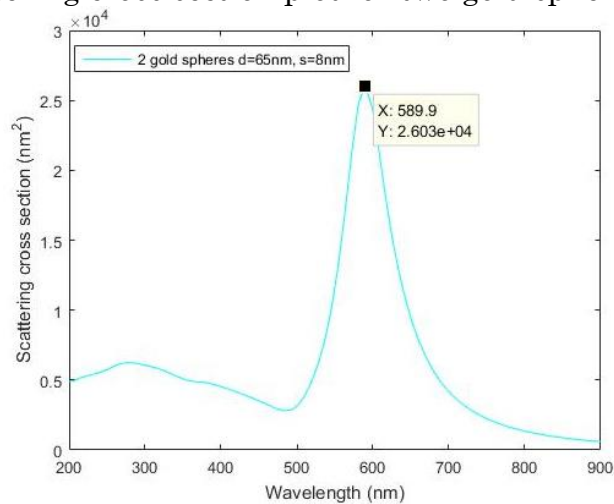
Figure 6.31: Scattering cross section plot for two gold spheres, spacing = 8 nm
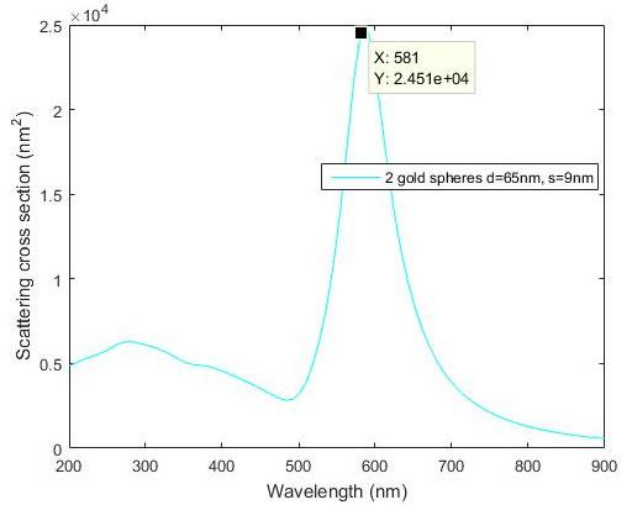
Figure 6.32: Scattering cross section plot for two gold spheres, spacing = 9 nm
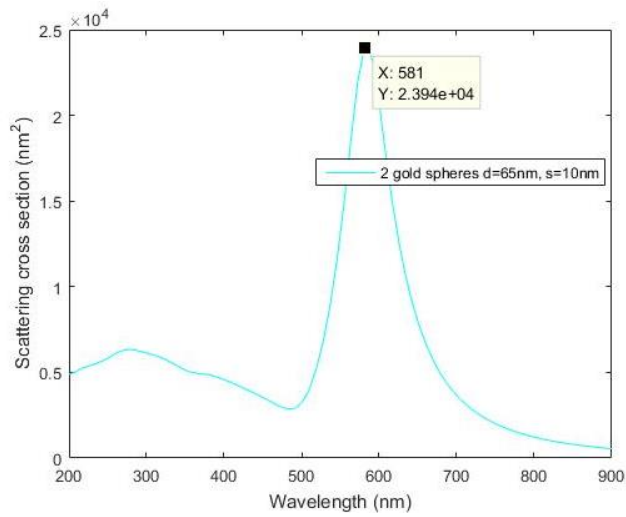
Figure 6.33: Scattering cross section plot for two gold spheres, spacing = 10 nm
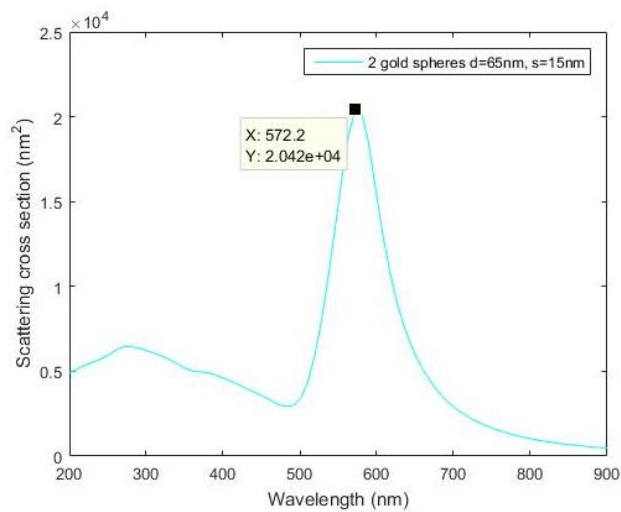
Figure 6.34: Scattering cross section plot for two gold spheres, spacing = 15 nm
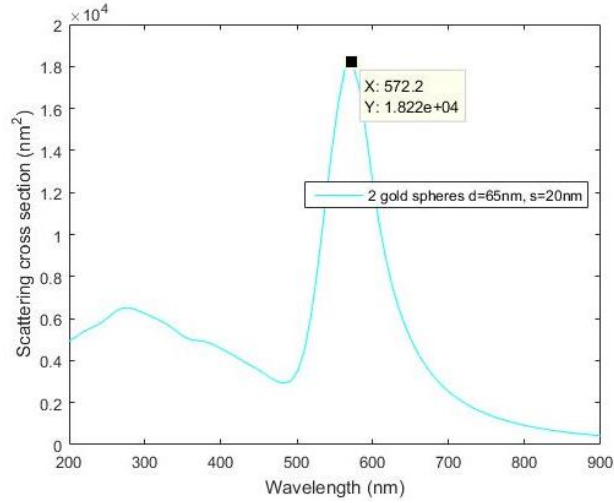
Figure 6.35: Scattering cross section plot for two gold spheres, spacing = 20 nm
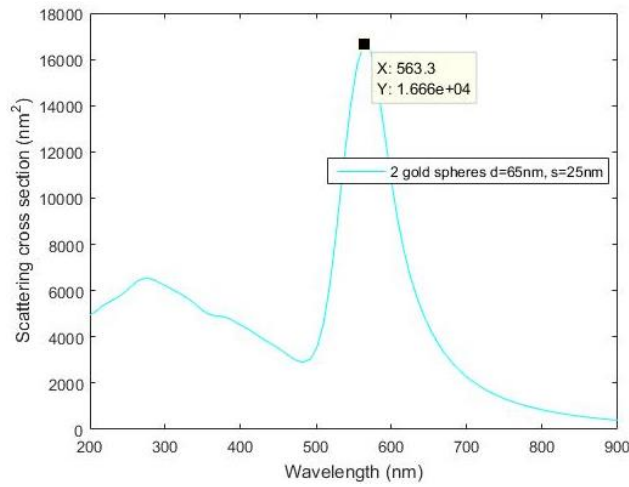
Figure 6.36: Scattering cross section plot for two gold spheres, spacing = 25 nm
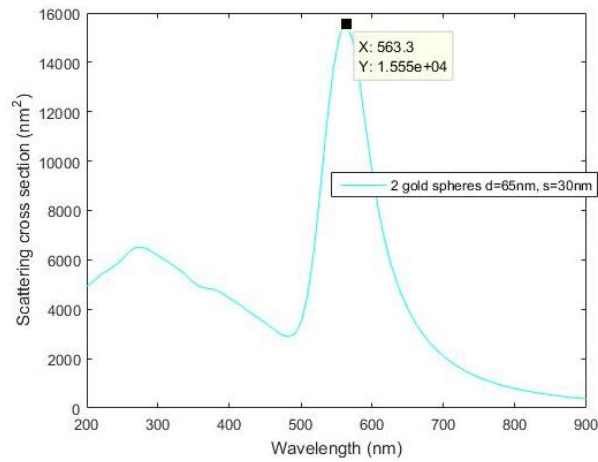
Figure 6.37: Scattering cross section plot for two gold spheres, spacing = 30 nm
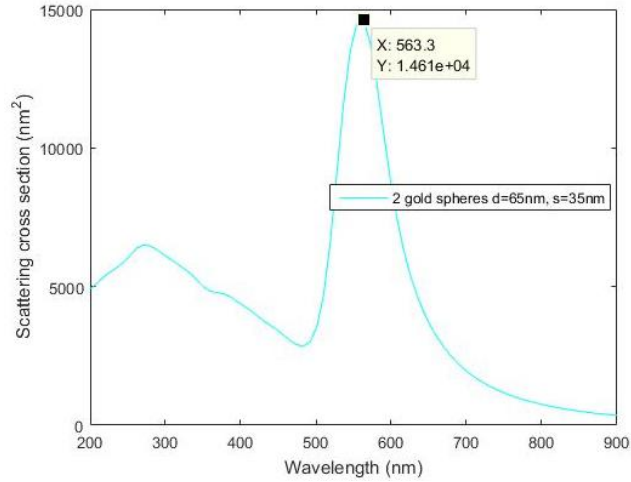
Figure 6.38: Scattering cross section plot for two gold spheres, spacing = 35 nm
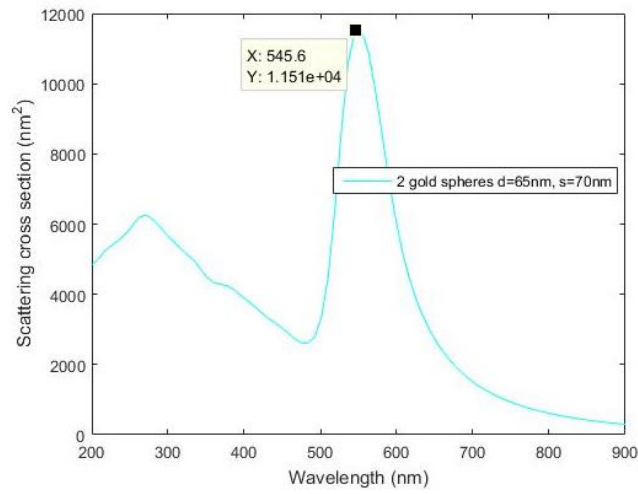
Figure 6.39: Scattering cross section plot for two gold spheres, spacing = 70 nm
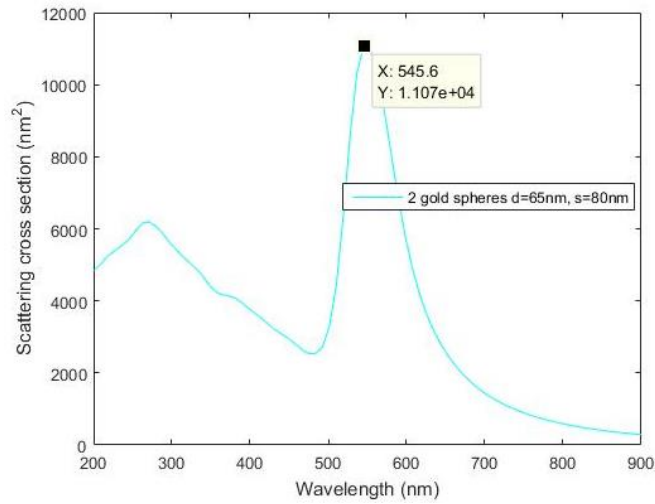
Figure 6.40: Scattering cross section plot for two gold spheres, spacing = 80 nm
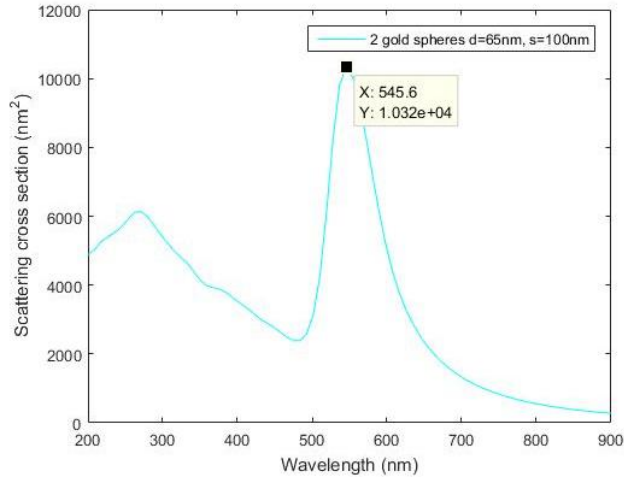
Figure 6.41: Scattering cross section plot for two gold spheres, spacing = 100 nm
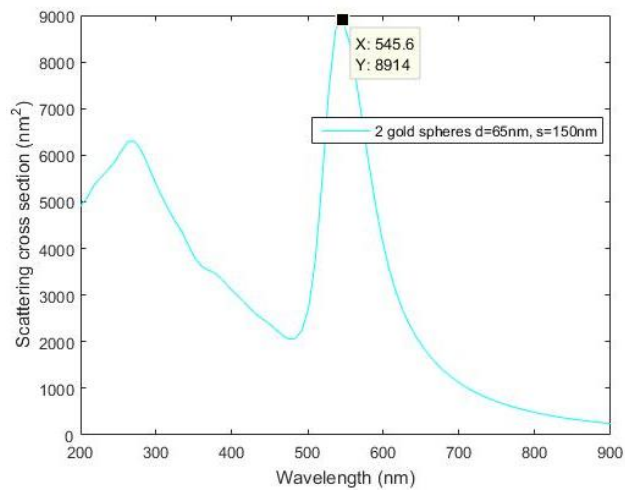
Figure 6.42: Scattering cross section plot for two gold spheres, spacing = 150 nm
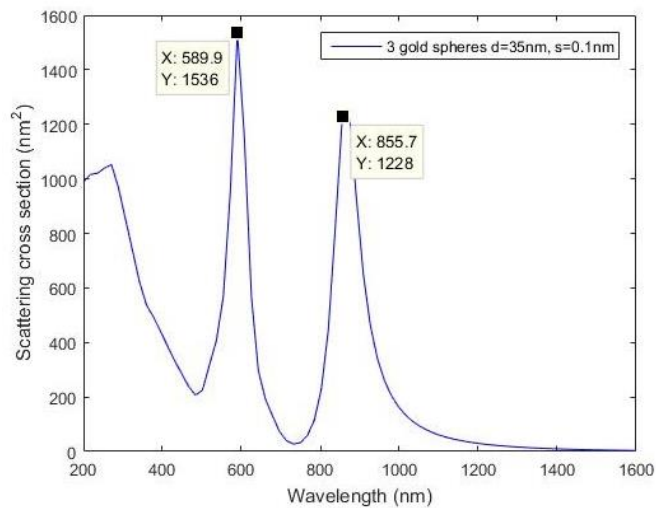
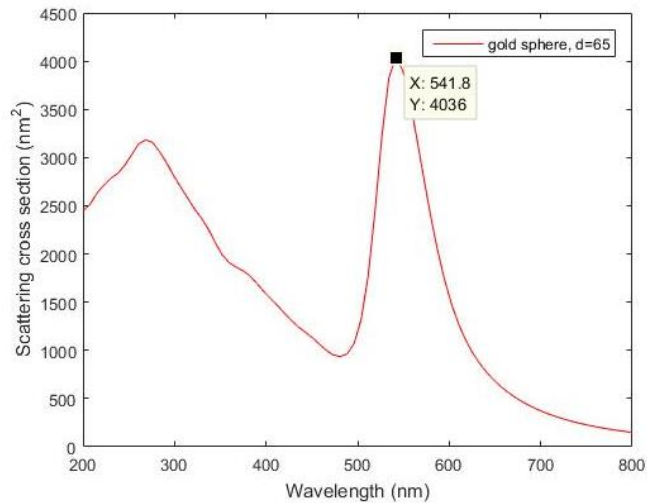Figure 6.43: Scattering cross section plot for three gold spheres, d=35 nm
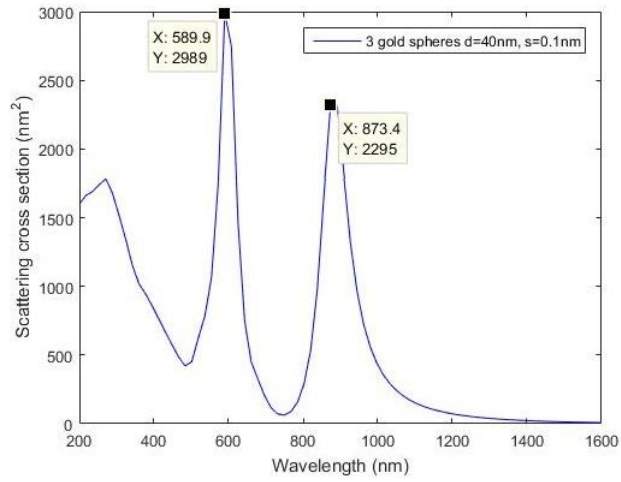
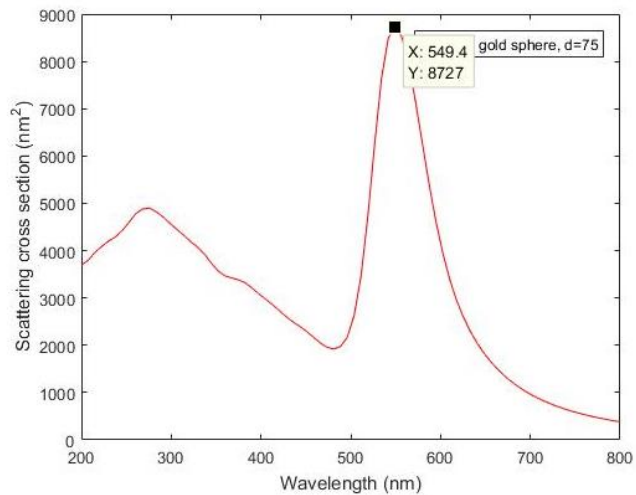Figure 6.44: Scattering cross section plot for three gold spheres, d=40 nm
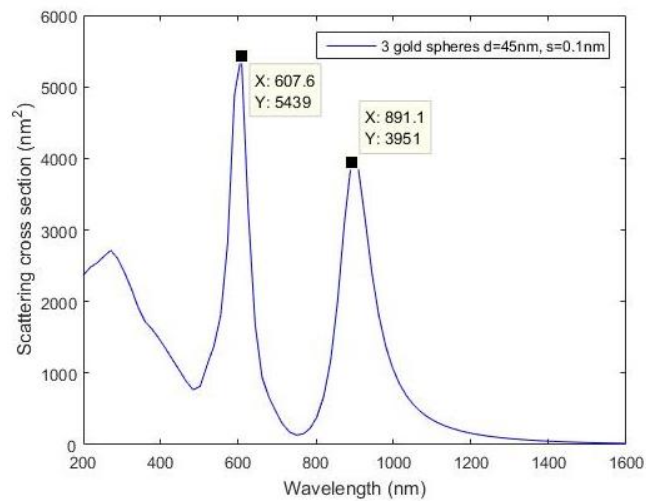
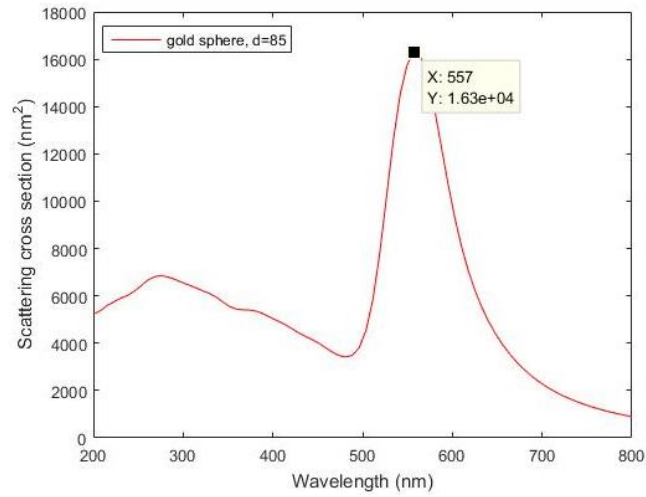Figure 6.45: Scattering cross section plot for three gold spheres, d=45 nm
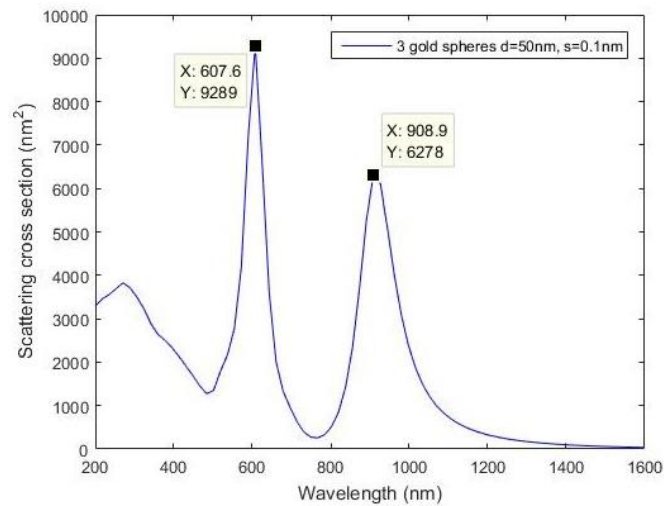
Figure 6.46: Scattering cross section plot for three gold spheres, d=50 nm
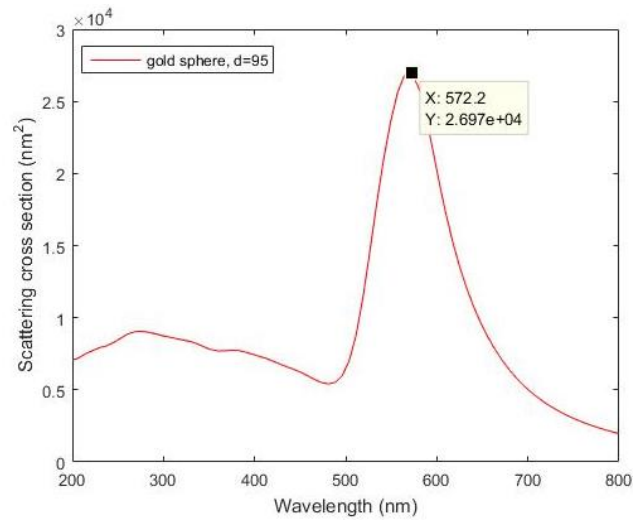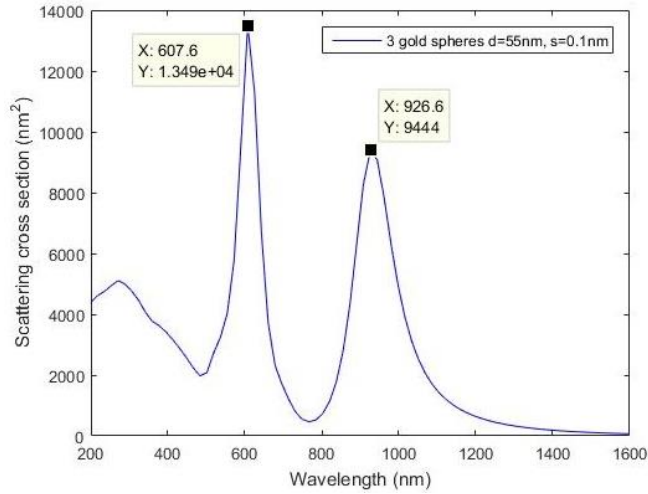
Figure 6.47: Scattering cross section plot for three gold spheres, d=55 nm
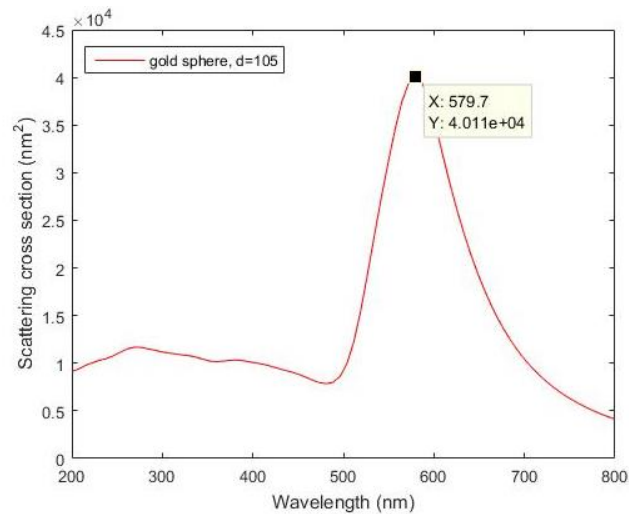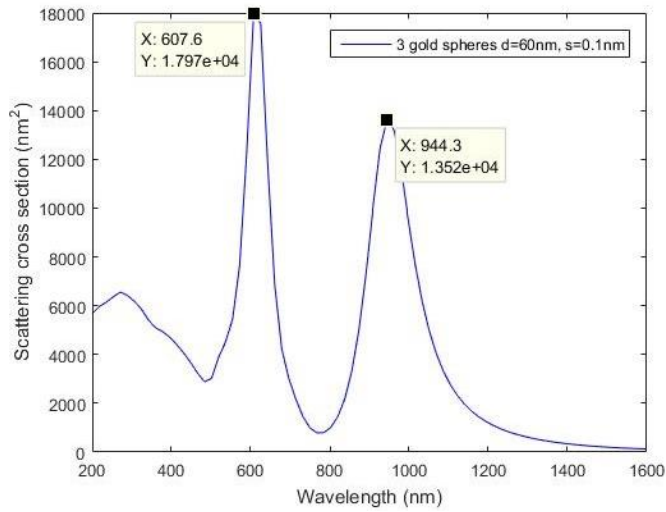

Figure 6.48: Scattering cross section plot for three gold spheres, d=60 nm
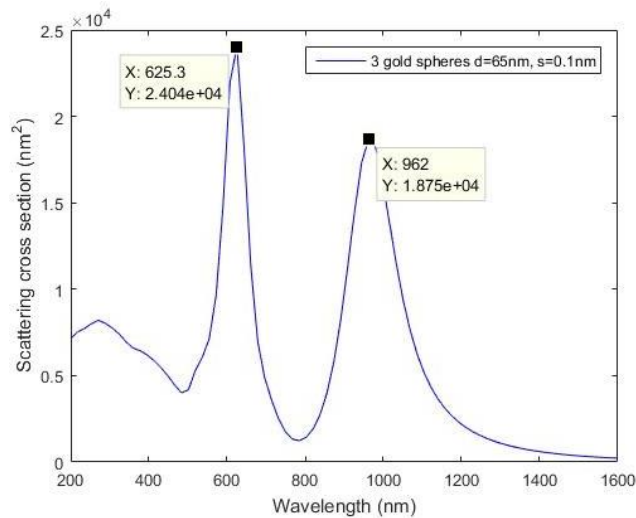
Figure 6.49: Scattering cross section plot for three gold spheres, d=65 nm
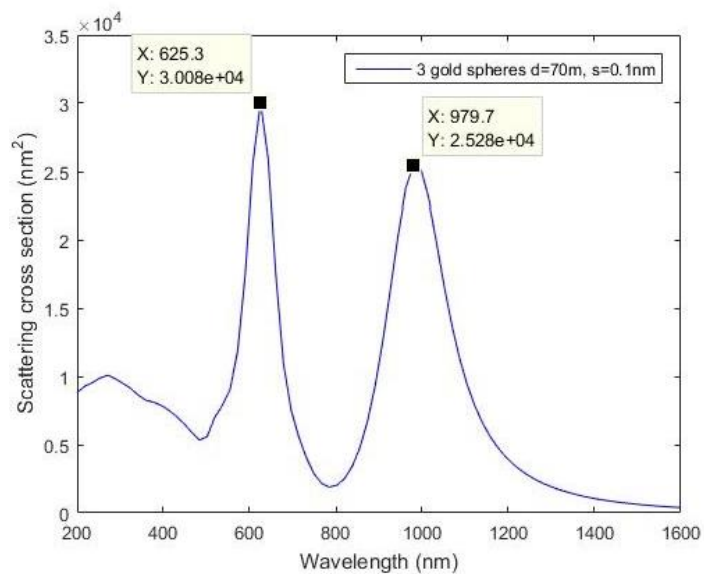
Figure 6.50: Scattering cross section plot for three gold spheres, d=70 nm

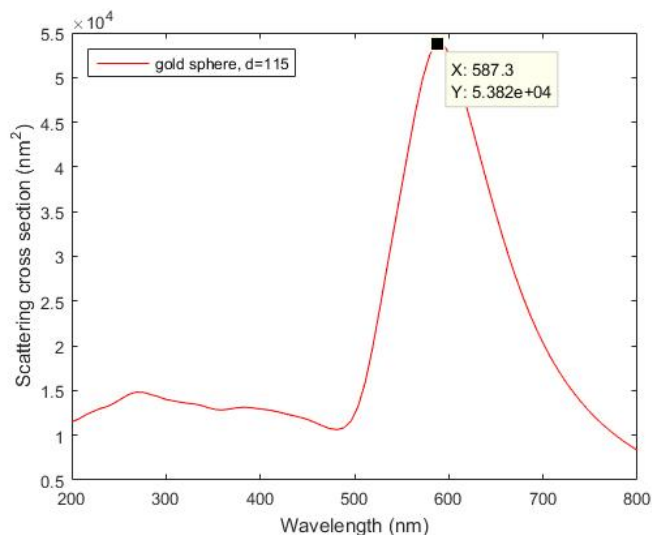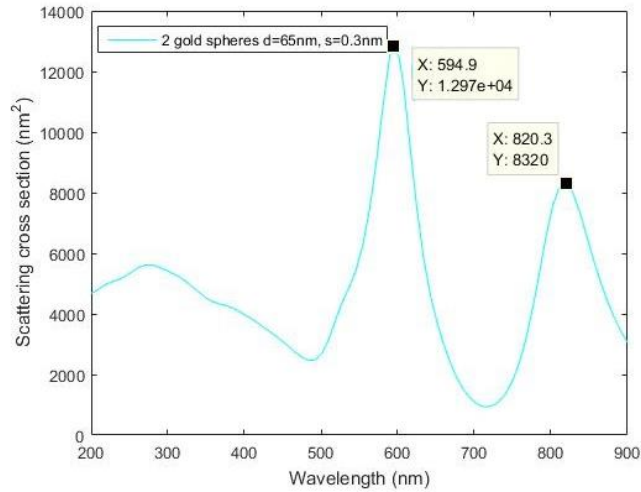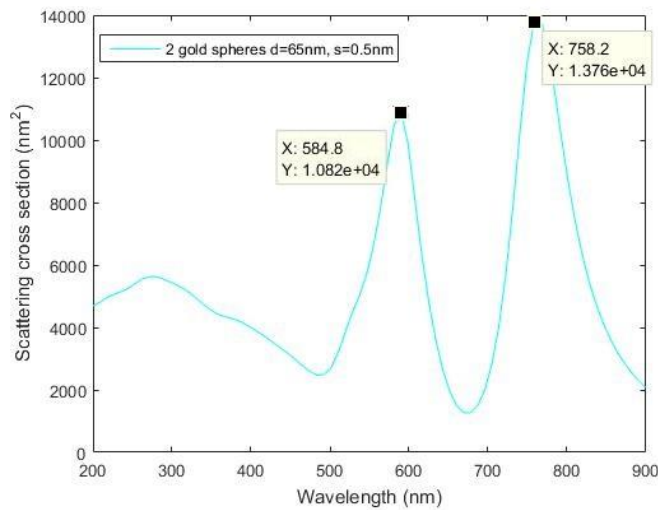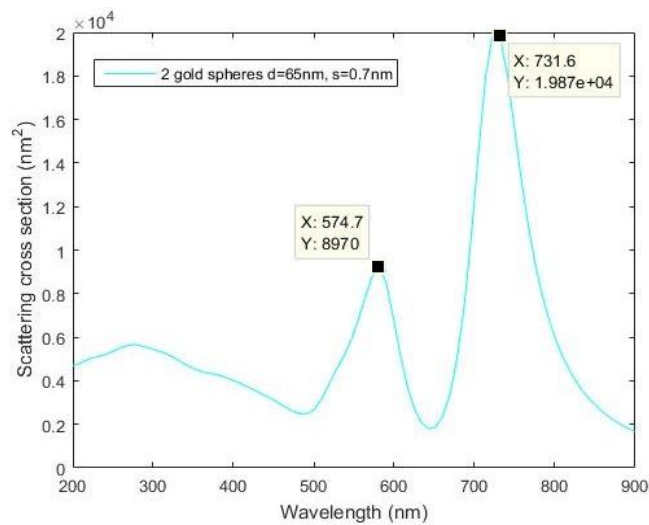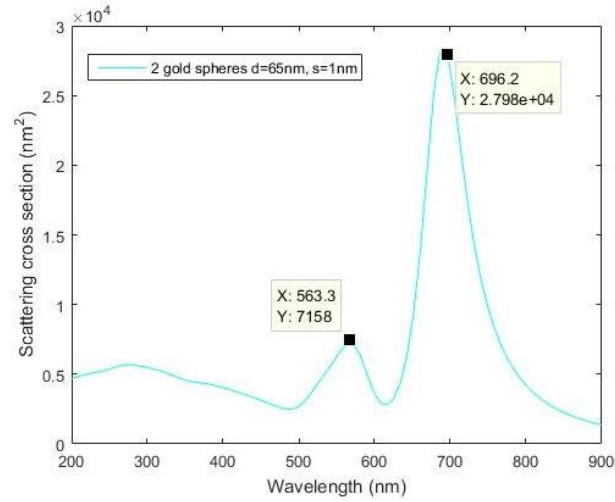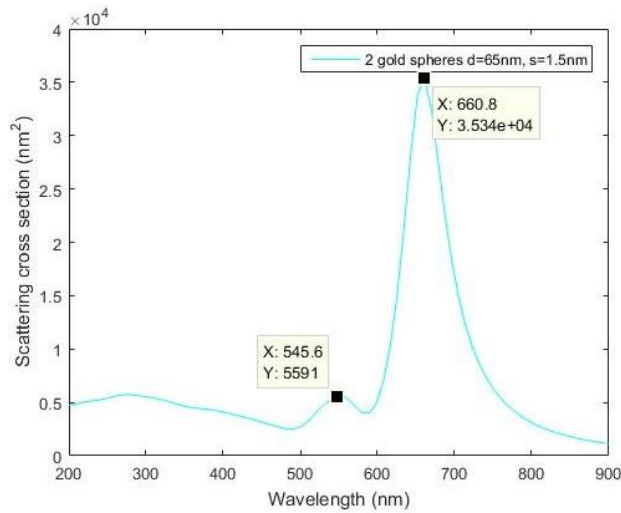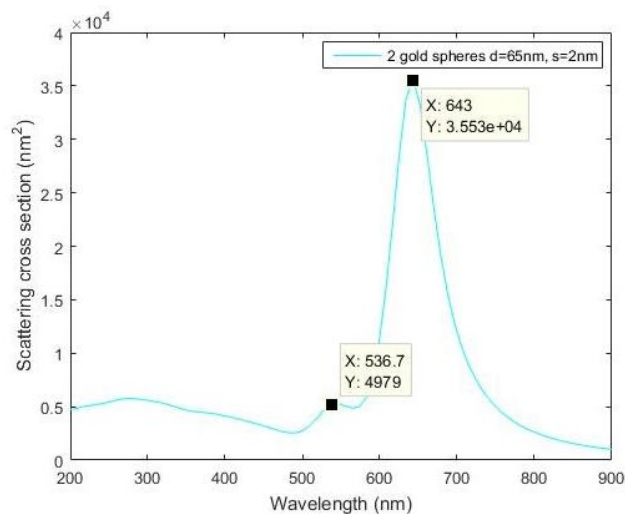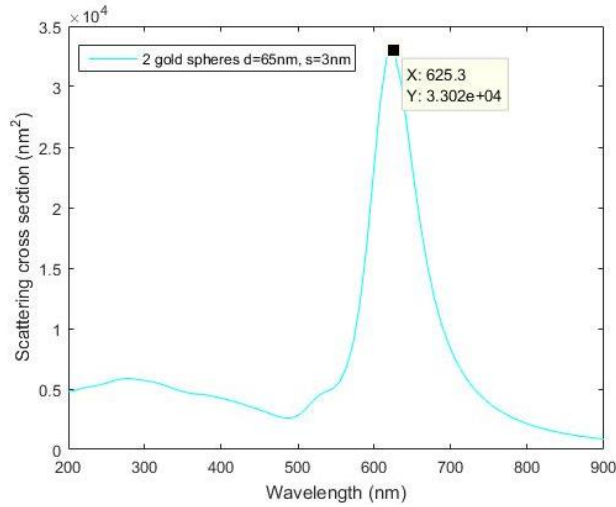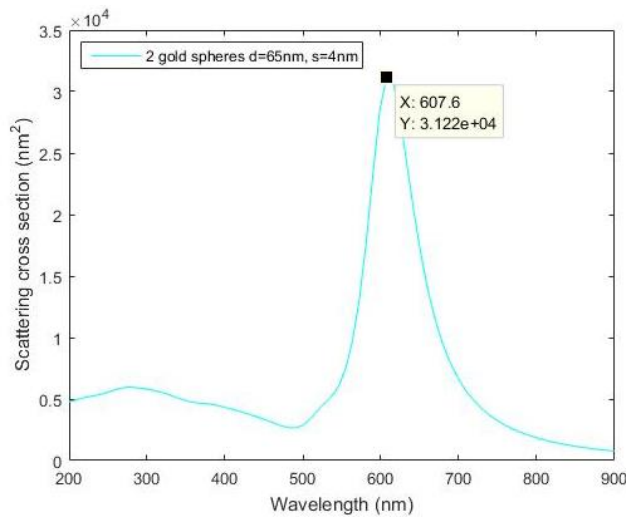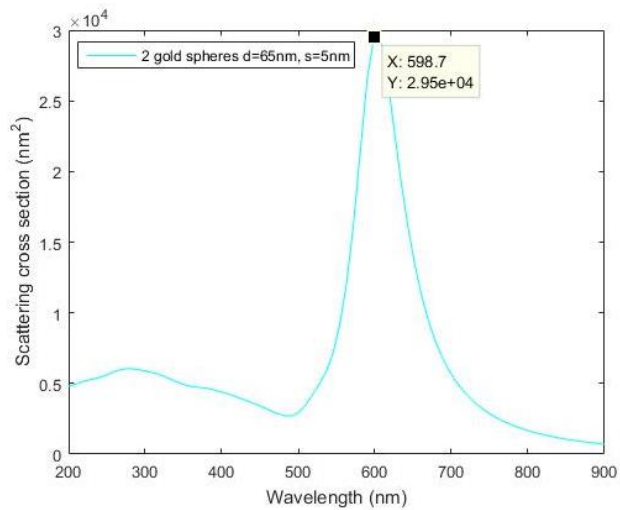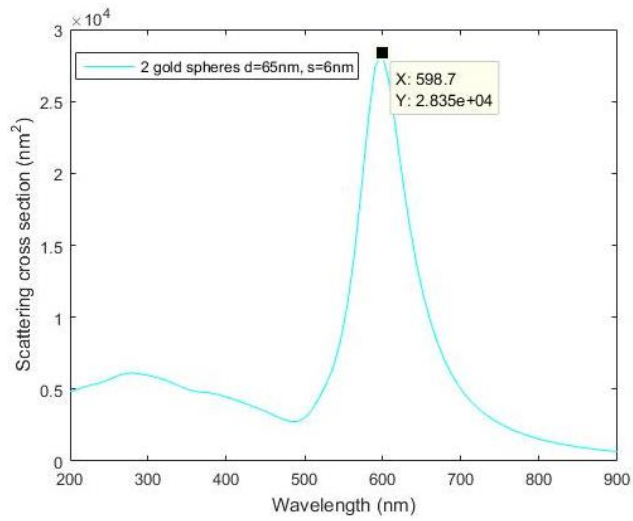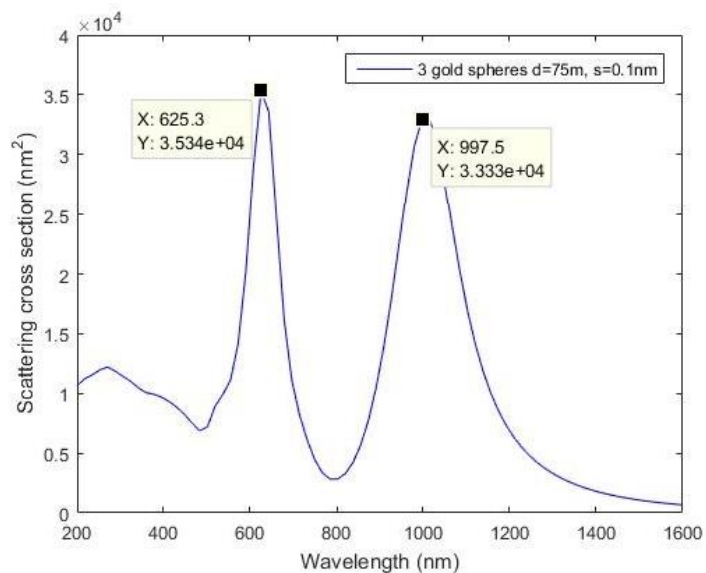Figure 6.51: Scattering cross section plot for three gold spheres, d=75 nm

References

1.   Schieber, M.; Lund, J.C.; Olsen, R.W.; McGregor, D.S.; VanScyoc, J.M.; James, R.B.; Soria, E. Material properties and room temperature nuclear detector response of wide band gap semiconductors. *Nuclear Inst. And Methods in Physics Research, A,* **1997,** *389*(3), 523

2.   Cardona, M.; Yu, P.Y. *Fundamentals of Semiconductors: Physics and Materials Properties,* 5th ed.; Springer: Berlin, **2010**

3.   Smith, R.A.; Yu, P.Y. *Semiconductors,* 2nd ed.; Cambridge University Press: Cambridge, **1978**

4.   Singh, J.; Yu, P.Y. *Semiconductor Devices: Basic Principles,* John Wiley and Sons: New York, **2001**

5.   Kuiper, P. Isolator-Metal. Wikimedia Commons. https://commons.wikimedia.org/wiki/File:Isolator-metal.svg/ **2007**

6.   Yin, L.W.; Bando, Y. Semiconductor morphology: optimizing properties by tuning morphology. *Nature Materials,* **2005,** *4*(12), 883-884

7.   Sun, Y.; Rogers, J.A.; Structural forms of single crystal semiconductor nanoribbons for high-performance stretchable electronics. *J. Mater. Chem,* **2007,** *17*(9), 832-840

8.   Fang, X.S.; Ye, C.H.; Peng, X.S.; Wang, Y.H.; Wu, Y.C.; Zhang, L.D. Temperature-controlled growth of α-Al_2O_3 nanobelts and nanosheets. *J. Mater. Chem,* **2003,** *13*(12), 3040-3043

9.   Fang, X.S.; Ye, C.H.; Zhang, L.D.; Xie, T. Twinning-mediated growth of Al2O3 nanobelts and their enhanced dielectric responses. *Adv. Mater.* **2006,** *17*(13), 1661-1665

10. Fang, X.; Bando, Y.; Gautam, U.K.; Ye, C.; Golberg, D. Inorganic semiconductor nanostructors and their field-emission applications. *J. Mater. Chem,* **2007,** *18*(5), 509-522

11. Fang, X.S.; Ye, C.H.; Zhang, L.D.; Zhang, J.X.; Zhao, J.W.; Yan, P. Direct observation of the growth process of MgO nanoflowers by a simple chemical route. *Small,* **2005,** *1*(4), 422-428

12. Ekimov, A.I.; Onushchenko, A.A. Quantum size effect in three-dimensional microscopic semiconductor crystals. *JETP Lett,* **1981**, *34*(6), 345–349

13. Alivisatos, A.P.; Semiconductor clusters, nanocrystals, and quantum dots. *Science,* **1996**, *271*(5251), 933-937

14. Wu, M.; Mukherjee, P.; Lamont, D. N.; Waldeck, D. H. Electron transfer and fluorescence quenching of nanoparticle assemblies. *J. Phys. Chem. C,* **2010**, *114*(13), 5751-5759

15. Markus, T. Z.; Wu, M.; Wang, L.; Waldeck, D. H.; Oron, D.; Naaman, R. Electronic structure of CdSe nanoparticles adsorbed on Au electrodes by an organic linker: fermi level pinning of the homo. *J. Phys. Chem. C,* **2009**, *113*(32), 14200-14206

16. Jose, R.; Zhanpeisov, N. U.; Fukumura, H.; Baba, Y.; Ishikawa, M. Structure-property correlation of CdSe clusters using experimental results and first-principles DFT calculations. *J. Am. Chem. Soc.* **2006,** *128*(2), 629-636

17. Park, Y.S.; Dmytruk, A.; Dmitruk, I.; Kasuya, A.; Takeda, M.; Ohuchi, N.; Okamoto, Y.; Kaji, N.; Tokeshi, M.; Baba, Y. Size selective growth and stabilization of small CdSe nanoparticles in aqueous solution. *ACS Nano,* **2010**, *4*(1), 121-128

18. Michalet, X.; Pinaud, F.F.; Bentolila, L.A.; Tsay, J.M.; Doose, S.; Li, J.J.; Sundaresan, G.; Wu, A.M.; Gambhir, S.S.; Weiss, S. Quantum dots for live cells, in vivo imaging, and diagnostics. *Science,* **2005,** *307*(5709), 538-544

19. Rogach, A.L. *Semiconductor nanocrystal quantum dots: synthesis, assembly, spectroscopy, and applications;* Springer: Austria, **2008**

20. Cox, J. A quantum paintbox. *Chem. Brit., 2003,* 39, *21-25*

21. Tayyebi, A.; Tavakoli, M.M.; Outokesh, M.; Shafiekhani, A.; Simchi, A. Supercritical synthesis and characterization of graphene-PbS quantum dots composite with enhanced photovoltaic properties. *Industrial & Engineering Chemistry Research,* **2015,** *54*(30), 7382-7392

22. Wang, X.; Koleilat, G.I.; Fischer, A.; Tang, J.; Debnath, R.; Levina, L.; Sargent, E.H. Enhanced open-circuit voltage in visible quantum dot photovoltaics by engineering of carrier-collecting electrodes. *ACS Appl. Mater. Interfaces,* **2011,** *3*(10), 3792-3795

23. Tang, J.; Sargent, E.H. Infrared colloidal quantum dots for photovoltaics: fundamentals and recent progress. *Advanced Materials,* **2011,** *23*(1), 12-29

24. Tavakoli, M.M.; Tayyebi, A.; Simchi, A.; Aashuri, H.; Outokesh, M.; Fan, Z. Physicochemical properties of hybrid graphene-lead sulfide quantum dots prepared by supercritical ethanol. *J. Nanopart. Res.,* **2015,** *17*(1), 1-13

25. Brus, L.E. Electron-electron and electron-hole interactions in small semiconductor crystallites: the size dependence of the lowest excited electronic state. *J. Chem. Phys.,* **1984,** *80*(9), 4403-4409

26. Markus, T.Z.; Itzhakov, S.; Alkotzer, Y.I.; Cahen, D.; Hodes, G.; Oron, D.; Naaman, R. Energetics of CdSe quantum dots adsorbed on TiO_2. *J. Phys. Chem. C,* **2011,** *115*(27), 13236-13241

27. Klostranec, J.M.; Chan, W.C.W. Quantum dots in biological and biomedical research: recent progress and present challenges. *Adv. Mater.* **2006,** *18*(15), 1953-1964

28. Park, N.M.; Kim, T.S.; Park, S.J. Band gap engineering of amorphous silicon quantum dots for light-emitting diodes. *Appl. Phys. Lett.,* **2001,** *78*(17), 2575-2577

29. Sun, Q.; Wang, Y.A.; Li, L.S.; Wang, D.Y.; Zhu, T.; Xu, J.; Yang, C.H.; Li, Y.F. Bright, multicoloured light-emitting diodes based on quantum dots. *Nat. Photonics,* **2007,** *1*(12), 717-722

30. Lee, D.C.; Robel, I.; Pietryga, J.M.; Klimov, V.I. Infrared-active heterostructured nanocrystals with ultralong carrier lifetimes. *J. Am. Chem. Soc.,* **2010,** *132*(29), 9960-9962

31. Pietryha, J.M.; Werder, D.J.; Williams, D.J.; Casson, J.L.; Schaller, R.D.; Klimov, V.I.; Hollingsworth, J.A. Utilizing the lability of lead selenide to produce heterostructured nanocrystals with bright, stable infrared emission. *J. Am. Chem. Soc.,* **2008,** *130*(14), 4879-4885

32. Chen, Y.; Vela, J.; Htoon, H.; Casson, J.L.; Werder, D.J.; Bussian, D.A.; Klimov, V.I. Hollingsworth, J.A. "Giant" multishell CdSe nanocrystal quantum dots with supressed blinking. *J. Am. Chem. Soc.,* **2008,** *130*(15), 5026-5027

33. Mahler, B.; Spinicelli, P.; Buil, S.; Quelin, X.; Hermier, J.P.; Dubertret, B. Towards non-blinking colloidal quantum dots. *Nature Materials,* **2008**, *7*(8), 659-664

34. Zhou, D.; Li, Y.; Hall, E.A.H.; Abel, C.; Klenerman, D. A Chelating dendritic ligand capped quantum dot: preparation, surface passivation, and specific DNA detection. *Nanoscale,* **2011,** *3* (1), 201-211

35. Lee, S.F.; Osborne, M.A. Photodynamics of a single quantum dot: fluorescence activation, enhancement, intermittency, and decay. *J. Am. Chem. Soc.,* **2007**, *129* (29), 8936-8937

36. Van Sark, W.G.J.H.M.; Frederix, P.L.T.M.; Van de Heuval, D.J.; Gerritsen, H.C. Photooxidation and photobleaching of single CdSe/ZnS quantum dots probed by room-temperature time-resolved spectroscopy. *J. Phys. Chem. B,* **2001**, *105* (35), 8281-8284

37. Lee, S.F.; Osborne, M.A. Brightening, blinking, blueing and bleaching in the life of a quantum dot: friend or foe? *ChemPhysChem*, **2009**, *10* (13), 2174-2191

38. Julien, C. Our Technology: What is a Quantum Dot? 2016. NanoPhotonica, nanophotonica.com/technology/#toggle-id-1 **2016**

39. Erwin, S.C.; Zu, L.; Haftel, M.I.; Efros, A.L.; Kennedy, T.A.; Norris, D.J. Doping semiconducting nanocrystals. *Nature,* **2005**, *436*(7047), 91-94

40. Beaulac, R.; Schneider, L.; Archer, P.I.; Bacher, G.; Gamelin, D.R. Light-induced spontaneous magnetization in doped colloidal quantum dots. *Science,* **2009,** *325*(5943), 973-976

41. Wu, P.; Yan, X.P. Doped quantum dots for chemo/biosensing and bioimaging. *Chem. Soc. Rev.,* **2013,** *42*(12), 5489-5521

42. Wang, X.; Yan, X.; Li, W.; Sun, K. Doped quantum dots for white-light emitting diodes without reabsorption of multiphase phosphors. *Adv. Mater.* **2012,** *24*(20), 2742-2747

43. Sahu, A.; Kang, M.S.; Kompch, A.; Notthoff, C.; Wills, A.W.; Deng, D.; Winterer, M.; Frisbie, C.D.; Norris, D.J. Electronic impurity doping in CdSe nanocrystals. *Nano Letters,* **2012,** *12*(5), 2587-2594

44. Norris, D.J.; Efros, A.L.; Erwin, S.C. Doped nanocrystals. *Science*, **2008,** *319*(5871), 1776-1779

45. Shim, M.; Guyot-Sionnest, P. n-type colloidal semiconductor nanocrystals. *Nature,* **2000,** *407*(6807), 981-983

46. Yu, D.; Wang, C.; Guyot-Sionnest, P. n-type conducting CdSe nanocrystal solids. *Science,* **2003,** *300*(5623), 1277-1280

47. Talapin, D.V.; Murray, C.B. PbSe nanocrystal solids for n- and p- channel thin film field-effect transistors. *Science,* **2005,** *310*(5745), 86-89

48.   Bekenstein, Y.; Vinokurov, K.; Keren-Zur, S.; Schilt, Y.; Raviv, U.; Millo, O.; Banin, U. Thermal doping by vacancy formation in copper sulfide nanocrystal arrays. *Nano Lett.,* **2014,** *14*(3), 1349-1353

49.   Choi, J.H.; Fafarman, A.T.; Oh, S.J.; Ko, D.K.; Kim, D.K.; Diroll, B.T.; Muramoto, S.; Gillen, J.G.; Murray, C.B.; Kagan, C.R. Bandlike transport in strongly coupled and doped quantum dot solids: a route to high-performance thin-film electronics. *Nano Lett.,* **2012,** *12*(5), 2631–2638.

50.   Wang, C.; Shim, M.; Guyot-Sionnest, P. Electrochromic nanocrystal quantum dots. *Science,* **2001,** *291*(5512), 2390-2392

51.   Dalpian, G.M.; Chelikowsky, J.R. Self-purification in semiconducting nanocrystals. *Phys. Rev. Lett.,* **2006,** *96*(22), 226802

52.   Chan, T.L.; Tiago, M.L.; Kaxiras, E.; Chelikowsky, J.R. Size limits on doping in phosphorus into silicon nanocrystals. *Nano Lett.,* **2008,** *8*(2), 596-600

53.   Turnbull, D. Formation of crystal nuclei in liquid metals. *J. Appl. Phys.,* **1950,** *21*(10), 1022-1028

54.   Edmond, J.T.; Hilsum, C. Heat treatment effects in indium arsenide. *J. Appl. Phys.,* **1960,** *31*(7), 1300-1301

55.   Yang, Y.; Chen, O.; Angerhofer, A.; Cao, Y.C. Radial-position-controlled doping in CdS/ZnS core/shell nanocrystals. *J. Am. Chem. Soc.,* **2006,** *128* (38), 12428-12429

56.   Avinor, M.; Meijer, G. Emission of activated cadmium selenide phosphors. *J. Chem. Phys.,* **1960,** *32*(5), 1456-1458

57.   Robinson, A.L.; Bube, R.H. Photoelectronic properties of defects in CdSe single crystals. *J. Appl. Phys.,* **1971,** *42*(13), 5280-5295

58.   Swaminathan, V.; Greene, L.C. Low temperature photoluminescence in Ag-doped ZnSe. *J. Lumin.* **1976,** *14*(3), 357-363

59.   Mocatta, D.; Cohen, G.; Schattner, J.; Millo, O.; Rabani, E.; Banin, U. Heavily doped semiconductor nanocrystal quantum dots. *Science*, **2011,** *332*(6025), 77-81

60.   Kang, M.S.; Sahu, A.; Frisbie, C.D.; Norris, D.J. Influence of silver doping on electron transport in thin films of PbSe nanocrystals. *Adv. Mater.,* **2013,** 25(5), 725-731

61. Hines, M.A.; Guyot-Sionnest, P. Synthesis and characterization of strongly luminescing ZnS-capped CdSe nanocrystals. *J. Phys. Chem.,***1996,** 100(2), 468-471

62. Dabbousi, B.O.; Rodriguez-Viejo, J.; Mikulec, F.V.; Heine, J.R.; Mattoussi, H.; Ober, R.; Jensen, K.F.; Bawendi, M.G. (CdSe)ZnS core-shell quantum dots: synthesis and characterization of a size series of highly luminescent nanocrystallites. *J. Phys. Chem. B,* **1997,** 101(46), 9463-9475

63. Burke, K. *The ABC of DFT*. Department of Chemistry: University of California, 2007, 1-208. chem.ps.uci.edu/~kieron/dft/book/ **2016**

64. Kock, W.; Holthausen, M.C. *A chemist's guide to density functional theory.* Wiley: New York, **2001**

65. Corminboeuf, C.; Tran, F.; Weber, J. The role of density functional theory in chemistry: some historical landmarks and applications to zeolites. *Journal of Molecular Structure,* **2006**, *762*(1), 1-7

66. Sutcliffe, B.T.; Woolley, R.G.; Molecular structure calculations without clamping the nuclei. *Phys. Chem. Chem. Phys.,* **2005,** *7*(21), 3664-3676

67. Hohenberg, P.; Kohn, W. Inhomogeneous electron Gas. *Phys. Rev.* **1964,** *136*(3B), 864-871

68. Sholl, D.S.; Steckel, J.A. *Density Functional Theory: A Practical Introduction.* John Wiley & Sons, Inc: New Jersey, **2009**, 10-12

69. Burke, K.; Wagner, L.O. DFT in a nutshell. *International J. Quantum Chem*, **2013**, *113*(2), 96-101

70. Kohn, W.; Sham, L.J. Self-consistent equations including exchange and correlation effects. *Phys. Rev.* **1965,** *140*(4A), 1133-1138

71. Kuhne, T.D. Ab-initio molecular dynamics. *WIREs Comput. Mol. Sci.,* **2014,** *4*, 391-404

72. Car, R.; Parrinello, M. Unified approach for molecular dynamics and density-functional theory. *Phys. Rev. Lett.,* **1985,** *55*(22), 2471-2474

73. Born, M.; Huang, K. *Dynamical theory of crystal lattices*. Oxford University Press: Oxford, **2000**

74. Bolhuis, P.G.; Chandler, D.; Dellago, C.; Geissler, P.L. Transition path sampling: throwing ropes over rough mountain passes, in the dark. *Annu. Rev. Phys. Chem.,* **2002,** *531*(1), 291-318

75. Boero, M.; Parrinello, M.; Terakura, K.; Weiss, H. Car-Parrinello study of Zeilger-Natta heterogeneous catalysis: stability and destabilization problems of the active site models. *Mol. Phys.,* **2002,** *100*(18), 2935-2940

76. Jones, R.O.; Gunnarsson, O. The density functional formalism, its applications and prospects. *Rev. Mod. Phys.,* **1989,** *61*(3), 689-746

77. Mori-Sanchez, P.; Cohen, A.J.; Yang, W. Localization and delocalization errors in density functional theory and implications for band-gap prediction. *Phys. Rev. Lett.,* **2008,** *100*(14), 146401-146404

78. Perdew, J.P.; Levy, M. Physical content of the exact Kohn-Sham orbital energies: band gaps and derivative discontinuities. *Phys. Rev. Lett.,* **1983,** *51*(20), 1884-1887

79. Sham, L.J.; Schlüter, M. Density-functional theory of the energy gap. *Phys. Rev. Lett.,* **1983,** *51*(20), 1888-1891

80. Dreizler, R.M.; Providência, J. *Density functional methods in physics.* Plenum Press: New York and London, **1985,** 265-308

81. Assadi, M.H.N.; Hanaor, D.A.H. Theoretical study on copper's energetics and magnetism in TiO2 polymorphs. *J. Appl. Phys.,* **2013,** *113*(23), 233913-233918

82. Kristyán, S.; Pulay, P. Can (semi)local density functional theory account for the London dispersion forces? *Chem. Phys. Lett.* **1994,** *229*(3), 175-180

83. Pérez-Jordá, J.M.; Becke, A.D. A density-functional study of van der Waals forces: rare gas diatomics. *Chem. Phys. Lett.* **1995,** *233*(1), 134-137

84. Craig, D.P.; Thirunamachandran, T. *Molecular quantum electrodynamics.* Dover Publications, Inc.: Mineola, New York, **1998**

85. Pérez-Jordá, J.M.; San-Fabián, E.; Pérez-Jiménez, A.J. Density-functional study of van der Waals forces on rare-gas diatomics: Hartree-Fock exchange. *J. Chem. Phys.,* **1999,** *110*(4), 1916-1920

86. Werder, T.; Walther, J.H.; Jaffe, R.L.; Halicioglu, T.; Koumoutsakos, P. On the water-carbon interactions for use in molecular dynamics simulations of graphite and carbon nanotubes. *J. Phys. Chem. B,* **2003,** *107*(6), 1345-1352

87.   Oliveira, A.F.; Seifert, G.; Heine, T.; Duarte, H.A. Density-functional based tight-binding: an approximate DFT method. *Journal of the Brazilian Chemical Society,* **2009,** *20*(7), 1193-1205

88.   Sharma, A.N.; Kumar, U.; Sing, V.N., Mehta, B.R.; Kakkar, R. Surface modification of CdSe quantum dots for biosensing applications: role of ligands. *Thin Solid Films,* **2010,** *519*(3), 1202-1212

89.   Samia, A.C.S.; Chen, X.; Burda, C. Semiconductor quantum dots for photodynamic therapy. *J. Am. Chem. Soc.,* **2003,** *125*(51), 15736-15737

90.   Bakalova, R.; Ohba, H.; Zhelev, Z.; Ishikawa, M.; Baba, Y. Quantum dots as photosensitizers? *Nat. Biotechnol.,* **2004,** *22*(11), 1360-1361

91.   Azzazy, H.M.; Mansour, M.M.; Kazmierczak, S.C. From diagnostics to therapy: prospects of quantum dots. *Clin. Biochem.*, **2007,** *40*(13-14), 917-927

92.   Vibin, M.; Vinayakan, R.; John, A.; Raji, V.; Rejiya, C.; Vinesh, N.; Abraham, A. Cytotoxicity and fluorescence studies of silica-coated CdSe quantum dots for bioimaging applications. *J. Nanopart. Res.,* **2011,** *13*(6), 2587-2596

93.   Lopez-Luke, T.; Wolcott, A.; Xu, L.P.; Chen, S.; Wen, Z.; Li, J.; De La Rosa, E.; Z, J.Z. Nitrogen-doped and CdSe quantum-dot sensitized nanocrystalline TiO2 films for solar energy conversion applications. *J. Phys. Chem. C.,* **2008,** *112*(4), 1282-1292

94.   Altintas, Y.; Genc, S.; Tulpar, M.Y.; Mutlugun, E. CdSe/ZnS quantum dot films for high performance flexible lighting and display applications. *Nanotechnology,* **2016,** *27*(29), 295604-295613

95.   Webber, D.H.; Brutchey, R.L. Ligand exchange on colloidal CdSe nanocrystals using thermally labile *tert*-butylthiol for improved photocurrent in nanocrystal films. *J. Am. Chem. Soc.,* **2011,** *134*(2), 1085-1092

96.   Wang, W.; Banerjee, S.; Jia, S.; Steigerwald, M. L.; Herman, I. P. Ligand control of growth, morphology, and capping structure of colloidal CdSe nanorods. *Chem. Mater.,* **2007,** *19*(10), 2573–2580

97.   Li, Z.; Peng, X. Size/shape-controlled synthesis of colloidal CdSe quantum disks: ligand and temperature effects. *J. Am. Chem. Soc.,* **2011,** *133*(17), 6578–6586

98. Gao, Y.; Peng, X. crystal structure control of CdSe nanocrystals in growth and nucleation: dominating effects of surface versus interior structure. *J. Am. Chem. Soc.,* **2014,** *136*(18), 6724–6732

99. García-Rodríguez, R.; Liu, H. Mechanistic insights into the role of alkylamine in the synthesis of CdSe nanocrystals. *J. Am. Chem. Soc.,* **2014,** *136*(5), 1968–1975

100. Yu, W.W.; Wang, Y.A.; Peng, X. Formation and stability of size-, shape-, and structure-controlled CdTe nanocrystals: ligand effects on monomers and nanocrystals. *Chem. Mater.,* **2003,** *15*(22), 4300–4308

101. Talapin, D.V.; Rogach, A.L.; Kornowski, A.; Haase, M.; Weller, H. Highly luminescent monodisperse CdSe and CdSe/ZnS nanocrystals synthesized in a hexadecylamine-trioctylphosphine oxide-trioctylphospine mixture. *Nano Lett.,* **2001,** *1*(4), 207–211

102. Kadlag, K.P.; Rao, M.J.; Nag, A. Ligand-free, colloidal, and luminescent metal sulfide nanocrystals. *J. Phys. Chem. Lett.,* **2013,** *4*(10), 1676–1681

103. Grandhi, G.K.; Swathi, K.; Narayan, K.S.; Viswanatha, R. Cu doping in ligand free CdS nanocrystals: conductivity and electronic structure study. *J. Phys. Chem. Lett.,* **2014,** *5*(13), 2382–2389

104. Bullen, C.; Mulvaney, P. The effects of chemisorption on the luminescence of CdSe quantum dots. *Langmuir,* **2006,** *22*(7), 3007– 3013

105. Blum, A.S.; Soto, C.M.; Wilson, C.D.; Whitley, J.L.; Moore, M.H.; Sapsford, K.E.; Lin, T.; Chatterji, A.; Johnson, J.E.; Ratna, B.R. Templated self-assembly of quantum dots from aqueous solution using protein scaffolds. *Nanotechnology,* **2006,** *17*(20), 5073-5079

106. Aihara, J. Reduced HOMO-LUMO gas as an index of kinetic stability for polycyclic aromatic hydrocarbons. *J. Phys. Chem. A,* **1999,** *103*(37), 7487-7495

107. Sher, A. (1985). *WO 1985003598 A1,* Sri International.

108. Trügler, A. *Optical Properties of Metallic Nanoparticles: Basic Principles and Simulation.* Springer: Switzerland, **2016**, 21

109. Waxenegger, J.; Trügler, A.; Hohenester, U. Plasmonics simulations with the MNPBEM toolbox: consideration of substrates and layer structures. *Comp. Phys. Commun.,* **2015,** *193,* 138-150

110. Lamprecht, B. Ultrafast plasmon dynamics in metal nanoparticles. Ph.D. thesis, Institut für Physik, Karl-Franzens-Universität Graz, **2000**

111. Perez-Juste, J.; Pastoriza-Santos, I.; Liz-Marzan, L.M.; Mulvaney, P. Gold nanorods: synthesis, characterization and applications. *Coordination Chemistry Reviews,* **2005,** *249*(17), 1870-1901

112. NanoHybrids. Plasmonics and Surface Plasmon Resonance. https://nanohybrids.net/pages/plasmonics, 2017

113. Liu, S.; Chen, G.; Prasad, P.N.; Swihart, M.T. Synthesis of monodisperse Au, Ag, and Au-Ag alloy nanoparticles with tunable size and surface plasmon resonance frequency. *Chemistry of Materials,* **2011**, *23*(18), 4098-4101

114. Cytodiagnostics Inc. Gold Nanoparticle Properties, 2016. Cytodiagnostics Inc, www.cytodiagnostics.com/store/pc/Gold-Nanoparticle-Properties-d2.htm, **2016**

115. Hohenester, U. Simulating electron energy loss spectroscopy with the MNPBEM toolbox. *Comp. Phys. Commun.,* **2014,** *185*(3), 1177-1187

116. Hohenester, U.; Trügler, A. MNPBEM – A Matlab toolbox for the simulation of plasmonic nanoparticles. *Comp. Phys. Commun.,* **2012**, *183*(2), 370-381